Spin-Orbit Interaction in Hybrid Josephson Junctions

Master's Thesis
of
Matthew Alexandrakis

August 2013

email: matt.alexandrakis@gmail.com
Graduate student, University of Crete (UOC), Department of Physics

Author:
Matthew Alexandrakis

Supervisor:
Prof. Nikos Flytzanis

Commitee Member A:
Prof. Xenophon Zotos

Commitee Member B:
Prof. Nikolaos Efremidis

Abstract

In this Master's Thesis we study the Rashba spin-orbit coupling effect (RSOC) on the supercurrent and zero-phase current of a short, ballistic Josephson junction, in the clean limit. The junction consists of two s-wave superconductors (S) and three layers in between, a 2-dimensional electron gas ($2DEG$) between two ferromagnets (F) ($S/I_F/F/2DEG/F/I_F/S$). In addition, we have two thin insulator interfaces (I_F) between the superconductors and the ferromagnets, capable of both normal scattering and spin-flip due to inhomogeneous magnetization.

We study this junction by observing how the absolute value of the critical supercurrent, the zero-phase current and the current-phase relation (CPR) change when we introduce a $2DEG$ layer with spin-orbit coupling.

The effects produced by magnetization and spin-orbit coupling are compared. The 2-dimensional electron gas is placed on the xy plane, and that means it produces an electric field, parallel to the z axis, with the induced magnetic field on the plane where the carriers move. As we increase spin-orbit coupling we observe that the magnetization geometry has a strong effect on physical properties. In the half-metallic limit, where due to spin $\downarrow$ cut-off, *singlet correlations* diminish, while *triplet correlations* are induced, which enable long range supercurrent.

Spin-orbit interaction changes the $0 - \pi$ transitions observed due to the magnetization. Also, it breaks the degeneracy for the supercurrent of geometries with equal supercurrent. Oscillations in the critical supercurrent are attributed to exchange fields but also to resonances in the $2DEG$ intermediate layer, which scale in width like λ^{-1}. In the half-metallic limit we see strong *triplet correlations*, which are especially noticed outside the cut-off points in k_p. *Triplet correlations* exist even for smaller exchange fields along with *singlet correlations*. For this, the magnetization geometry is crucial.

Keywords:

- Josephson junction, rashba spin-orbit coupling effect, zero-phase current, current-phase relation (CPR), singlet correlations, triplet correlations, half-metallic limit.

Contents

List of Figures

1 Introduction

We start this Thesis by introducing the reader to the basic theories and phenomena involved in the problem we study. We consider weakly linked superconductors (Josephson junctions) through an intermediate layer (insulator, metal, ferromagnetic layer, etc.) which allow supercurrent to pass through them with zero impedance at zero external voltage. Josephson developed a theory which, involving effectively Cooper pair tunneling, successfully explained the $S/I/S$ junctions with an insulator (I) thickness of about 10 $\mathring{A}$. This is possible, also for large metallic intermediate layers, due to a process called Andreev reflection, which enables pairs of electrons pass through the junction. Multiple Andreev reflections lead to the Andreev bound states, states carrying the supercurrent from one superconductor to the other. We will introduce all of the above in a physical language.

1.1 Superconductivity

H. Kamerlingh Onnes, on April 8, 1911, while studying the resistance of metals at cryogenic temperatures, observed that after a certain temperature, specific for each metal, their resistance abruptly disappeared. This phenomenon was called Superconductivity, meaning that in certain materials, their cooling below a specific critical temperature (T_c) vanishes the electrical resistance expulses magnetic fields. In the following years, many other materials were observed of being superconductive. Starting from a low critical temperature, for pure metals, of around 0.4K to 9K, materials were found to have critical temperatures higher than 100K. The hunt continues for high T_c superconductors, with the highest temperature material being a ceramic material consisting of thallium, mercury, copper, barium, calcium and oxygen ($HgBa_2Ca_2Cu_3O_{8+d}$) with a $T_c = 133K$ [1].

In 1933, Walther Meissner and Robert Ochesfeld discovered the expulsion of a magnetic field from a superconductor, and named the phenomenon the Meissner effect. A superconductor in a magnetic field, produces surface electrical currents. The magnetic field which these surface currents produce, cancels out the applied magnetic field within the bulk of the superconductor. The applied magnetic field penetrates the superconductor within a distance called the London penetration depth, where it is not completely cancelled. The penetration length is characteristic for each superconductor. Due to

the Meissner effect, the superconductors are thought of as having perfect diamagnetism.

Proposed by John Bardeen, Leon Neil Cooper and John Robert Schrieffer, the BCS theory was the first microscopic theory of superconductivity. The theory states that for sufficiently low temperatures, electrons near the Fermi surface form Cooper pairs. This binding occurs in the presence of an attractive potential, which is generally attributed to the interaction between electrons and the vibrating crystal lattice. BCS theory can explain superconductivity quite well in conventional superconductors.

The BCS theory assumes that an attractive force exists between electrons. This force is due to Coulomb attraction between the electron and the crystal lattice. An electron in the lattice will cause a slight increase in positive charges around it. The induced local positive charge will, in turn, attract another electron, making them correlated. These two electrons form what we know as a Cooper pair. However, energy from thermal vibrations of the lattice can break the pair, if it is high enough, else the electrons remain correlated. This explains roughly why superconductivity requires low temperatures. Cooper pairs feel no scattering, thus can propagate without resistance, at zero temperature, and they contribute to the supercurrent. To be more specific, BCS theory describes how two electrons interact, using a weak attraction with an exchange of phonons, in an energy band of ω_D width (where ω_D is Debye frequency) centered on Fermi energy E_F.

1.2 Josephson Effect

The Josephson effect is a macroscopic quantum phenomenon of a current that can flow between two superconductors without being reduced, when no voltage is applied. A weak link is a weak electrical contact put between superconductive electrodes. When the dimensions of such links are sufficiently small, a single-valued and 2π periodic relationship arises between the supercurrent I_s and the phase difference, ϕ, of the condensates on the two superconductive electrodes. The condensate is described by a macroscopic wavefunction (complex order parameter), where the amplitude is related to the density of the superconducting electrons and has a given phase. With increasing dimensions, this relationship deviates gradually from the Josephson behavior. The type of the weak link defines this deviation.

1.2.1 General description

The Josephson effect describes the phenomenon of the current that flows through a weak contact, between two superconductive electrodes, that can

contain a component I_s (supercurrent), which is not dependent on voltage V across the electrodes but on the phase difference

$$\varphi = \chi_2 - \chi_1, \tag{1}$$

where $\chi_{1,2}$ are the phases of the order parameter, Δ, in the electrodes

$$\Delta_{1,2} = |\Delta_{1,2}| \exp(i\chi_{1,2}). \tag{2}$$

In the simplest ("classical") case, the relationship $I_S(\varphi)$ is sinusoidal

$$I_S = I_c \sin\varphi, \tag{3}$$

where I_c is called the supercurrent amplitude or the critical current with no external voltage applied. This phenomenon is called the DC Josephson effect. DC Josephson has been studied by means of probability amplitude of the Andreev reflections by Furusaki, Tsukada [9]. Experimentally, Eq. (3) is a good description for SIS junctions.

The phase φ can also be related to the external voltage V, applied across the superconductive electrodes (superconductors), by the superconducting phase evolution equation

$$\frac{d\varphi}{dt} = \frac{2e}{\hbar} V. \tag{4}$$

where $\frac{h}{2e}$ is the magnetic flux quantum Φ_0. In Eq. (4), φ changes with time, and that produces a supercurrent in the Josephson junction. This phenomenon is called the AC Josephson effect.

Eq. (3), in general junctions, is an approximate one, and various kind of deviations of supercurrent from this dependence may be observed in a superconductive weak link of any type. Moreover, the constant I_c involved in Eq. (3) is essentially dependent on the geometry and material of the weak link, the electrode material, temperature, and other factors.

1.2.2 DC and AC Josephson effects

The phenomena taking place at the Josephson contacts are divided into stationary (DC) and non-stationary (AC) effects, depending on whether the variables, including the phase difference φ, change with time or not.

The phase difference between the two condensates, introduces a non-zero supercurrent flow and if φ remains constant (DC effect), no voltage appears across the junction. As stated above, the supercurrent remains constant in time and it's amplitude can be between $-I_c$ and I_c. When a fixed voltage

V_{DC} is applied across the junction, the phase will vary linearly with time and the current will be an AC current with amplitude I_c and frequency $\frac{1}{h}2eV_{DC}$.

1.3 Andreev process

The mechanism that allows the transfer of supercurrent across a wide intermediate layer is based on the so-called Andreev reflection [4]. It is triggered when a conduction electron in a normal metal hits a superconductor - normal metal (SN) interface. The electron at the Fermi energy μ can not pass through to the superconductor due to absence of single particle states in an energy window of $\mu \pm \Delta$, with Δ being the superconductor energy gap. Inside the gap of the superconductor there are no excitations so that the incident electron can not propagate. Andreev found that the incident electron can correlate with another electron with opposite momentum, form a Cooper pair and pass through to the superconductor. In order to satisfy the boundary conditions we have the reflection of a hole, inside the normal region. Moreover, as the momentum of the hole is nearly identical to that of the incident electron, the hole is retroreflected, following the incident electron's path in the opposite direction. During this process, the superconductor phase is transferred to the hole along with a scattering phase shift. The inverse process is also possible, that is holes can be Andreev reflected into electrons.

1.3.1 Bogoliubov de Gennes equations

Bogoliubov-de Gennes equations [2] describe the quasiparticle excitations in a superconductor, for a two-component wavefunction

$$\vec{\Psi}(\vec{r}) = \begin{pmatrix} \vec{u}(r) \\ \vec{v}(r) \end{pmatrix} \tag{5}$$

where u and v describe the electron and hole part of the quasiparticle excitation. The equation then, reads:

$$\begin{pmatrix} H_0 & \Delta(\vec{r}) \\ \Delta^*(\vec{r}) & -H_0^* \end{pmatrix} \cdot \vec{\Psi}(\vec{r}) = E\vec{\Psi}(\vec{r}) \tag{6}$$

where

$$H_0 = \frac{1}{2m}\left(\frac{\hbar}{i}\vec{\nabla} - \frac{e\vec{A}}{c}\right)^2 + U(\vec{r}) - \mu \tag{7}$$

and $U(\vec{r})$ is the total electrostatic potential, $\Delta(\vec{r})$ the pair potential, and μ the Fermi energy. For $\Delta = 0$ the electron and hole parts in the BdG

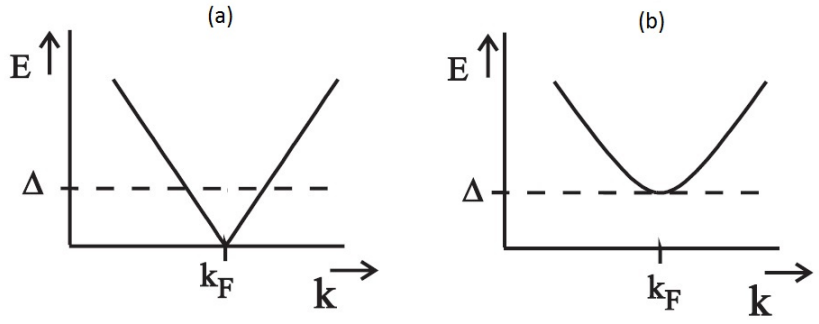

Figure 1.1: (a) Dispersion relation in a normal metal for electrons and holes, left and right of the k_F respectively. (b) Dispersion relation for quasiparticles in a superconductor with an energy gap Δ around Fermi energy E_F. Both have $E = 0$ at the Fermi energy.

equations decouple. $u(\vec{r})$ and $v(\vec{r})$ are the ordinary electron and hole eigenfunctions with energies $\pm E$, relative to the Fermi energy. For a uniform bulk superconductor with $\Delta(\vec{r}) = \Delta_0 e^{i\phi}$, the dispersion relation of the quasiparticles is identical to the well known Bardeen-Cooper-Schrieffer (BCS) theory for superconductivity [3].

$$E = \sqrt{(\frac{\hbar^2 k^2}{2m} - \mu)^2 + \Delta_0^2}. \tag{8}$$

shown in figure 1.1. The quasiparticles have an excitation gap Δ. Below that energy, only evanescent states are available. The dispersion relation for a normal metal, for energies close to the Fermi energy μ is

$$E = |p^2/2m - \mu| \approx \hbar v_F |k - k_F| \tag{9}$$

with the Fermi velocity $v_F = \sqrt{2\mu/m}$ and the Fermi wavevector $k_F = m v_F/\hbar$.

1.3.2 Andreev reflection

When a normal metal is in contact with a superconductor, the Fermi energies of the electrons and Cooper pairs respectively are aligned. Electrons can only pass into the superconductor if their energy is over Δ. When their energy is below Δ, Andreev reflection occurs [4]. An incident electron hits the interface, is annihilated, forming a Cooper pair on the superconductor, while a hole is reflected. The total charge transported across the interface is $q_e - q_h = 2q_{e,Cooper} = 2e$. As the Cooper pair has a total energy of $2E_F$, the incident electron $E_F + E$ and the reflected hole $E_F - E$, the total energy of the process is conserved. This process is shown schematically in figure 1.2.

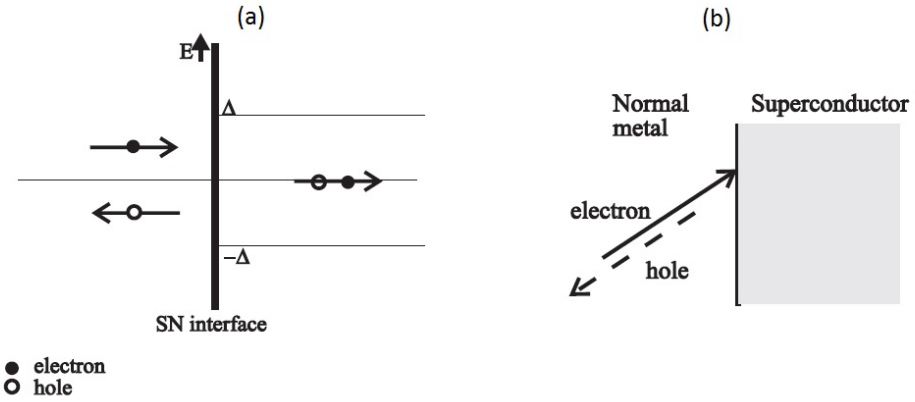

Figure 1.2: (a) The Andreev reflection in energy space, and (b) in real space.

1.3.3 Phase Conjugation

The wavevectors of the incident electron (k^+) and the reflected hole (k^-) are given by

$$k^{\pm} = k_F \pm E/\hbar v_F \tag{10}$$

where k_F is the Fermi wavevector and v_F the Fermi velocity and E is measured from the Fermi energy. As the wavevectors are nearly identical ($E \ll \Delta$), the hole is effectively *retroreflected* and will retrace the incident electron's path backwards.

As the electron traverses the normal region at the Fermi energy, gains a phase θ_e

$$\theta_e = \int_{-L}^{0} k^+ dx \tag{11}$$

while the hole traversing backwards, towards $x = -L$, introduces a phase:

$$\theta_{e,h} = \int_{-L}^{0} k^+ dx + \int_{0}^{-L} k^- dx = 0. \tag{12}$$

This is known as *phase conjugation*. The phase conjugation is complete only when the energy is at the Fermi level ($E = 0$). When $E \neq 0$, the conjugation is not complete, and a small phase $\theta_{e,h}(E) = 2LEv_F/\hbar$ change remains. With phase conjugation we can have bound states that span distances much more than the typical Fermi wavelength of a single particle.

1.3.4 Macroscopic phase imparted on electrons and holes

When an incident electron (or hole) hits an interface in the Andreev reflection process, the macroscopic phase of the superconductor is imparted to the reflected hole (or electron). The phase of the reflected hole is shifted by the phase of the condensate and a phase due to the scattering of electron to hole.

$$\phi_{hole} = \phi_{electron} + \phi_{superconductor} + \arccos(E/\Delta)$$

the corresponding phase shift occurs when the hole is reflected to an electron at the other interface, so that the total phase shift during this process is

$$\Delta\phi_e + \Delta\phi_h + \phi + 2\arccos(E/\Delta)$$

The term $\arccos(E/\Delta)$ is the phase shift acquired by the evanescent quasi-particle wavefunction, which penetrates a total distance of ξ_s, into the superconductive region, where

$$\xi_s = \hbar v_{F,s}/\pi\Delta \tag{13}$$

with $v_{F,s}$ the superconductor's Fermi velocity. When the energy is equal to E_F, Eq. (9) becomes $E = \hbar v_F|k_F - k_F| = 0$. Then, the phase due to penetration of the evanescent quasi-particle wavefunction is equal to $\arccos(E/\Delta) = \arccos(0) = \pi/2$.

1.3.5 Interface scattering

Blonder, Tinkham and Klapwijk (BTK) have shown [5] that the probability of Andreev reflection is strongly reduced by normal interface scattering. In addition, the Fermi velocity mismatch between the normal region and the superconductive region can lead to interface scattering. BTK provided a model to include interface scattering in the form of a delta function with variable height, $V(x) = U_0\delta(x)$. The scattering strength is given by the parameter $Z = U_0/\hbar v_F$.

1.3.6 Double NS interface Andreev reflection

The SNS Josephson junction is essentially two NS interfaces with Fermi velocity mismatches and normal reflection potentials. So,in order to draw conclusions about the junction's function, we can apply what we have already discussed in the previous sections. In the case of an SNS junction, at each NS interface occur Andreev reflections. When we put the two NS interfaces together, Andreev reflections occur in both interfaces and that leads

to multiple Andreev reflections. This phenomenon was first introduced by Klapwijk et al. [19].

An electron (or hole) that hits the left SN interface is Andreev reflected into a hole (or electron) that travels to the right. At the right NS interface it is Andreev reflected into an electron (or hole) that travels to the left. As the flow of the carriers continues, Andreev reflections continue to occur. Andreev reflection enables Cooper pairs from one superconductor to pass through the intermediate region into the other superconductor. Multiple Andreev reflections can enable a flow of Cooper pairs that can lead to supercurrent.

However, we also mentioned that normal scattering strongly reduces the probability for Andreev reflections to occur. That is the reason why normal scattering affects directly the value of the supercurrent. As we introduce a normal scattering potential at the interfaces, an incident electron can be either Andreev reflected or reflected normally.

1.4 Bound states

Inside an SNS with zero external voltage, in general, an infinite number of Andreev reflections occur. The carriers taking part in the process do not gain any energy, and thus can not escape the normal region. These multiple Andreev reflections form current-carrying bound states, inside the SNS junction, as was first discussed by Kulik [20]. We are going to introduce some basic concepts of bound states for $1-D$ systems.

1.4.1 Andreev bound states

We consider an SNS junction, the interfaces of which can induce normal scattering. We include all scattering in the delta function potentials of the interfaces, using the phenomenological parameter Z to characterize the scattering strength, a parameter identical for both interfaces. Z includes the scattering due to mismatch of the Fermi velocities between the superconductor and the normal metal. The scattering potential is

$$V_{barrier} = U_0 \left(\delta(x) + \delta(x-L)\right) \tag{14}$$

where U_0 will be normalized as $Z = \frac{U_0}{E_F/k_F}$. The pair potential, across the junction, has a piece-wise constant form

$$\Delta(x) = \begin{cases} \Delta, & x < 0 \\ 0, & 0 < x < L \\ \Delta e^{i\phi}, & x > L \end{cases} \tag{15}$$

with Δ vanishing in the normal region, but constant in the superconductors ($\Delta \ll \mu$). In Eq. (15), ϕ is the phase of the right superconductor, as in the phase difference, we set $\phi_L = 0$. We solve the boundary conditions at $x = 0$ and $x = L$.

$$\Psi(x)|_{x=0^-} = \Psi(x)_{x=0^+}$$

$$\Psi(x)|_{x=L^-} = \Psi(x)_{x=L^+}$$

$$\frac{\hbar^2}{2m^*}\frac{\partial}{\partial x}\Psi(x)|_{x=0^+} - \frac{\hbar^2}{2m_e}\frac{\partial}{\partial x}\Psi(x)|_{x=0^-} = \frac{\hbar^2 p_F}{2m_e} Z\Psi(x)|_{x=0}$$

$$\frac{\hbar^2}{2m^*}\frac{\partial}{\partial x}\Psi(x)|_{x=L^+} - \frac{\hbar^2}{2m_e}\frac{\partial}{\partial x}\Psi(x)|_{x=L^-} = \frac{\hbar^2 p_F}{2m_e} Z\Psi(x)|_{x=L}$$

We solve the BdG equations, assuming a constant effective mass m_*. The wavevectors for electrons (k^+) and holes (k^-) in the normal region, are given

$$\hbar q^{\pm} = \sqrt{2m(\mu \pm E)} \tag{16}$$

and for the superconductor

$$\hbar k^{\pm} = \sqrt{2m(\mu \pm \sqrt{E^2 - \Delta^2})} \tag{17}$$

The wavefunction is

$$\Psi(x) = \begin{cases} ae^{ikx}\begin{pmatrix} v \\ u \end{pmatrix} + be^{ikx}\begin{pmatrix} u \\ v \end{pmatrix} & x < 0 \\ (\alpha e^{iq^+x} + \beta e^{-iq^+(x-L)})\begin{pmatrix} 1 \\ 0 \end{pmatrix} & \\ +(\gamma e^{iq^-(x-L)} + \delta e^{-iq^-x})\begin{pmatrix} 0 \\ 1 \end{pmatrix} & 0 < x < L \\ ce^{ik(x-L)}\begin{pmatrix} ue^{i\phi/2} \\ ve^{-i\phi/2} \end{pmatrix} + de^{-ik(x-L)}\begin{pmatrix} ve^{i\phi/2} \\ ue^{-i\phi/2} \end{pmatrix} & x > L \end{cases}$$

Eliminating $\alpha,\ \beta,\ \gamma,\ \delta$, the conditions form a set of equations, shown in a matrix form:

$$\begin{bmatrix} A^+v & \bar{A}^+u & B^+e^{i\phi/2}u & B^+e^{i\phi/2}v \\ A^-u & \bar{A}^-v & B^-e^{-i\phi/2}u & B^-e^{-i\phi/2}v \\ B^+u & B^+v & \bar{A}^+e^{i\phi/2}u & A^+e^{i\phi/2}v \\ B^-u & B^-v & \bar{A}^-e^{-i\phi/2}u & A^-e^{-i\phi/2}v \end{bmatrix} \cdot \begin{bmatrix} a \\ b \\ c \\ d \end{bmatrix} = \begin{bmatrix} 0 \\ 0 \\ 0 \\ 0 \end{bmatrix} \tag{18}$$

where $A^{\pm} = -q^{\pm}/(m^* tan(q^{\pm}L)) - k_F Z - ik,\ B^{\pm} = q^{\pm}/(m^* sin(q^{\pm}L))$, and $\bar{A}^{\pm}$ is the complex conjugate of $A^{\pm}$, in dimensionless quantities.

1.4.2 Supercurrent in short junctions

Limiting the junction to short lengths, the phase difference imparted on the carriers for traversing the normal region is negligible, so that $(k^+ - k^-)L \ll 1$. Using Taylor series on $\sqrt{1 \pm x} \approx 1 \pm x/2$, so from Eq. (16) we can derive that $k^{\pm} \approx k_F E/2\mu$, and $v_F = \hbar k_F/m^*$. The condition, then, becomes $\frac{2E}{\hbar v_F} L \ll 1$. We only consider states that have energies within the superconductor energy gap, so that the maximum E will assume the value Δ. The condition becomes

$$L \ll \xi_0 \tag{19}$$

with

$$\xi_0 = \frac{\hbar v_F}{2\Delta}. \tag{20}$$

When the above condition is satisfied, we can take the limit of $L \to 0$ to simplify the matrix of the Eq. (18). If we set the determinant of the matrix equal to zero, we can solve the set of equations, for energy E,

$$E = \pm\Delta\sqrt{\frac{cos^2(\phi/2) + Z^2}{1 + Z^2}} \tag{21}$$

For $Z = 0$, Eq. (21) becomes $E = \pm\Delta cos(\frac{\phi}{2})$, a result produced by Kulik [20]. In figure 1.3, the bound states are plotted for three values of Z, both for positive and negative values of energy. Note that the bound states branches are symmetrical, that is for each energy there is a corresponding negative energy. An interface with $(Z \neq 0)$ leads to a gap in the bound states, which as shown, increases fast with Z. When temperature is $T = 0$, the bound states below the Fermi energy level can carry a supercurrent that depends on the superconductor phase difference:

$$I = -\frac{2e}{\hbar}\frac{dE}{d\phi} \tag{22}$$

Combining the above equation with bound state spectrum, $E = \pm\Delta cos(\frac{\phi}{2})$, we derive the current-phase relation (CPR) in figure 1.4. For short junctions, the continuous bound state spectrum, for energies above the superconductor gap, do not contribute to the supercurrent [21]. The non-sinusoidal $I(\phi)$ relation transitions to sinusoidal when normal interface scattering is introduced. As we observe at figure 1.4, when $Z = 0.5$, the $I(\phi)$ relation has already transitioned to a sinusoidal form.

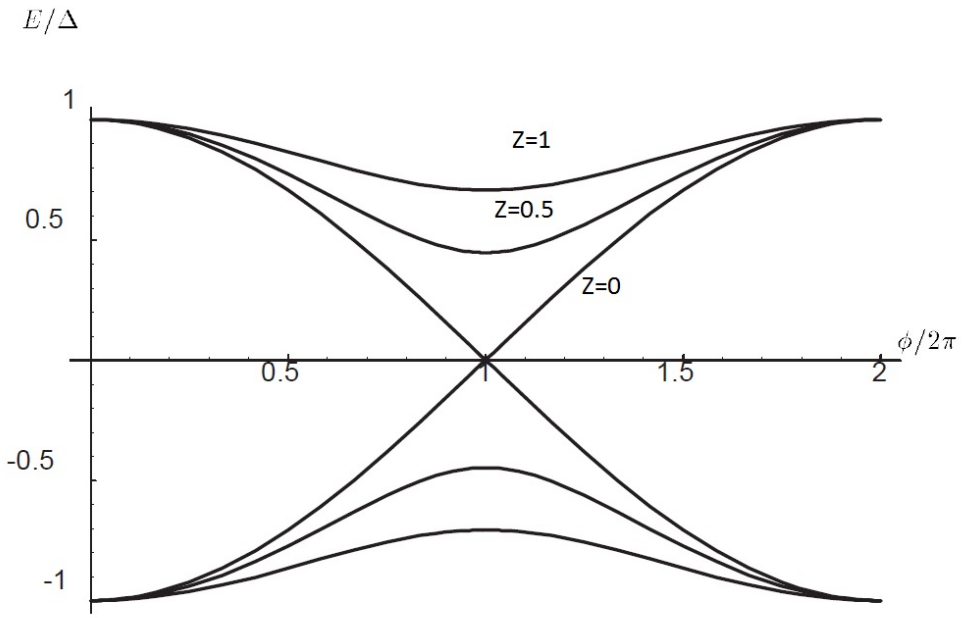

Figure 1.3: Bound state energy versus superconductor phase difference, for $Z = 0$, $Z = 0.5$ and $Z = 1$.

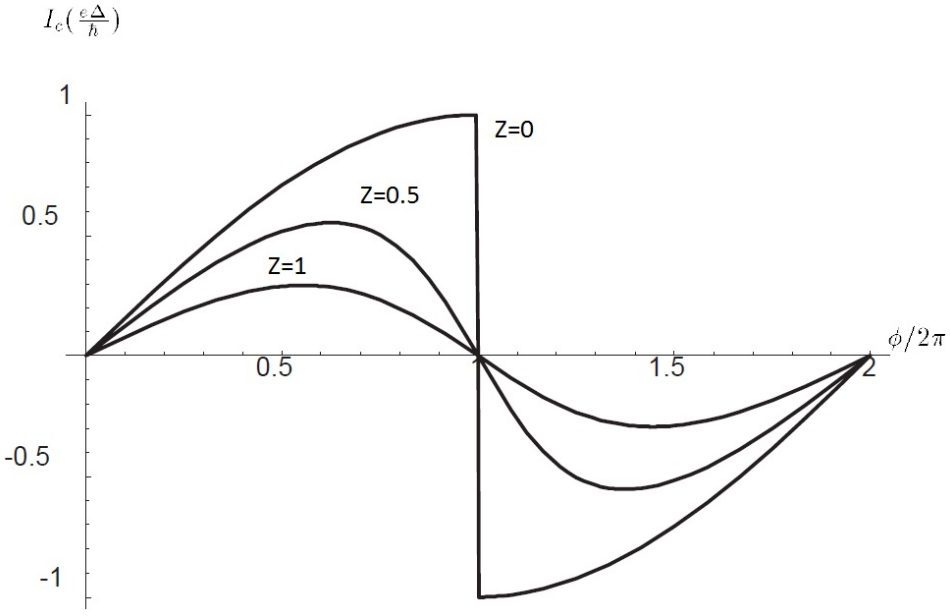

Figure 1.4: Current-phase relation for three values of normal interface scattering, $T/T_c = 0$, $Z = 0$, $Z = 0.5$ and $Z = 1$.

1.5 Organization of Thesis

In section 2, we approach the $S/F/2DEG/F/S$ junction analytically. We solve the BdG equations [2] by using the Klapwijk, Blonder and Tinkham model (BTK) [19]. We then proceed to calculate the supercurrent with the Furusaki-Tsukada method [8] by summing analytically the contributions from the normal Andreev reflection, in a single term [28].

In section 3, we produce numerical results for simple junctions, both as a point of comparison and as a code validation method. We study the critical supercurrent, current as a function of k_p, and current-phase relation for SNS, $S/2DEG/S$ and SFS junctions.

In section 4, we study the $S/F/2DEG/F/S$ junction numerically. We observe how parameters of the junction and more specifically the spin-orbit interaction affects weak and strong magnetization induced phenomena.

In section 5, we summarize the results and discuss potential problems and further expansion of this Thesis subject.

2 Analytical approach - The $SF/2DEG/FS$ junction

We consider a clean two-dimensional ballistic $SF/2DEG/FS$ Josephson junction. The left and right superconductors are assumed identical except for the different macroscopic phases. The interface barriers at $x = 0$ and $x = d_L + d + d_R = L$ are in the zy plane and are capable of both normal scattering and spin-flips due to interface magnetization (gray areas). The quantum spin-axis is set along the z-axis. A schematic approach of the $SF/2DEG/FS$ junction is in figure 2.1.

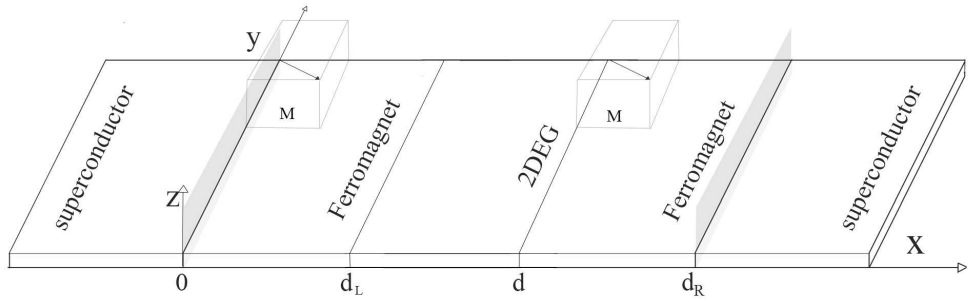

Figure 2.1: Schematic of an $SF/2DEG/FS$ junction. Gray areas denote spin-active interfaces with normal scattering potential.

2.1 BdG Hamiltonian of the junction

The BdG equation describing the junction is given by

$$\begin{pmatrix} H(k) & \Delta(k) \\ -\Delta^*(-k) & -H^*(-k)) \end{pmatrix} \begin{pmatrix} \hat{u} \\ \hat{v} \end{pmatrix} = E \begin{pmatrix} \hat{u} \\ \hat{v} \end{pmatrix} \tag{23}$$

where

$$H(k) = H_0(k) + H_{RSOC}(k) - H_M \tag{24}$$

is the Hamiltonian of the problem, and the components of this Hamiltonian are:

$$H_0(k) = \varepsilon_k - \mu + V(x) \tag{25}$$

$\varepsilon_k = \frac{\hbar^2 k^2}{2m}$ being the kinetic energy and μ is the chemical potential, of the system. The interface potential is $V(x) = U_0 \left[\delta(x) + \delta(x - L)\right]$ and the scattering strength is given by the parameter $Z = U_0/\hbar v_F$.

$$H_{RSOC}(k) = \frac{\lambda_0}{\hbar}\left(\sigma_y p_x - \sigma_x p_y\right)\theta_0(x) \tag{26}$$

$H_{RSOC}(k)$ describes the Rashba spin-orbit coupling (RSOC) in the $2DEG$ region [23] with λ_0 the RSOC constant. σ_x and σ_y are the Pauli spin matrices, p_x and p_y are the two components of the momentum operator p, $\theta_0(x) = \theta(x - d_L)\theta(x - L - d_R)$ with $\theta(x)$ the Heavyside step function.

$$H_M(x) = \sigma \cdot M(x) \tag{27}$$

where $\sigma = (\sigma_x, \sigma_y, \sigma_z)$ of the Pauli matrices. $M(x)$ is the self-consistent pair magnetization vector of the junction, measured in energy units. It is written in the form

$$M(x) = \sum_i M_i(x)\chi_i(x) + \sum_j N_j \delta(x - x_j) \tag{28}$$

2.2 Stationary scattering states

The equilibrium supercurrent can be calculated by the method of Furusaki-Tsukada [8]. This calculation is dependent on the asymptotic form of the stationary scattering states of the BdG Hamiltonian and specifically the Andreev scattering amplitudes [4]. Andreev scattering amplitudes are the reflection amplitudes, with particle and spin reversal, when compared to the incident state. We assume that the pair potential and the magnetization are determined self-consistently, meaning that both assume their bulk values exponentially, as the distance from the interface grows. This enables us to study the problem with the short range potential scattering theory. Specifically, we define the existence of two spatial points on the left and right side of the junction, beyond which the pair potential assumes its bulk constant value. The BdG equations are then solved separately in each region (left SC, left FM, $2DEG$, right FM, right SC) and the solutions are matched at the respective boundaries. The junction is placed on the xy plane. The left superconductor (LSC) extends for $x \leq 0$, the left ferromagnet (LFM) from $0 \leq x \leq d_L$, the 2-dimensional electron gas (2DEG) from $d_L \leq x \leq d$, the right ferromagnet (RFM) from $d \leq x \leq d_R$, and the right superconductor (RSC) for $x \geq d_R$. We have translational invariance along the y axis, so that the momentum, parallel to the interface (k_p), is conserved, so that the y-dependent wavefunction is $e^{ik_p y}$. k_p is normalized on Fermi wavevector k_F and takes values from -1 to 1.

2.2.1 Superconductor eigenfunctions

The linearly independent solutions of the superconductors [28] are given below. We define $\nu = L, R$ for left and right superconductor respectively. For the left, we have the wavefunctions of the scattered states travelling to $-\infty$. That means that the planar wave for electrons is $e^{-ik_{eL}x}$ and for holes is $e^{+ik_{hL}x}$. For the right, the transmitted wavefunctions for electrons are $e^{+ik_{eR}x}$, and holes are $e^{-ik_{hR}x}$. Thus, in each superconductor, the wavefunction is a linear combination of the following

$$\Psi_{e\uparrow\nu}(x) = \begin{pmatrix} u_\nu(E)e^{i\frac{\chi_\nu}{2}} \\ 0 \\ 0 \\ v_\nu(E)e^{-i\frac{\chi_\nu}{2}} \end{pmatrix} e^{\pm ik_{e\nu}x}e^{ik_p y}, \tag{29}$$

$$\Psi_{e\downarrow\nu}(x) = \begin{pmatrix} 0 \\ u_\nu(E)e^{i\frac{\chi_\nu}{2}} \\ -v_\nu(E)e^{-i\frac{\chi_\nu}{2}} \\ 0 \end{pmatrix} e^{\pm ik_{e\nu}x}e^{ik_p y}, \tag{30}$$

$$\Psi_{h\uparrow\nu}(x) = \begin{pmatrix} 0 \\ v_\nu(E)e^{i\frac{\chi_\nu}{2}} \\ -u_\nu(E)e^{-i\frac{\chi_\nu}{2}} \\ 0 \end{pmatrix} e^{\pm ik_{h\nu}x}e^{ik_p y}, \tag{31}$$

$$\Psi_{h\downarrow\nu}(x) = \begin{pmatrix} v_\nu(E)e^{i\frac{\chi_\nu}{2}} \\ 0 \\ 0 \\ u_\nu(E)e^{-i\frac{\chi_\nu}{2}} \end{pmatrix} e^{\pm ik_{h\nu}x}e^{ik_p y}, \tag{32}$$

where

$$k_{e\nu,h\nu} = \sqrt{\frac{2m}{\hbar^2}\left(\mu - U \pm \mathrm{sgn}(E)\sqrt{E^2 - |\Delta|^2}\right) - k_p^2} \tag{33}$$

are the wavenumbers for electrons and holes on the left superconductor (and right) respectively, χ_ν is the phase of the superconducting order parameter for left and right superconductors. Also,

$$u_\nu(E) = \sqrt{\frac{1}{2}\left(1 + \frac{\Omega_\nu}{E}\right)} \tag{34}$$

and

$$v_\nu(E) = \mathrm{sgn}(E)\sqrt{\frac{1}{2}\left(1 - \frac{\Omega_\nu}{E}\right)}, \tag{35}$$

are the coherence factors for both superconductors.

2.2.2 Ferromagnet eigenfunctions

In this section we use Stoner's model to define eigenfunctions in a ferromagnet with a magnetization $\mathbf{M}$ [28]. By setting $\Delta = 0$ in BdG equations, we get

$$\begin{pmatrix} h_0 - \mu - \boldsymbol{\sigma}\cdot\mathbf{M} & \hat{0} \\ \hat{0} & -h_0 + \mu + (\boldsymbol{\sigma}\cdot\mathbf{M})^* \end{pmatrix} \begin{pmatrix} \hat{u}(x) \\ \hat{v}(x) \end{pmatrix} = E \begin{pmatrix} \hat{u}(x) \\ \hat{v}(x) \end{pmatrix}. \quad (36)$$

The solutions for electrons and holes can be decoupled into two independent equations

$$(h_0 - \mu - \boldsymbol{\sigma}\cdot\mathbf{M})\hat{u}(x) = E\hat{u}(x) \quad (37)$$

$$(h_0 - \mu - (\boldsymbol{\sigma}\cdot\mathbf{M})^*)\hat{v}(x) = -E\hat{v}(x). \quad (38)$$

The magnetization vector is given in polar coordinates, with a magnitude of M, and ϕ, θ the radial and angular coordinates respectively, so that

$$\boldsymbol{\sigma}\cdot\mathbf{M} = M \begin{pmatrix} \cos\theta & e^{-i\phi}\sin\theta \\ e^{i\phi}\sin\theta & -\cos\theta \end{pmatrix}. \quad (39)$$

We can derive the energy eigenvalues of a homogeneous ferromagnet for electron-like excitations

$$\Psi_{e\uparrow}(x) = \begin{pmatrix} \cos\frac{\theta}{2}e^{-i\frac{\phi}{2}} \\ \sin\frac{\theta}{2}e^{i\frac{\phi}{2}} \\ 0 \\ 0 \end{pmatrix} e^{\pm iq_{e\uparrow}x}e^{ik_p y} \quad (40)$$

$$\Psi_{e\downarrow}(x) = \begin{pmatrix} -\sin\frac{\theta}{2}e^{-i\frac{\phi}{2}} \\ \cos\frac{\theta}{2}e^{i\frac{\phi}{2}} \\ 0 \\ 0 \end{pmatrix} e^{\pm iq_{e\downarrow}x}e^{ik_p y}, \quad (41)$$

where

$$q_{es} = \sqrt{\frac{2m}{\hbar^2}(\mu - U + sM + E) - k_p^2}. \quad (42)$$

with s indicating $\uparrow, \downarrow$ spin states. In each ferromagnet, with magnetization angles $\theta,\ \phi$, the hole-like excitations in the ferromagnet are

$$\Psi_{h\uparrow}(x) = \begin{pmatrix} 0 \\ 0 \\ \cos\frac{\theta}{2}e^{i\frac{\phi}{2}} \\ \sin\frac{\theta}{2}e^{-i\frac{\phi}{2}} \end{pmatrix} e^{\pm iq_{h\uparrow}x}e^{ik_py} \tag{43}$$

$$\Psi_{h\downarrow}(x) = \begin{pmatrix} 0 \\ 0 \\ -\sin\frac{\theta}{2}e^{i\frac{\phi}{2}} \\ \cos\frac{\theta}{2}e^{-i\frac{\phi}{2}} \end{pmatrix} e^{\pm iq_{h\downarrow}x}e^{ik_py}, \tag{44}$$

where

$$q_{hs} = \sqrt{\frac{2m}{\hbar^2}(\mu - U + sM - E) - k_p^2}. \tag{45}$$

is the wavenumber for hole-like excitations with $s = \uparrow, \downarrow$ spin states. The above are the wavefunctions for a single ferromagnet. In our study, we have two ferromagnets. The left ferromagnet is placed from $0 \leq x \leq d_L$ and the right ferromagnet is placed from $d \leq x \leq d_R$. The same expressions hold if we put the corresponding direction angles for each magnetization.

2.2.3 Two-dimensional electron gas eigenfunctions

Rashba Hamiltonian and electron transport have been studied by Molenkamp et. al. [10, 11]. In addition, triplet Josephson current modulated by Rashba spin-orbit coupling has been studied by Yang et. al. [12]. In Eq. (26) we defined the Rashba hamiltonian for spin-orbit interaction

$$H_{RSOC}(k) = \frac{\lambda_0}{\hbar}\left(\sigma_y p_x - \sigma_x p_y\right)\theta_0(x).$$

where the function θ_0 is 1 inside the $2DEG$ and 0 outside. The above equation is derived from

$$H_{RSOC}(k) = \lambda_0(-i\vec{\nabla} \times \vec{E}) \cdot \vec{\sigma} = \frac{\lambda_0}{\hbar}\vec{E}_z \cdot (\vec{\sigma} \cdot \vec{k})_z \tag{46}$$

where $\vec{E}_z$ is the electric field (in z-direction) vector in the $2DEG$ which is placed on the xy plane. The wavefunction for the $2DEG$ is

$$\Psi_{RSOC} = e^{ik_p y}\left[\frac{c_{e1R}}{\sqrt{2}}\begin{pmatrix} e^{i\chi(a_1)} \\ 1 \\ 0 \\ 0 \end{pmatrix} e^{iq_{e1}x} + \frac{c_{e1L}}{\sqrt{2}}\begin{pmatrix} e^{i\chi(a_1 r)} \\ 1 \\ 0 \\ 0 \end{pmatrix} e^{-iq_{e1}x}\right.$$
$$+\frac{c_{e2R}}{\sqrt{2}}\begin{pmatrix} -e^{i\chi(a_2)} \\ 1 \\ 0 \\ 0 \end{pmatrix} e^{iq_{e2}x} + \frac{c_{e2L}}{\sqrt{2}}\begin{pmatrix} -e^{i\chi(a_2 r)} \\ 1 \\ 0 \\ 0 \end{pmatrix} e^{-iq_{e2}x}$$
$$+\frac{c_{h1R}}{\sqrt{2}}\begin{pmatrix} 0 \\ 0 \\ -e^{-i\chi(b_1 r)} \\ 1 \end{pmatrix} e^{-iq_{h1}x} + \frac{c_{h1L}}{\sqrt{2}}\begin{pmatrix} 0 \\ 0 \\ -e^{-i\chi(b_1)} \\ 1 \end{pmatrix} e^{iq_{h1}x}$$
$$\left.+\frac{c_{h2R}}{\sqrt{2}}\begin{pmatrix} 0 \\ 0 \\ e^{-i\chi(b_2 r)} \\ 1 \end{pmatrix} e^{-iq_{h2}x} + \frac{c_{h2L}}{\sqrt{2}}\begin{pmatrix} 0 \\ 0 \\ e^{-i\chi(b_2)} \\ 1 \end{pmatrix} e^{iq_{h2}x}\right] \tag{47}$$

where k_p is the conserved momentum parallel to the interface. The propagation coefficients, $c_{ps\nu}$, are the coefficients for the respective particles and spin modes, with $p = e,\ h$ the particle counter, $s = 1,\ 2$ the spin mode of a carrier, and $\nu = L,\ R$ the direction that a particle is propagating compared to the x axis, with L being the propagation to the left, and R to the right. The spin-dependent wavevectors of particles are $q_{e1},\ q_{e2},\ q_{h1},\ q_{h2}$. $\chi(a_i) = \pi/2 - a_i,\ \chi(a_i r) = a_i - \pi/2$ and $a_{i=1,2}$ are the angles between electron wavevectors and the x axis, while $\chi(b_i) = \pi/2 - b_i,\ \chi(b_i r) = b_i - \pi/2$ and $b_{i=1,2}$ are the angles between hole wavevectors and the x axis. In order to define the wavevectors inside the 2DEG we first define the Fermi wavevector

$$k_F = \sqrt{2mE_F/\hbar^2}, \tag{48}$$

where E_F is the Fermi energy level and m the mass of the particles. Also the Rashba wavevector

$$k_R = m\lambda_0/\hbar^2, \tag{49}$$

where λ_0 is the unnormalized spin-orbit interaction constant. The amplitudes of the wavevectors of particles $p = e,\ h$ and spin modes $s = 1,\ 2$ are given by

$$q_{e10} = \sqrt{k_R^2 + k_F^2 + 2mE/\hbar^2} - k_R \tag{50}$$

$$q_{e20} = \sqrt{k_R^2 + k_F^2 + 2mE/\hbar^2} + k_R \tag{51}$$

$$q_{h10} = \sqrt{k_R^2 + k_F^2 - 2mE/\hbar^2} - k_R \tag{52}$$

$$q_{h20} = \sqrt{k_R^2 + k_F^2 - 2mE/\hbar^2} + k_R \tag{53}$$

The normal component of the wavevectors are

$$q_{e1} = \sqrt{q_{e10}^2 - k_p^2} \tag{54}$$

$$q_{e2} = \sqrt{q_{e20}^2 - k_p^2} \tag{55}$$

$$q_{h1} = \sqrt{q_{h10}^2 - k_p^2} \tag{56}$$

$$q_{h2} = \sqrt{q_{h20}^2 - k_p^2} \tag{57}$$

since we assume homogeneity along y axis, and k_p is conserved. The angles of the wavevectors, Eqs. (50) to (53), are given by

$$\begin{aligned} a1 &= arctan(k_p/qe1) \\ a2 &= arctan(k_p/qe2) \\ b1 &= arctan(k_p/qh1) \\ b2 &= arctan(k_p/qh2) \end{aligned} \tag{58}$$

2.2.4 Normalization of parameters

In order to calculate the supercurrent using the Andreev scattering amplitudes, we normalize our parameters.

As we have already mentioned, the widths are normalized on the Fermi wavevector k_F^{-1} of the left superconductor. The pair potential, Δ, is normalized over the Fermi energy, E_F, of the left superconductor, as well as the ferromagnet magnetization strength, M, the interface magnetization, Z_m, and the interface normal scattering strength, Z_n. In this study, the Fermi energy (taken from the bottom of the conduction band) is considered the same for all layers. The particle mass, m, is considered constant across the junction, and in case of different masses, it is normalized over the particle mass of the left superconductor, m_0. All wavevectors are normalized over the Fermi wavevector, k_F, of the left superconductor. The spin-orbit coupling constant λ is normalized over the Fermi energy divided by the Fermi wavevector, E_F/k_F. It is convenient to introduce the Rashba wavevector, $k_R = m\lambda_0/\hbar^2$, which we normalized over k_F, so that $k_R/k_F = \frac{m\lambda_0}{\hbar^2 k_F} = \frac{m}{m_0}\frac{\lambda_0}{\hbar^2 k_F^2/m_0}k_F = \bar{m}\frac{\lambda}{2E_F}k_F = \bar{m}\lambda$. When m is constant across the junction, $\bar{m} = 1$, thus $\lambda = \lambda_0 k_F/2E_F$. The current is normalized over $e\Delta_{L0}/\hbar$.

2.3 Boundary conditions

Having written the wavefunctions for each layer in the junction, we need to solve for 32 coefficients. There are 4 scattering amplitudes for the left superconductor, 4 propagation amplitudes for the right superconductor, and 8 coefficients for each intermediate layer in between. We solve the boundary conditions for each interface. The boundary conditions for the left superconductor ($x = 0^-$) and the left ferromagnet ($x = 0^+$) are

$$\begin{aligned} \Psi(x)|_{x=0^+} &= \Psi(x)|_{x=0^-} \\ v_x\Psi(x)|_{x=0^+} - v_x\Psi(x)|_{x=0^-} &= Z_0\tau\Psi(0) \end{aligned} \tag{59}$$

for the left ferromagnet ($x = d_L^-$) and the 2DEG ($x = d_L^+$) are

$$\begin{aligned} \Psi(x)|_{x=d_L^+} &= \Psi(x)|_{x=d_L^-} \\ v_x\Psi(x)|_{x=d_L^+} - v_x\Psi(x)|_{x=d_L^-} &= \tau\Psi(d_L) \end{aligned} \tag{60}$$

for the 2DEG ($x = d^-$) and the right ferromagnet ($x = d^+$) are

$$\begin{aligned} \Psi(x)|_{x=d^+} &= \Psi(x)|_{x=d^-} \\ v_x\Psi(x)|_{x=d^+} - v_x\Psi(x)|_{x=d^-} &= \tau\Psi(d) \end{aligned} \tag{61}$$

for the right ferromagnet ($x = d_R^-$) and the right superconductor, for $x = d_R^+$

$$\begin{aligned} \Psi(x)|_{x=d_R^+} &= \Psi(x)|_{x=d_R^-} \\ v_x\Psi(x)|_{x=d_R^+} - v_x\Psi(x)|_{x=d_R^-} &= Z_0\tau\Psi(d_R) \end{aligned} \tag{62}$$

where v_x the velocity operator

$$v_x = \begin{pmatrix} -\frac{\hbar}{m}\frac{\partial}{\partial x} & \frac{\lambda_0}{\hbar}\theta_0(x) & 0 & 0 \\ -\frac{\lambda_0}{\hbar}\theta_0(x) & -\frac{\hbar}{m}\frac{\partial}{\partial x} & 0 & 0 \\ 0 & 0 & \frac{\hbar}{m}\frac{\partial}{\partial x} & -\frac{\lambda_0}{\hbar}\theta_0(x) \\ 0 & 0 & \frac{\lambda_0}{\hbar}\theta_0(x) & \frac{\hbar}{m}\frac{\partial}{\partial x} \end{pmatrix} \tag{63}$$

and τ is

$$\tau = \begin{pmatrix} 1 & 0 & 0 & 0 \\ 0 & 1 & 0 & 0 \\ 0 & 0 & -1 & 0 \\ 0 & 0 & 0 & -1 \end{pmatrix} \tag{64}$$

where θ_0 is the domain function for the $2DEG$, and Z_0 is the matrix

$$Z_0 = \begin{pmatrix} \hat{Z}_j & \hat{0} \\ \hat{0} & \hat{Z}_j{}^* \end{pmatrix} \tag{65}$$

with

$$\hat{Z}_j = \frac{2m_0}{\hbar^2} V_j \hat{1} - \frac{2m_0}{\hbar^2} \boldsymbol{\sigma} \cdot \mathbf{N}_j. \tag{66}$$

which include both normal and spin-flip scattering

2.4 The matching matrix from the boundary conditions

From section 3.4, we have a linear system of 32 coefficients. We define that ℓ, r denote the left and right ferromagnet, whereas L, R the left and right superconductor.

$$\begin{pmatrix} L_1 & F_{11}^{\ell} & F_{12}^{\ell} & 0 & 0 & 0 & 0 & 0 \\ L_2 & F_{21}^{\ell} & F_{22}^{\ell} & 0 & 0 & 0 & 0 & 0 \\ 0 & f_{11}^{\ell} & f_{12}^{\ell} & S_{11} & S_{12} & 0 & 0 & 0 \\ 0 & f_{21}^{\ell} & f_{22}^{\ell} & S_{21} & S_{22} & 0 & 0 & 0 \\ 0 & 0 & 0 & s_{11} & s_{12} & F_{11}^{r} & F_{12}^{r} & 0 \\ 0 & 0 & 0 & s_{21} & s_{22} & F_{21}^{r} & F_{22}^{r} & 0 \\ 0 & 0 & 0 & 0 & 0 & f_{11}^{r} & f_{12}^{r} & R_1 \\ 0 & 0 & 0 & 0 & 0 & f_{21}^{r} & f_{22}^{r} & R_2 \end{pmatrix} \begin{pmatrix} \alpha \\ \beta^{\ell} \\ \eta \\ \beta^{r} \\ \gamma \end{pmatrix} = B_{ps} \tag{67}$$

where L_1 and L_2 are 4×4 matrices

$$L_1 = \begin{pmatrix} u_L \hat{1} & v_L \hat{1} \\ -ik_{eL} u_L \hat{1} & ik_{hL} v_L \hat{1} \end{pmatrix} e^{\frac{i\chi_L}{2}} \tag{68}$$

$$L_2 = \begin{pmatrix} v_L \hat{1}_a & u_L \hat{1}_a \\ -ik_{eL} v_L \hat{1}_a & ik_{hL} u_L \hat{1}_a \end{pmatrix} e^{-\frac{i\chi_L}{2}}, \tag{69}$$

R_1 and R_2 are 4×4 matrices

$$R_1 = -\begin{pmatrix} u_R \hat{1} & v_R \hat{1} \\ \frac{ik_{eR}}{\widetilde{m}_R} u_R \hat{1} & -\frac{ik_{hR}}{\widetilde{m}_R} v_R \hat{1} \end{pmatrix} e^{\frac{i\chi_R}{2}} \tag{70}$$

$$R_2 = -\begin{pmatrix} v_R \hat{1}_a & u_R \hat{1}_a \\ \frac{ik_{eR}}{\widetilde{m}_R} v_R \hat{1}_a & -\frac{ik_{hR}}{\widetilde{m}_R} u_R \hat{1}_a \end{pmatrix} e^{-\frac{i\chi_R}{2}}, \tag{71}$$

where $\hat{1}$ is the unitary matrix and $\hat{1}_a$ is

$$\hat{1}_a = \begin{pmatrix} 0 & -1 \\ 1 & 0 \end{pmatrix}.$$

We also consider the mass to be constant across the junction, so the normalized right superconductor mass is $\widetilde{m}_R = 1$. F^{ℓ}_{ij}, f^{ℓ}_{ij}, S_{ij}, s_{ij}, F^{r}_{ij}, f^{r}_{ij} are all 4×4 matrices, and the indices $i,j = 1,2$ correspond to their position on the matrix of Eq. (67). Elements denoted with 0, are 4×4 matrices comprised only of zeroes. When $i \neq j$ the above matrices are zero.

The $F^{\ell,r}_{ij}$ for $i = j$ are

$$F_{11} = \left(\; E_+ \; \middle| \; E_- \; \right) \tag{72}$$

$$F_{22} = \left(\; H_+ \; \middle| \; H_- \; \right), \tag{73}$$

where

$$E_+ = \begin{pmatrix} -e_\uparrow & -e_\downarrow \\ (-\frac{iq_{e\uparrow}}{\widetilde{m}_{\ell,r}} + \hat{Z}_\ell)e_\uparrow & (-\frac{iq_{e\downarrow}}{\widetilde{m}_{\ell,r}} + \hat{Z}_\ell)e_\downarrow \end{pmatrix} \tag{74}$$

$$H_+ = \begin{pmatrix} -h_\uparrow & -h_\downarrow \\ (-\frac{iq_{h\uparrow}}{\widetilde{m}_{\ell,r}} + \hat{Z}^*_\ell)h_\uparrow & (-\frac{iq_{h\downarrow}}{\widetilde{m}_{\ell,r}} + \hat{Z}^*_\ell)h_\downarrow \end{pmatrix}, \tag{75}$$

from which we obtain E_- and H_- if we change $q_{e\uparrow,\downarrow} \to -q_{e\uparrow,\downarrow}$ in E_+, and $q_{h\uparrow,\downarrow} \to -q_{h\uparrow,\downarrow}$ in H_+, respectively.

In addition, $f^{\ell,r}_{ij}$ matrices for $i = j$ are

$$f_{11} = \left(\; E'_+ \; \middle| \; E'_- \; \right) \tag{76}$$

$$f_{22} = \left(\; H'_+ \; \middle| \; H'_- \; \right), \tag{77}$$

where E'_+ and H'_+ are

$$E'_+ = \begin{pmatrix} e_\uparrow e^{iq_{e\uparrow}d_{L,R}} & e_\downarrow e^{iq_{e\downarrow}d_{L,R}} \\ (\frac{iq_{e\uparrow}}{\widetilde{m}_{\ell,r}} + \hat{Z}_r)e_\uparrow e^{iq_{e\uparrow}d_{L,R}} & (\frac{iq_{e\downarrow}}{\widetilde{m}_{\ell,r}} + \hat{Z}_r)e_\downarrow e^{iq_{e\downarrow}d_{L,R}} \end{pmatrix} \tag{78}$$

$$H'_+ = \begin{pmatrix} h_\uparrow e^{iq_{h\uparrow}d_{L,R}} & h_\downarrow e^{iq_{h\downarrow}d_{L,R}} \\ (\frac{iq_{h\uparrow}}{\widetilde{m}_{\ell,r}} + \hat{Z}^*_r)h_\uparrow e^{iq_{h\uparrow}d_{L,R}} & (\frac{iq_{h\downarrow}}{\widetilde{m}_{\ell,r}} + \hat{Z}^*_r)h_\downarrow e^{iq_{h\downarrow}d_{L,R}} \end{pmatrix}. \tag{79}$$

and E'_- and H'_- are obtained by changing $q_{e\uparrow,\downarrow} \to -q_{e\uparrow,\downarrow}$ in E'_+, and $q_{h\uparrow,\downarrow} \to -q_{h\uparrow,\downarrow}$ in H'_+, respectively.

The $e_{\uparrow,\downarrow}$ spinors are defined

$$e_\uparrow = \begin{pmatrix} e^{-i\phi/2}\cos\theta/2 \\ e^{i\phi/2}\sin\theta/2 \end{pmatrix}, \quad e_\downarrow = \begin{pmatrix} -e^{-i\phi/2}\sin\theta/2 \\ e^{i\phi/2}\cos\theta/2 \end{pmatrix} \tag{80}$$

The $h_{\uparrow,\downarrow}$ spinors are defined as the conjugate of the respective electron spinors, $h_s = e_s^*$. These four spinors are different for the left and right ferromagnet, as the angles can be changed independently for each ferromagnetic layer, so that $\phi \to \phi_{\ell,r}$ and $\theta \to \theta_{\ell,r}$.

S_{ij} and s_{ij} matrices are the part of the boundary conditions corresponding to the $2DEG$ interfaces with the ferromagnetic layers, F. As mentioned, when $i \neq j$, the matrix elements are zeroes. So, for $i = j$ we have S_{ij}

$$S_{11} = \left(E''_+ | E''_-\right) \tag{81}$$

$$S_{22} = \left(H''_+ | H''_-\right) \tag{82}$$

where

$$E''_+ = \begin{pmatrix} -e_{1R} & -e_{1L} \\ (-\frac{iq_{e1}}{\tilde{m}}\hat{1} - \lambda\hat{1}_a)e_{1R} & (\frac{iq_{e1}}{\tilde{m}}\hat{1} - \lambda\hat{1}_a)e_{1L} \end{pmatrix}$$

$$E''_- = \begin{pmatrix} -e_{2R} & -e_{2L} \\ (-\frac{iq_{e2}}{\tilde{m}}\hat{1} - \lambda\hat{1}_a)e_{2R} & (\frac{iq_{e2}}{\tilde{m}}\hat{1} - \lambda\hat{1}_a)e_{2L} \end{pmatrix}$$

$$H''_+ = \begin{pmatrix} -h_{1R} & -h_{1L} \\ (\frac{iq_{h1}}{\tilde{m}}\hat{1} - \lambda\hat{1}_a)h_{1R} & (-\frac{iq_{h1}}{\tilde{m}}\hat{1} - \lambda\hat{1}_a)h_{1L} \end{pmatrix}$$

$$H''_- = \begin{pmatrix} -h_{2R} & -h_{2L} \\ (\frac{iq_{h2}}{\tilde{m}}\hat{1} - \lambda\hat{1}_a)h_{2R} & (-\frac{iq_{h2}}{\tilde{m}}\hat{1} - \lambda\hat{1}_a)h_{2L} \end{pmatrix},$$

and for s_{ij} when $i = j$, we have

$$s_{11} = \left(E'''_+ | E'''_-\right) \tag{83}$$

$$s_{22} = \left(H'''_+ | H'''_-\right) \tag{84}$$

where

$$E'''_+ = \begin{pmatrix} e_{1R}\, e^{iq_{e1}d} & e_{1L}\, e^{-iq_{e1}d} \\ (\frac{iq_{e1}}{\tilde{m}}\hat{1} + \lambda\hat{1}_a)e_{1R}\, e^{iq_{e1}d} & (-\frac{iq_{e1}}{\tilde{m}}\hat{1} + \lambda\hat{1}_a)e_{1L}\, e^{-iq_{e1}d} \end{pmatrix}$$

$$E'''_- = \begin{pmatrix} e_{2R}\, e^{iq_{e2}d} & e_{2L}\, e^{-iq_{e2}d} \\ (\frac{iq_{e2}}{\tilde{m}}\hat{1} + \lambda\hat{1}_a)e_{2R}\, e^{iq_{e2}d} & (-\frac{iq_{e2}}{\tilde{m}}\hat{1} + \lambda\hat{1}_a)e_{2L}\, e^{-iq_{e2}d} \end{pmatrix}$$

$$H'''_+ = \begin{pmatrix} h_{1R}\, e^{-iq_{h1}d} & h_{1L}\, e^{iq_{h1}d} \\ (-\frac{iq_{h1}}{\tilde{m}}\hat{1} + \lambda\hat{1}_a)h_{1R}\, e^{-iq_{h1}d} & (\frac{iq_{h1}}{\tilde{m}}\hat{1} + \lambda\hat{1}_a)h_{1L}\, e^{iq_{h1}d} \end{pmatrix}$$

$$H'''_- = \begin{pmatrix} h_{2R}\, e^{-iq_{h2}d} & h_{2L}\, e^{iq_{h2}d} \\ (-\frac{iq_{h2}}{\tilde{m}}\hat{1} + \lambda\hat{1}_a)h_{2R}\, e^{-iq_{h2}d} & (\frac{iq_{h2}}{\tilde{m}}\hat{1} + \lambda\hat{1}_a)h_{2L}\, e^{iq_{h2}d} \end{pmatrix}$$

where $\hat{1}$ is the unitary 2×2 matrix, $\hat{1}_a = \begin{pmatrix} 0 & -1 \\ 1 & 0 \end{pmatrix}$, $\bar{m}$ is the normalized mass over the mass of the particles, on the left superconductor. We define the spinors $e_{1L,R}$, $e_{2L,R}$, $h_{1L,R}$ and $h_{2L,R}$ as

$$e_{1R} = \begin{pmatrix} ie^{-ia_1} \\ 1 \end{pmatrix}, \quad e_{1L} = \begin{pmatrix} -ie^{ia_1} \\ 1 \end{pmatrix}$$
$$e_{2R} = \begin{pmatrix} -ie^{-ia_2} \\ 1 \end{pmatrix}, \quad e_{2L} = \begin{pmatrix} ie^{ia_2} \\ 1 \end{pmatrix}$$
$$h_{1R} = \begin{pmatrix} -ie^{-ib_1} \\ 1 \end{pmatrix}, \quad h_{1L} = \begin{pmatrix} ie^{ib_1} \\ 1 \end{pmatrix}$$
$$h_{2R} = \begin{pmatrix} ie^{-ib_2} \\ 1 \end{pmatrix}, \quad h_{2L} = \begin{pmatrix} -ie^{ib_2} \\ 1 \end{pmatrix}$$

which are calculated from Eq. (47), when we solve for the angles $a1$, $a2$, $b1$, $b2$.

In Eq. (67), α and γ are four-component vectors, β^ℓ, β^r and η are eight component vectors. α contains the left superconductor's scattering amplitudes, in the order $e_\uparrow$, $e_\downarrow$, $h_\downarrow$, $h_\uparrow$, whereas β contains the right superconductor's coefficients, in the same order as α. Column vectors β^ℓ and β^r contain the coefficients corresponding to the ferromagnetic layers, which are in the order $\overrightarrow{e}_\uparrow$, $\overleftarrow{e}_\uparrow$, $\overrightarrow{e}_\downarrow$, $\overleftarrow{e}_\downarrow$, $\overleftarrow{h}_\uparrow$, $\overrightarrow{h}_\uparrow$, $\overleftarrow{h}_\downarrow$, $\overrightarrow{h}_\downarrow$. Column vector η corresponds to the $2DEG$ layer's coefficients, in the order $\overrightarrow{e}_1$, $\overleftarrow{e}_1$, $\overrightarrow{e}_2$, $\overleftarrow{e}_2$, $\overrightarrow{h}_1$, $\overleftarrow{h}_1$, $\overrightarrow{h}_2$, $\overleftarrow{h}_2$. The overhead arrow denotes the direction the particle is travelling to.

B_{ps} is a 32-column vector, determined by the left incident free states. In order to calculate the bound states and supercurrent, we have to consider a zero-incident amplitude. As a result, we set $B_{ps} = 0$, the part that defines the incident free states.

Solving the set of equations, in Eq. (67), gives us the coefficients that we need in order to fully determine the wavefunctions of stationary scattering states. Using Cramer's rule, we get the solution:

$$\alpha_{ps,p's'} = \frac{\Gamma^\alpha_{ps,p's'}}{\Gamma} \tag{85}$$

where Γ is the determinant of the 32×32 matrix in Eq. (67), and $\Gamma^\alpha_{ps,p's'}$ is the determinant of the same matrix, if we swap the corresponding to $\alpha_{ps,p's'}$ column, with B_{ps} vector. Therefore, in order to calculate the supercurrent, we use:

$$I = -\frac{e}{\hbar\beta} \sum_{\omega_n} \frac{1}{\Gamma(\chi, i\omega_n)} \frac{\partial\Gamma(\chi, i\omega_n)}{\partial\chi} \tag{86}$$

The determinant Γ of the 32×32 matrix of Eq. (67), depends only on the linearly independent solutions in the left, right and intermediate regions of the junction, and not on solutions of the BdG equations for specific incidence conditions. The supercurrent depends on the structure of the junction and not on the incident conditions.

In order to calculate the Γ determinant so that we can calculate the supercurrent from Eq. (86), we take the analytic continuation of the Matsubara frequencies, ω_n. Setting $\phi_L = 0$ and $\phi_R = \chi$, the phase difference is then χ. By the method of Laplace expansion, we isolate terms that have the same dependence on the phase difference χ. Thus, we can express the determinant as follows:

$$\Gamma(\chi, i\omega_n) = Acos2\chi + Bsin\chi + Ccos\chi + D \tag{87}$$

where $A,\ B,\ C,\ D$ are complicated functions of the parameters of the junction, but independent of χ. In general, they are $A(\omega_n, k_p),\ B(\omega_n, k_p),\ C(\omega_n, k_p),\ D(\omega_n, k_p)$. Substituting into Eq. (86), we get:

$$I = \frac{e}{\hbar\beta} \sum_{\omega_n} \frac{2Asin2\chi - Bcos\chi + Csin\chi}{Acos2\chi + Bsin\chi + Ccos\chi + D} \tag{88}$$

Therefore, knowing $A,\ B,\ C,\ D$ as a function of ω_n and k_p, we can calculate the supercurrent as a function of phase, very efficiently. In the above expression was written for a given k_p. In the end we must sum over all k_p values, in two dimensions, so that Eq. (88) becomes

$$I = \frac{e}{\hbar\beta} \sum_{k_p} \sum_{\omega_n} \frac{2Asin2\chi - Bcos\chi + Csin\chi}{Acos2\chi + Bsin\chi + Ccos\chi + D} \tag{89}$$

We use the Eq. (89) to calculate all supercurrent values in this thesis.

3 Simple Results

In this section, we aim to reproduce well known results of heavily studied Josephson junctions, such as the SNS, $S/2DEG/S$ and the SFS. The Andreev bound states of two-dimensional systems and the dependence of I_c, as a function of the junction parameters, will be compared to one-dimensional results.

3.1 S - Normal Metal - S (SNS) Josephson junction

The superconductor - normal metal - superconductor (SNS) Josephson junction has been examined thoroughly in the past. We briefly study the properties of clean weak links for ballistic short junctions, in which the mean free path of an electron, l, is larger that the distance between the superconductive electrodes, d, and the coherence length $\xi_0 = v_F/2\pi T_c$, in which the condition of the clean limit $l \gg \xi_0 = v_F/2\pi T_c$ is also fulfilled in the superconductive electrodes.

It has been shown [6], and already discussed in figure 1.4, that in clean SNS junctions, the current-phase relation (CPR) has a sinusoidal form at $T \simeq T_c$, but takes a saw-toothed curve at low T.

We examine the ballistic SNS junction when the interfaces between the normal metal and the superconductor are thin insulator (I) films capable of normal scattering. Double-barrier junction modify the supercurrent heavily, which depends linearly on the barrier transparency, due to coherent Cooper pair tunneling [7].

3.1.1 SNS Andreev bound states

The momentum mismatch at energy E of the electron-hole pair, leads to the loss of coherence and the phase shift due to branch crossing processes determine the bound states [4, 21, 13], called Andreev bound states. Andreev bound states are states that carry the supercurrent from one superconductor to the other. At zero voltage, an infinite number of Andreev reflections can, in principle, take place. The electrons and holes do not gain energy in the normal region from which they can not escape. This leads to bound states in the junction which carry the supercurrent, as discussed by Kulik [20].

We use an SNS junction with two normal scattering interfaces included in delta function potentials. That has been discussed by Chrestin *et al.* [22], using normal scattering in both interfaces of a Nb-p-InAs-inversion-layer-Nb system. As we have seen from section 1.4.2, Eq. (22), the supercurrent in short junctions can take a simple form. The phase difference due to the

traversal of the normal region does not play a role, so that $(k^+ - k^-)L \ll 1$. Solving the determinant for energy E we get Eq. (21)

$$E = \pm\Delta\sqrt{\frac{\cos^2\left(\frac{\phi}{2}\right) + Z^2}{1 + Z^2}}.$$

For $Z = 0$, meaning zero normal scattering at the interfaces, Eq. (21) becomes $E = \pm\Delta\cos(\frac{\phi}{2})$, a result Kulik [20] has produced. Comparing the result Kulik produced, in figure 1.3, with figure 3.1, we can see the bound states for a two-dimensional SNS junction, when calculated for normal incidence ($k_p = 0$).

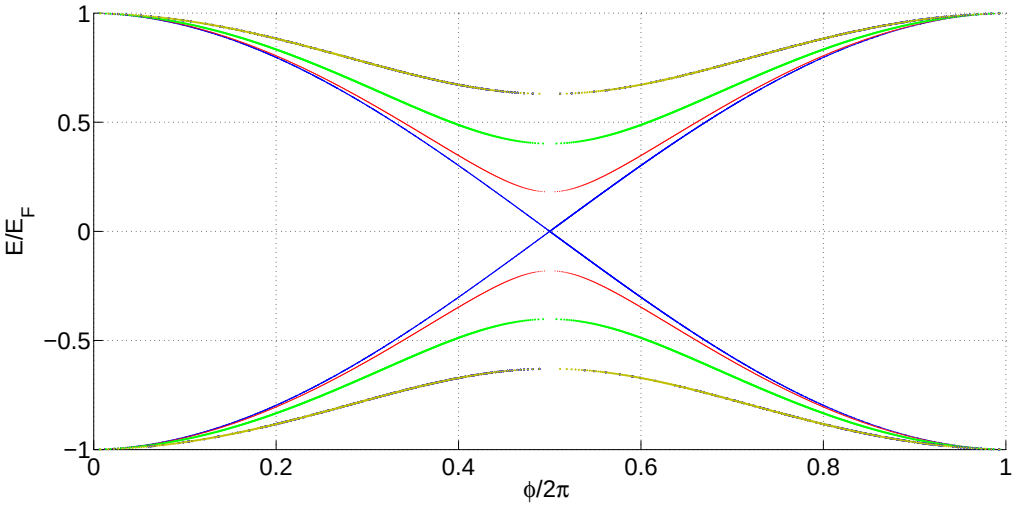

Figure 3.1: Andreev bound state energy versus superconductor phase difference, $T/\ T_c = 0.1$, Z_n varies from 0(blue line), 0.2(red line), 0.5(green line), 1(yellow line), $k_F d = 50$, measured at $k_p = 0$.

For increasing values of Z, we can see the gap at $\phi = \pi$ increasing. At $T = 0$, the bound state below the Fermi level can carry a supercurrent that depends on the superconductor phase difference, as described by Eq. (22)

$$I = -\frac{2e}{\hbar}\frac{dE}{d\phi}$$

We can calculate the current-phase relation (CPR) with figure 3.1 and Eq. (22). We can see that it agrees with the result produced by Eq. (21). At $\phi = 0$, the energy is $-\Delta, +\Delta$. That is what we call a 0-junction. Moreover, we observe that the missing points near $\phi = \pi$ are due to numerical reasons when $dE/d\phi$ tends to 0.

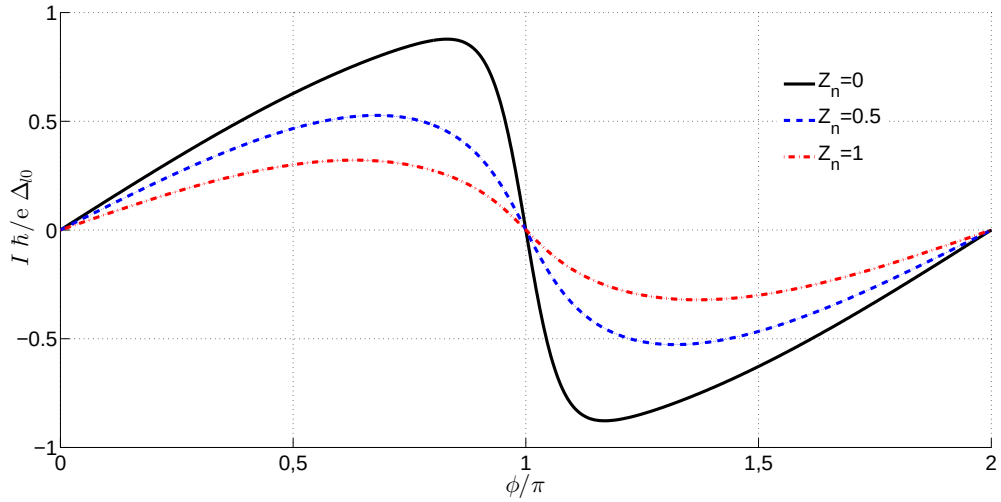

Figure 3.2: Current-Phase Relation, $T/T_c = 0.1$, $k_F d = 50$.

The numerical CPR for $Z_n = 0,\ 0.5,\ 1$ is consistent with the theoretical CPR of figure 1.4. We expect that at $T = 0$, the zero normal reflection graph will take a saw-tooth form, as in figure 1.4. At $Z_n = 0.5$, we observe that the CPR is very close to sinusoidal form. Generally, the maximum current for a given Z_n tends to move away from $\phi = \pi$ as normal scattering increases in strength.

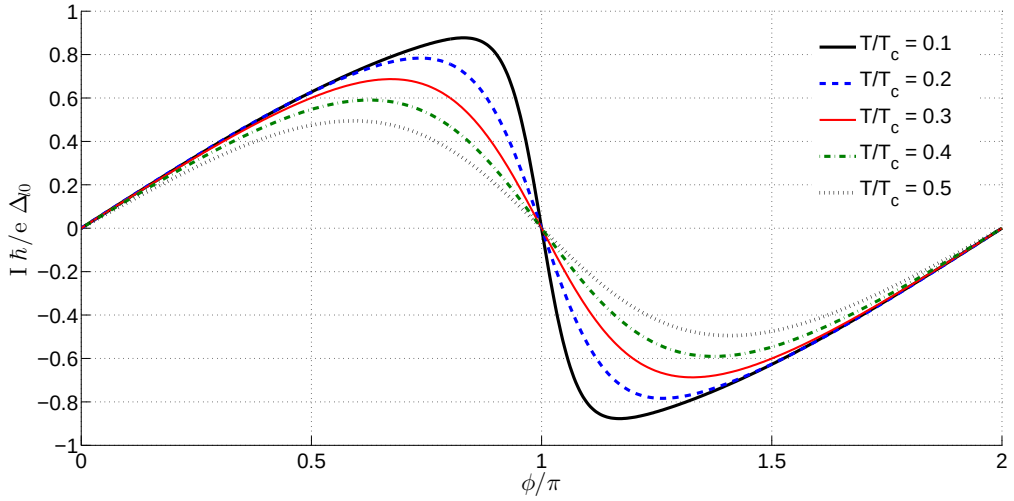

Figure 3.3: Current-Phase Relation, $k_F d = 50$, $Z_n = 0$.

In figure 3.2, the position of the critical current is displaced away from $\phi = \pi$ as Z_n increases, or as the temperature increases, in figure 3.3. Thus for

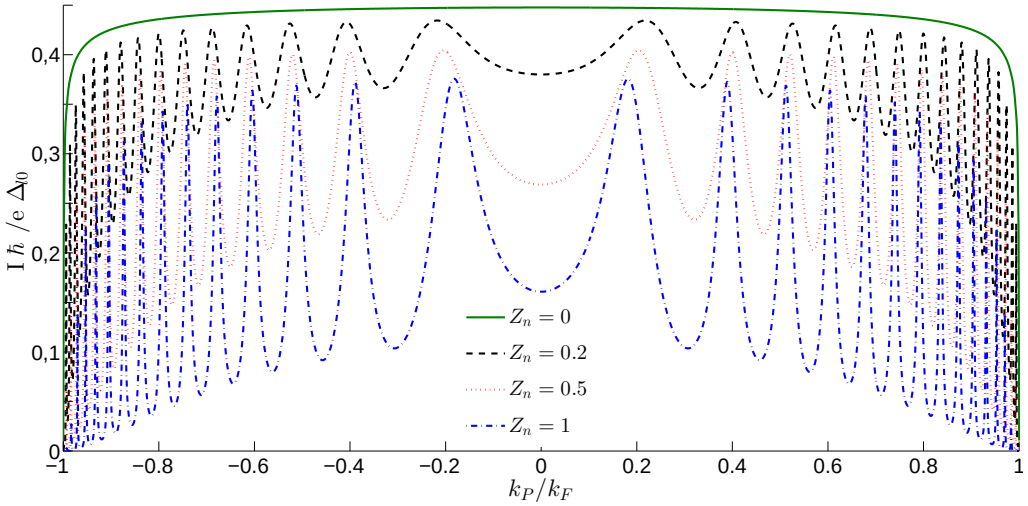

Figure 3.4: Current as a function of k_p/k_F, $T/T_c = 0.1$, $k_F d = 50$.

decreasing transmittance, the CPR transforms into a sinusoidal form. For small temperatures it has a saw-tooth form.

3.1.2 SNS critical current I_c

Supercurrent for a ballistic, junction at low temperatures, is calculated from Eq. (89), where we must sum up for all values of the parallel wavevector, $-1 \leq k_p \leq +1$. It is useful however, to see the contribution to the supercurrent, as a function of k_p, and this is plotted in figure 3.4. Due to the conservation of k_p from layer to layer, only the vertical wavenumber changes. The SNS junction has only one layer, the normal metal. We calculate the current versus k_p for the phase, ϕ, at maximum supercurrent.

In figure 3.4, supercurrent is calculated as a function of k_p for four different values of Z_n between 0 and 1. The contribution at $k_p = 0$ is not always the largest. When $Z_n = 0$, the interface normal scattering is zero, and as a result all k_p values (except the values close to $k_p = -1, 1$) contribute almost evenly to current. When we introduce interface normal scattering, specific values of k_p, for a given Z_n, contribute significantly more or less than the mean value. The oscillations in supercurrent are due to resonances in the normal region.

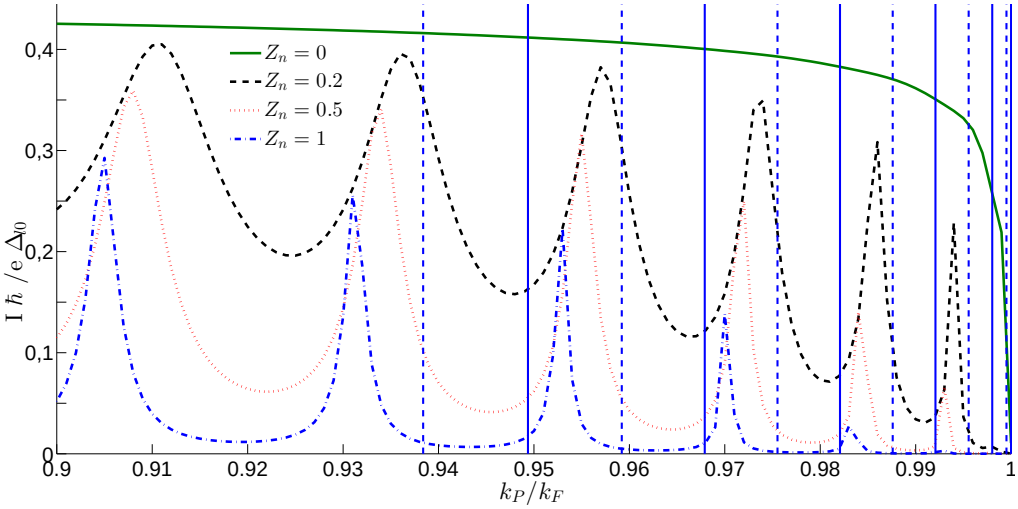

Figure 3.5: Current as a function of k_p/k_F, $T/T_c = 0.1$, $k_F d = 50$. k_p/k_F is limited to 0.9 to 1.

In figure 3.5 we limit $0.9 \leq k_p \leq 1$. The vertical lines correspond to resonances and anti-resonances due to normal scattering. The full lines denote a resonance and jagged lines denote an anti-resonance. The numbering is done from right to left, thus the full line on $k_p = 1$ is the first anti-resonance. The phase shift of electrons and holes is affected by the interface normal scattering. The corresponding peaks of each resonance, are displaced towards higher values of k_p, the higher the strength of normal scattering. In addition, the area of the current versus k_p for each line, which is the total respective supercurrent value, decreases as Z_n increases.

Increasing interface normal scattering decreases the critical supercurrent value. In figure 3.6, we calculate the critical current, I_c, for three different widths of the normal region, versus the normal scattering strength, Z_n. As a function of Z_n, the absolute value of critical current decreases as the width increases. The character of these three curves remains the same.

In figure 3.7 we observe how critical current is affected by an increase in temperature, for different values of normal scattering strength, Z_n. As expected, at $T = T_c$, superconductivity collapses, so the critical current vanishes, regardless of normal scattering strength.

3.2 S - Two-Dimensional Electron Gas - S ($S/2DEG/S$) Josephson junction

In spintronics, there is strong interest in the Rashba spin-orbit coupling (RSOC), which couples an electron's spin degree of freedom to orbital mo-

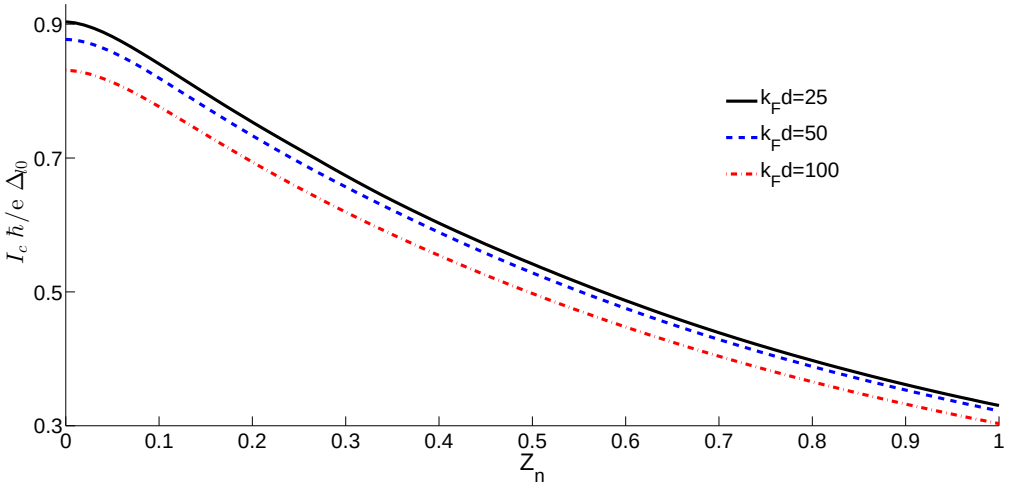

Figure 3.6: Critical current I_c as a function of the normal scattering strength Z_n, $T/T_c = 0.1$.

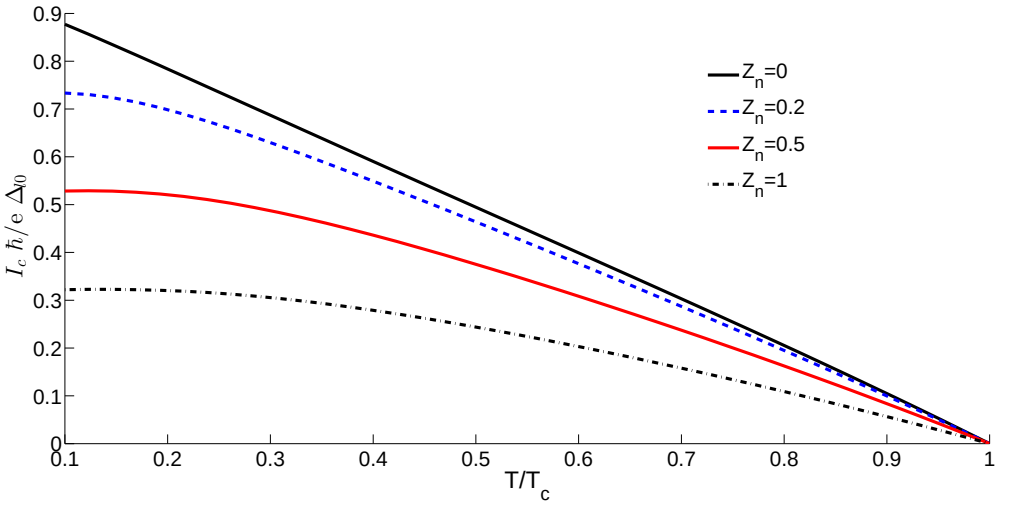

Figure 3.7: Critical current I_c as a function of the temperature (normalized on critical temperature T_c) for different scattering strengths, $k_Fd = 50$.

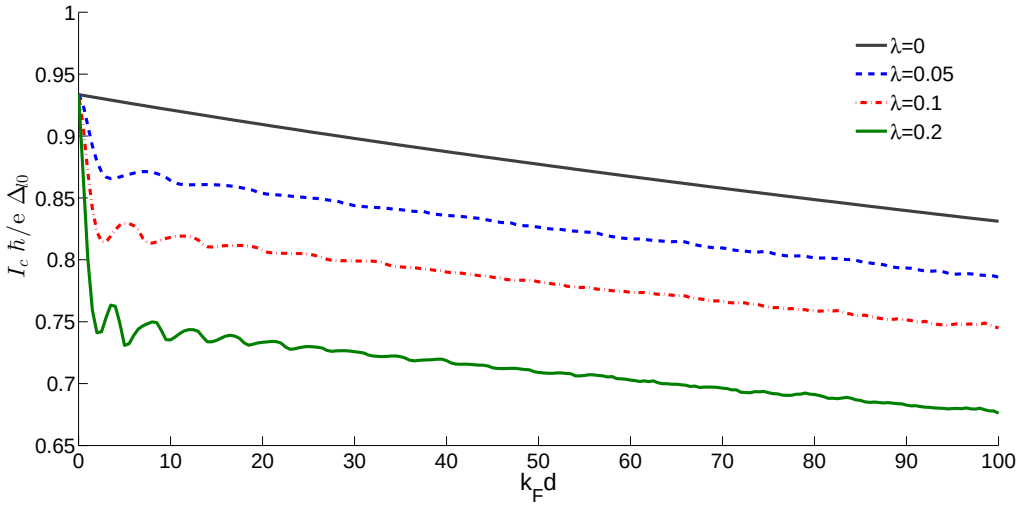

Figure 3.8: Critical current I_c as a function of width k_Fd, $T/T_c = 0.1$, $Z_n = 0$

tion. Motivated by the prospects in this area, studies are undertaken on incorporating RSOC in Josephson junctions [24, 25]. The first goal was to replace the ferromagnet, in SFS junctions, in the realization of $\pi-$junction and $0-\pi$ transition, by changing the spin-orbit coupling through an electric field. Even in the absence of an exchange field, the spin-orbit interaction splits the spin degeneracy of the Andreev levels for finite superconductive phase difference, χ. The coexistence of the spin-orbit coupling and Zeeman effect can give anomalous Josephson current [26, 27].

The $S/2DEG/S$ junction consists of two superconductors, and between them a 2-dimensional electron gas ($2DEG$). The $2DEG$ acts like a uniformly charged plane. It is placed on the xy plane, with x the vertical axis to the interfaces of the junction. Due to the asymmetry of the quantum well caused by dopping, $2DEG$ can exhibit Rashba spin-orbital interaction, which will modify carrier energies and trajectories based on their spin. We study the clean, ballistic, short $S/2DEG/S$ junction. Our study is not as extensive as the studies that have been done for this junction these two last decades. Our aim is to reproduce some basic and well established results, both as a point of comparison and as a code check. $S/2DEG/S$ remains a $0-$junction regardless of what parameters we change.

3.2.1 $S/2DEG/S$ critical current I_c

In chapter 3.1.2 we analyzed how the supercurrent changes as a function of an SNS junction's parameters. In this chapter, instead of a normal region, we place a two-dimensional electron gas on the xy plane.

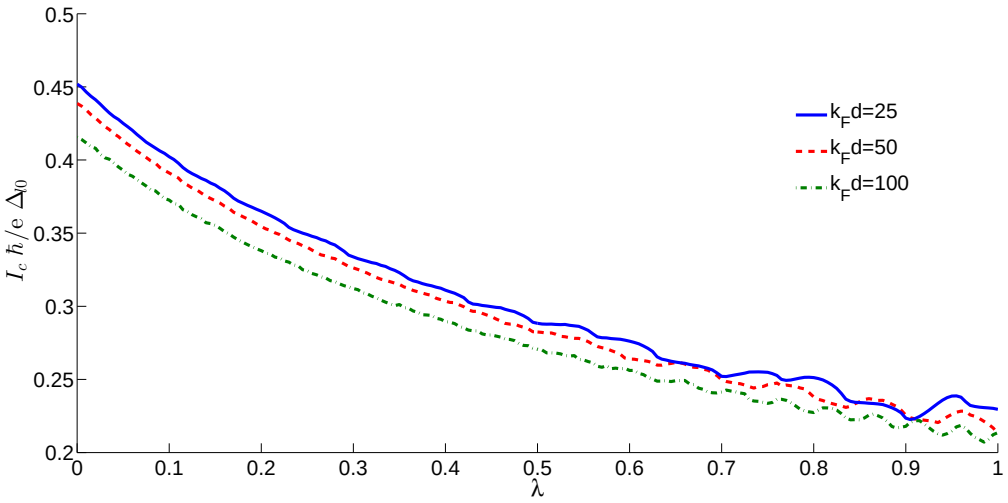

Figure 3.9: Critical current I_c as a function of the Rashba spin-orbit coupling constant λ, as seen for different widths $k_F d$, $Z_n = 0$, $T/T_c = 0.1$.

In figure 3.8 we compare the SNS junction ($\lambda = 0$) with the $S/2DEG/S$ junction ($\lambda \neq 0$). We study how the spin-orbit interaction affects critical supercurrent, as the width increases. The top full line is the critical supercurrent, I_c, of an SNS junction. The decrease of the supercurrent is almost linear. Increasing λ displaces the curves to lower critical supercurrent, while on the same time introduces oscillations, which die out for large values of width.

The effect of increasing spin-orbit interaction strength on the critical supercurrent, can be seen in figure 3.9. The critical supercurrent is calculated versus the Rashba spin-orbit coupling constant λ, for different widths of the intermediate layer, $k_F d$. As we can see, the supercurrent is reduced as the width is increased. Also, it is reduced as a function of spin-orbit interaction.

In figure 3.10, we calculate the critical supercurrent, as a function of the normal scattering strength, Z_n, for four values of λ. We see a displacement of the curves to lower critical supercurrent, as λ increases, and a smooth variation for increasing Z_n.

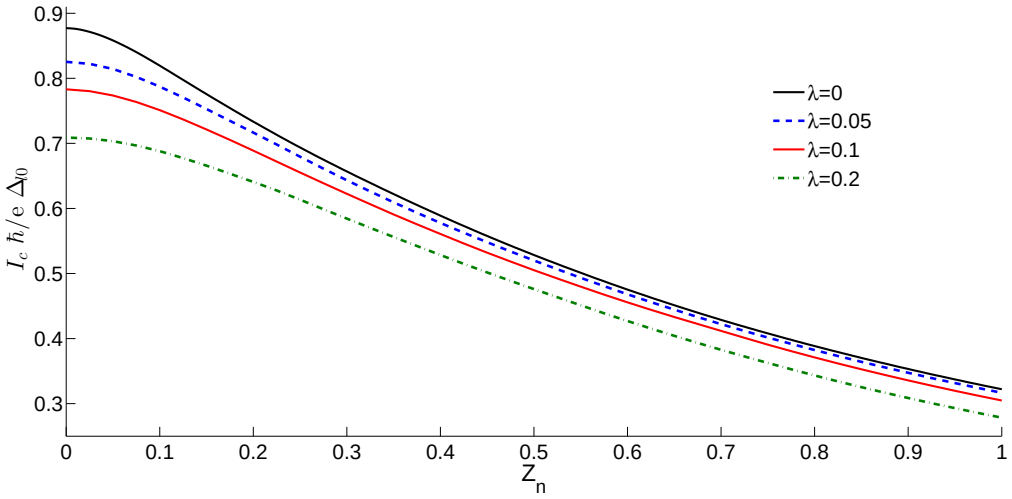

Figure 3.10: Critical current I_c as a function of scattering strength Z_n, as seen for different SOC parameters λ, $k_F d = 50$, $T/T_c = 0.1$.

3.3 S - Ferromagnet - S (SFS) Josephson junction

The SFS junction consists of two superconductors, and between them, a ferromagnet. The ferromagnet carries an arbitrary magnetization affecting spin states of the carriers. The two interfaces carry a magnetization that enables spin-flip scattering along with normal scattering. We will not do an extensive study of the SFS junction, as it has been done in the clean limit [14, 15, 16]. Our purpose is to provide a point of comparison, as well as code validation. We reproduce results from I. Margaris' *et al.* [28] study, taking into account the one-dimensional versus two-dimensional problem.

3.3.1 SFS zero-phase current I_{0P}

A non-coplanar set of magnetization vectors imparts to the junction a zero-phase current [28]. By changing the right interface's magnetization vector $\vec{Z}_{mR}$ we can observe in which geometries the junction has a zero-phase current.

We can observe that zero-phase current is significantly affected by normal scattering strength and interface magnetization scattering direction. In (a), we introduce an SFS junction, in which we change gradually the direction of the right interface magnetization vector along the xy plane. When the set of magnetization vectors becomes non-coplanar then we have finite zero-phase current. On the other hand, when the $\vec{Z}_{mR}$ is aligned with the x axis, whether it is $+x$ or $-x$, the zero-phase current vanishes. In (b), we calculated the

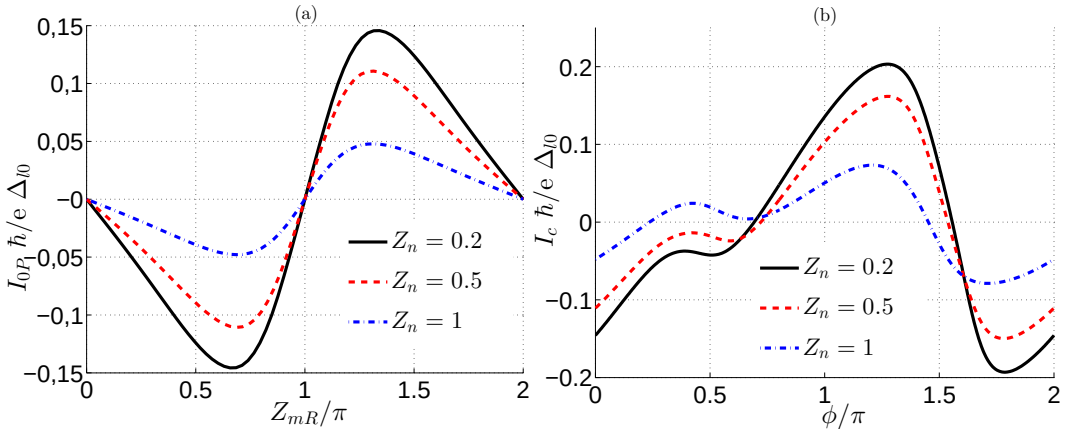

Figure 3.11: Zero-phase current versus (a) right interface's magnetization vector for three values of Z_n, and (b) Current-phase relation for $\vec{Z}_{mR}$ direction corresponding to maximum zero-phase current of (a). $T/T_c = 0.1$, $k_F d = 25$, $M = 0.8$, $Z_m = 1$. Geometry is $zx(xy)$.

current-phase relation for the corresponding three values of $\vec{Z}_{mR}$, for which the zero-phase current is maximum in (a), one for each Z_n value.

In figure 3.12, we increase Z_n and Z_m for (a) and (b) respectively, studying how zero-phase current is affected. In (a), the absolute zero-phase current decreases exponentially for Z_m equal 0.5 and 1, while for $Z_m = 2$ it reaches a maximum value around $Z_n = 1.25$. In (b), we observe that all three values of Z_n produce a peak in zero-phase current, but as Z_n values increase that maximum is displaced towards higher values of Z_m. These results are consistent with those in [28].

An SFS junction with non-coplanar set of magnetization directions zxy (read from left to right, left interface, layer, right interface) develops a zero-phase current. We study the effects of ferromagnet's width $k_F d$ as well as ferromagnet's magnetization strength M on the zero-phase current.
We observe in (a) as expected, the oscillations of the supercurrent as a function of width. In (b), as the magnetization strength approaches $M = E_F$, the results for figure 3.13 do not agree fully with the 1-dimensional results of [28]. In two dimensions, we see no sign changes in the supercurrent.

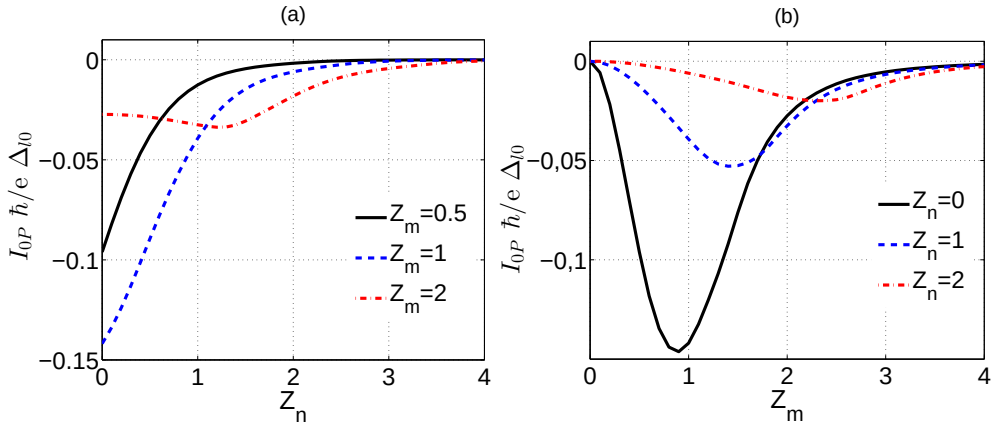

Figure 3.12: Zero-phase current versus (a) normal scattering strength Z_n, and (b) spin-flip scattering strength Z_m. $T/T_c = 0.1$, $k_F d = 25$, $M = 0.8$. Geometry is zxy.

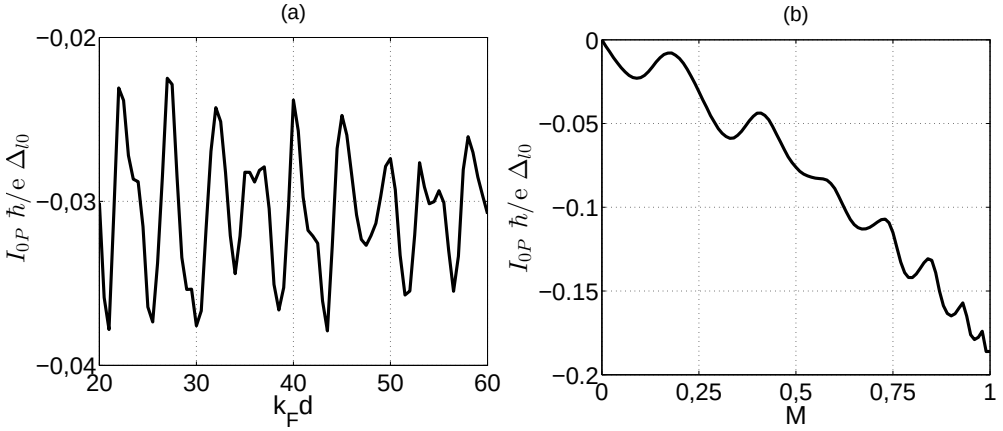

Figure 3.13: Zero-phase current versus (a) width $k_F d$, for $M = 0.5$, $Z_n = 1$, $Z_m = 1$, and (b) magnetization strength of ferromagnet M, for $k_F d = 25$, $Z_n = 0$, $Z_m = 1$. $T/T_c = 0.1$. Magnetization directions: zxy.

4 Results of the $SF/2DEG/FS$ junction

In section 2 we introduced the reader to the analysis of the $SF/2DEG/FS$ junction, whereas in section 3 we presented results of other junctions, for comparison and code validation. In this section we present the arithmetic results of the $SF/2DEG/FS$ junction. The junction consists of two superconductors (S), two ferromagnets (F) and a 2-dimensional electron gas ($2DEG$), while the SF and FS interfaces are spin active and have a normal scattering potential. The analysis is focused on the effect of the spin-orbit coupling on the supercurrent which is already modulated by ferromagnets. In section 3, we analyzed simple junctions. Comparing them to each other we observed that the modulation of the supercurrent between a $2DEG$ and a ferromagnet occurs in a different way.

4.1 Parameters of the $SF/2DEG/FS$ junction

We consider a short ballistic clean junction, so that we disregard diffusive characteristics. The junction has no inversion asymmetry, so we can neglect Dresselhaus spin-orbit coupling, and consider only Rashba spin-orbit effects where the asymmetry is caused by the $2DEG$. We also limit widths to $d < \xi_0$, so that the Andreev spectrum has few branches.

The junction consists of three layers between two superconductors. The layers are two ferromagnets and between them a $2DEG$. Each layer has different width, d_L for the left ferromagnet, d for the $2DEG$ and d_R for the right ferromagnet. Widths are normalized over the Fermi wavevector, k_F. For simplicity, the magnetization strength M is the same for the two ferromagnets, but not the direction, $\vec{M}_{L,R}$, of the magnetization vectors. Moreover, the interfaces between the ferromagnets and the superconductors have both spin-active magnetization Z_m and normal scattering potential Z_n. Magnetization strength, for both ferromagnets and interfaces, is normalized to the Fermi energy E_F. Spin-orbit coupling constant λ refers to the $2DEG$ and is normalized over the Fermi energy divided by the Fermi wavevector, E_F/k_F. Normal scattering strength Z_n is normalized over the Fermi energy divided by Fermi wavevector, E_F/k_F. For simplicity, we keep Z_n and Z_m the same in both interfaces, while we can independently change the magnetization vectors for Z_m, denoted as $\vec{Z}_{mL}$ and $\vec{Z}_{mR}$ respectively for the left and right interface. Temperature is regarded as uniform throughout the junction and is normalized to the critical temperature T_c. Lastly, the k_p wavevector depends on the incidence angle, its direction is vertical to the x axis, and it is normalized over the Fermi wavevector k_F.

Geometry is the direction of all the interface and ferromagnetic magnetization vectors of a junction. It is read from left to right, as the layers and interfaces are placed from left to right. Each component corresponds to the respective magnetization vector. Geometries can have two, three or four components. As an example, in section 3, we studied an SFS geometry with three components, zxy. Three-component geometries are for single layer and double interface junctions, with z and y being the magnetization vectors of the interfaces, whereas x being the vector of the ferromagnetic layer magnetization. Two and four-component geometries are used for junctions with double ferromagnet layers without or with interface magnetization respectively. Sometimes the vector of a magnetization may not be parallel to an axis, but on a plane. The plane vector will be put in brackets, in order to reflect this information. For example, in a junction with two interfaces and two ferromagnetic layers, the left layer has a magnetization vector on the xy plane. The geometry of that junction will read $x(xy)zy$. If the specific angle on that plane is needed, it will follow the plane components. As an example, for a magnetization direction in the xy plane with an angle of 30 degrees from x axis, the geometry will be $x(xy30)zy$, or $x(xy60)zy$ if it is 30 degrees from y axis.

4.2 Introductory Results

4.2.1 Current-phase relation types

The current-phase relation (CPR) for a junction can strongly affect the dynamical behaviour of a junction and drastically alter its form, as parameters change. We show five distinct $I(\phi)$ types; the 0-junction, the π-junction, the cosine-like ϕ-junction, the minus-cosine-like ϕ-junction and the general ϕ_0-junction.

Our goal in this section is to introduce the reader to $I(\phi)$ types, and not to the specific parameters used to obtain them. Values of supercurrent are not indicative of any certain $I(\phi)$ type.

The current as a function of the phase difference ϕ is given by

$$I_c = sin(\phi + \phi_0) \tag{90}$$

In figure 4.2, (a), $\phi_0 = 0$, therefore the supercurrent equals $I_c = sin(\phi)$ and thus called a 0-junction. When $\phi_0 = \pi$, $I_c = sin(\phi + \pi) = -sin(\phi)$, the junction is called π-junction.

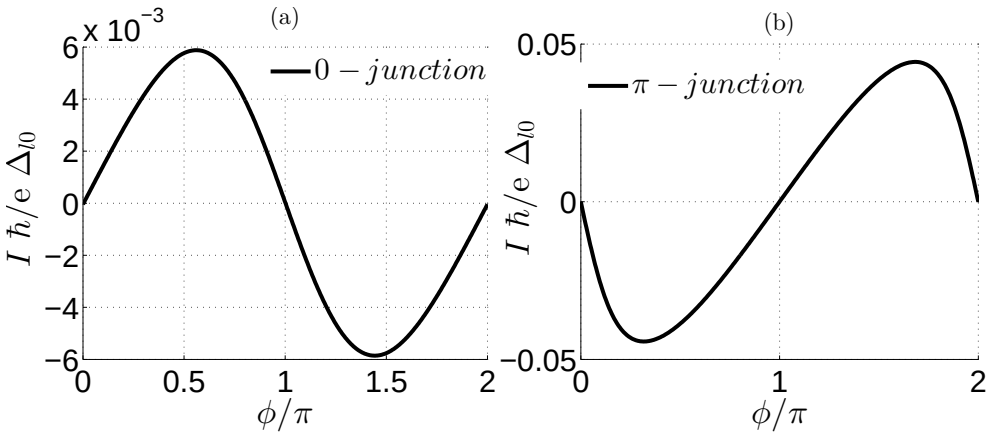

Figure 4.1: (a) 0-junction and (b) π-junction. $T/T_c = 0.1$, $M = 1$, $\lambda = 0.1$, $k_F d_{L,R} = 150$, $Z_m = 1$, $Z_n = 0$. Geometry is $yzxy$. $k_F d = 8.5$ for 0-junction, and $k_F d = 10$ for π-junction.

The shift in phase, ϕ_0, can be different than 0 or π. Then the junction is called a ϕ_0-junction. However, we can identify two more specific junctions that they can be separated from the general ϕ_0 type.

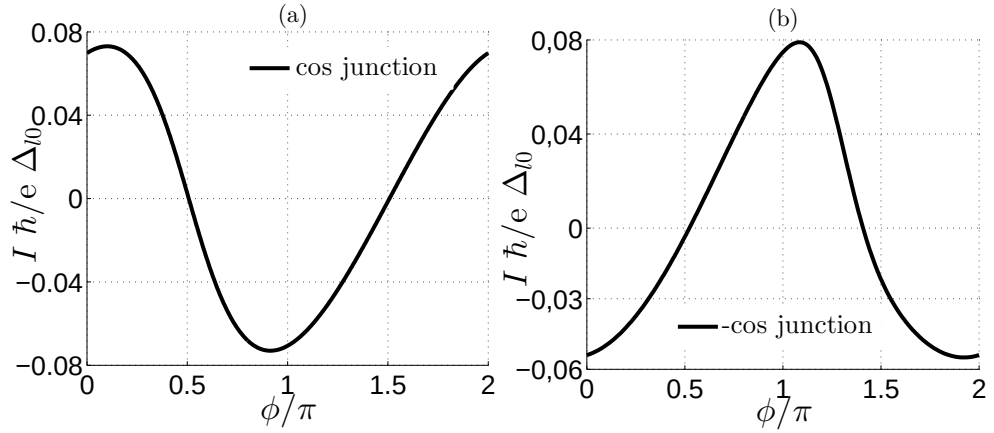

Figure 4.2: (a) cosine-like junction and (b) minus cosine-like junction. $T/T_c = 0.1$, $M = 1$, $\lambda = 0.1$, $k_F d = 50$, $k_F d_{L,R} = 150$, $Z_m = 1$, $Z_n = 0$. Geometry is $zyzy$ for cosine-like junction and $xyz(xy10)$.

When $\phi_0 = 3\pi/2,\ \pi/2$, the $I(\phi)$ relation can look like a cosine or minus-cosine function. In (a), the shift of phase is close to $\phi_0 = 3\pi/2$, and is regarded as a cosine-like junction, whereas in (b), $\phi_0 = \pi/2$ and the junction is then called a minus-cosine-like junction.

During the change of parameters on a junction, the form of the $I(\phi)$ can

be altered significantly. That is called a transition, from an $I(\phi)$ form to another.

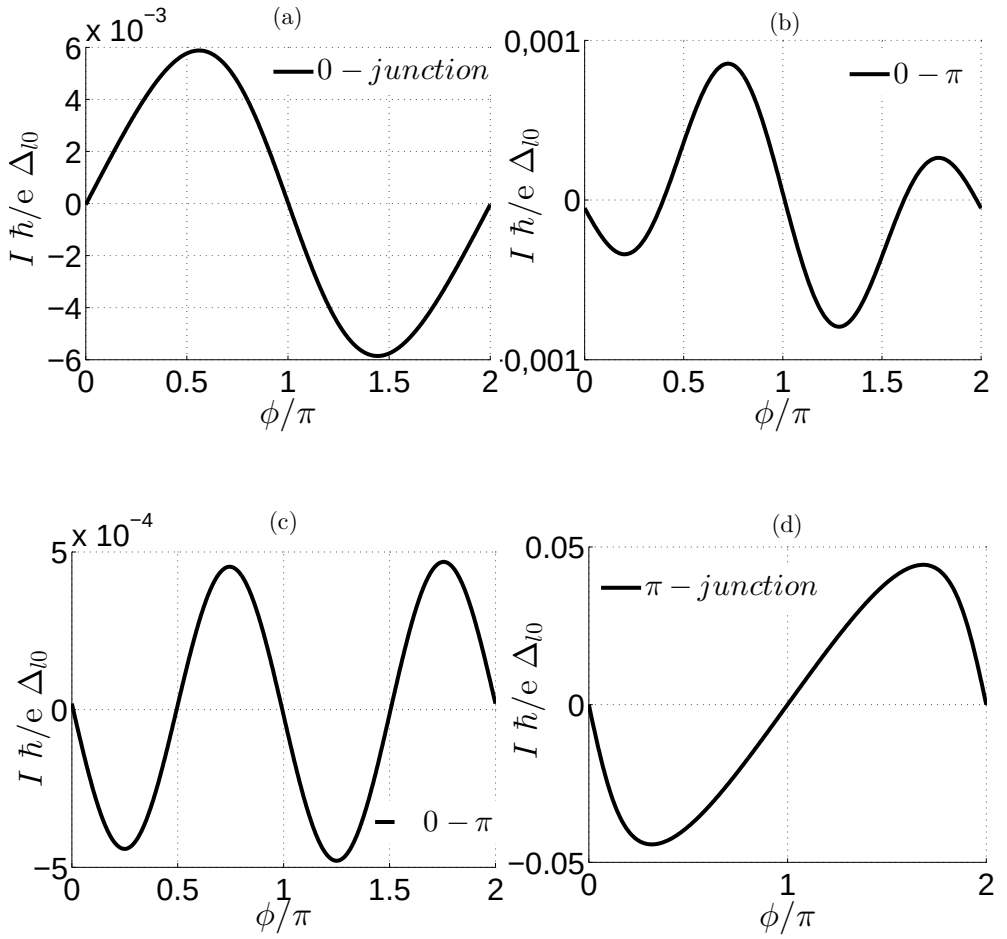

Figure 4.3: 0 to π transition. (a) 0-junction to (b) and (c) transition ϕ-junction, to (d) π-junction. $T/T_c = 0.1$, $M = 1$, $\lambda = 0.1$, $k_F d_{L,R} = 150$, $Z_m = 1$, $Z_n = 0$. Geometry is $yzxy$. $k_F d = 8.5$ for (a), $k_F d = 9$ for (b), $k_F d = 9.5$ for (c) and $k_F d = 10$ for (d).

As the width of the 2DEG, $k_F d$, increases the junction transitions from 0 (a) to π (d) type. As the junction changes from 0 to π-type, a second harmonic appears in the $I(\phi)$ relation, as is seen in (b) and (c). All 0 to π transitions go through (b) and (c), but not all $I(\phi)$ relations containing a second harmonic indicate a transition. Under specific circumstances, a transition can stop before it is completed, as the junction returns to the starting $I(\phi)$ relation. The $0 - \pi$ transition has been studied theoretically in the clean limit [16, 17, 18]

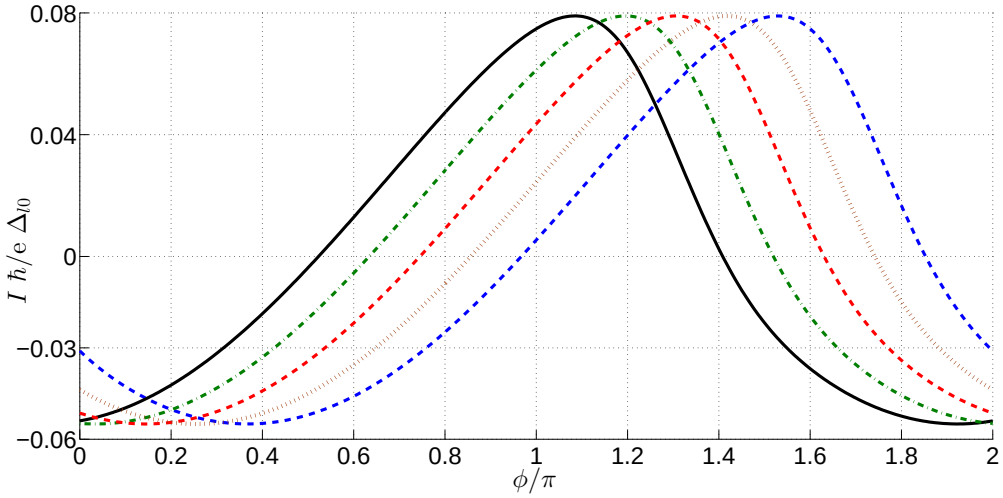

Figure 4.4: $-cos$-like to cos-like junction transition. $T/T_c = 0.1$, $M = 1$, $\lambda = 0.1$, $k_F d = 50$, $k_F d_{L,R} = 150$, Geometry is $xyz\vec{Z}_{mR}$, with $\vec{Z}_{mR}$ being changed from x axis to y axis.

Other ϕ_0 shifting examples include $-cos$-like to cos-like transitions, as we can see in figure 4.4. The $-cos$-like junction (full line) slowly shifts as the magnetization vector $\vec{Z}_{mR}$ is changed from $xyz(xy10)$ (full line) to $xyz(xy30)$ (jagged-with-dots line), to $xyz(xy50), xyz(xy70), xyz(xy90)$ respectively. The successive $I(\phi)$ relations denote generic ϕ_0-junctions. As the shift continues, the junction will fully transition to a cos-like junction.

4.2.2 Cut-off points

We consider the wavenumbers inside the ferromagnets and the 2DEG. While the value of these wavenumbers is a real number, the respective carrier plane wave can propagate inside the layer. So, for energies inside the gap

$$q_{ps} = \sqrt{1 + sM - k_p^2} \quad (ferromagnet) \tag{91}$$

$$q_{p2,1} = \sqrt{\left(\sqrt{1+\lambda^2} \pm \lambda\right)^2 - k_p^2} \quad (2DEG) \tag{92}$$

where $p = e, h$ is the particle counter, $s = +1(\uparrow), \ -1(\downarrow)$ the spin counter, and spin $2, 1$ corresponding to $+\lambda, -\lambda$ in Eq. (92). In the ferromagnet, the spin $\downarrow$ vector becomes imaginary above a critical k_p which depends on the magnetization. For the $2DEG$ layer, depending on the spin-orbit coupling constant, spin-mode 1 can become imaginary. Then, the carrier plane wave gets damped and can not continue to propagate inside the layer. We define

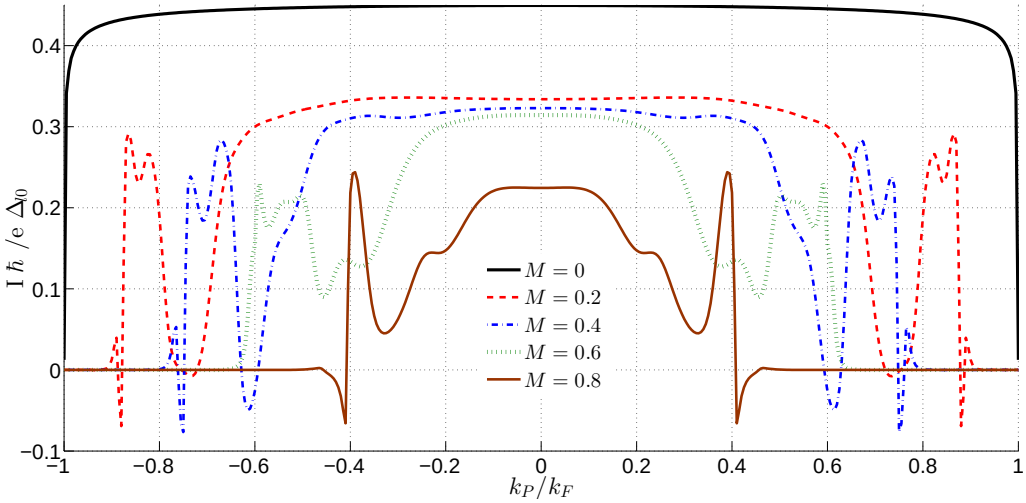

Figure 4.5: Cut-off k_p points for different values of magnetization M. $T/T_c = 0.1$, $\lambda = 0$, $k_F d = 15$, $k_F d_{L,R} = 15$, $Z_{n,m} = 0$, Geometry is zx.

the value of k_p, above which the wavenumber becomes imaginary, as the cut-off point for a specific value of λ and M.
In figure 4.5 we can see the k_p values above which the current vanishes, for each value of M. When $M = 0$, the cut-off point is $k_p = 1$. We can calculate the exact k_p by setting $q_{ps} = 0$ in Eq. 91. For $s = -1$ and $M = 1$, the wavevector is $q_{ps} = \sqrt{-k_p^2}$. This happens for all k_p values (cut-off point at $k_p = 0$). Thus, there is no propagation for $s = -1(\downarrow)$. $M = 1$ state is called the half-metallic limit, since spin $\uparrow$ propagates while spin $\downarrow$ decays. Therefore, we can calculate the spin $\downarrow$ cut-off in k_p, for any value of M.

The same principle can be applied, in order to calculate the cut-off points for the spin-orbit interaction on the $2DEG$. When $q_{p1} = 0$, the value of k_p calculated is the cut-off point. We observe that the cut-off for the spin-orbit interaction of the $2DEG$ is a sudden and abrupt reduction of supercurrent. In contrast to the magnetization case, the supercurrent does not vanish after the cut-off point. The cut-off point for $\lambda = 0.2$ is at $k_p = 0.82k_F$, for $\lambda = 0.6$ is at $k_p = 0.565k_F$ and so on. After the cut-off point, the supercurrent continues to take non-zero values, until $k_p = 1$. This non-zero current is due to spin 2 states that exist in $2DEG$.

Ferromagnet cut-off is different to the spin-orbit cut-off because of the $2DEG$ spin states. Whereas in ferromagnets, only two spin states exist, $\uparrow$ and $\downarrow$, in $2DEG$, spin modes 1 and 2 change as a function of k_p. In ferromagnets, above the cut-off point, only one spin state survives, spin $\uparrow$, while spin $\downarrow$ is suppressed. When a carrier with that spin is Andreev reflected, it will

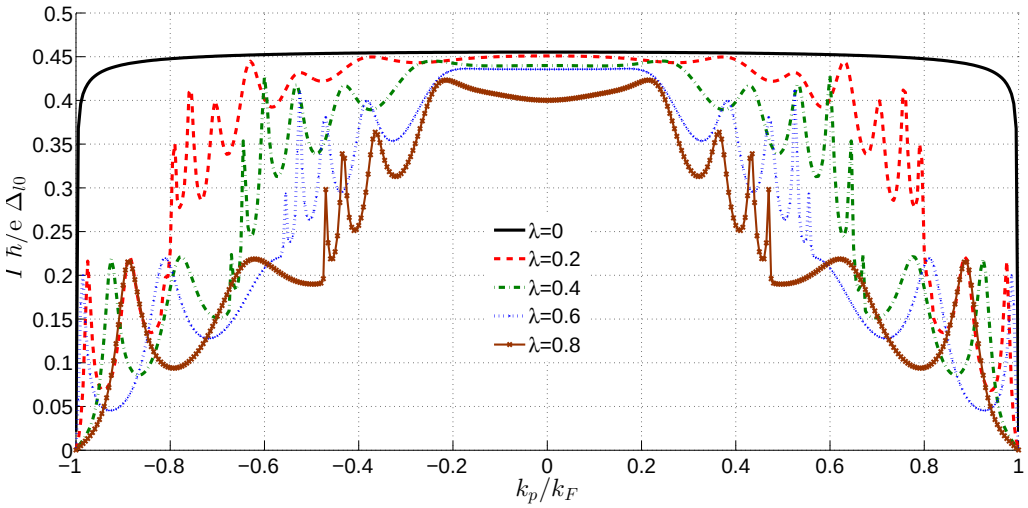

Figure 4.6: Cut-off k_p points for different values of spin-orbit coupling constant λ. $T/T_c = 0.1$, $M = 0$, $k_F d = 15$, $k_F d_{L,R} = 15$, $Z_{n,m} = 0$.

produce an opposite carrier with the opposite spin. The opposite spin can not propagate inside the ferromagnet. This process does not enable Cooper pairs to pass through the junction, which gives zero supercurrent. The spin mode 1 has cut-off points in k_p, as spin-orbit coupling increases. However, spin mode 2 carriers are reflected both into spin mode 1 and spin mode 2, which have both spin $\uparrow$ and $\downarrow$ components. Thus, they can propagate without decay.

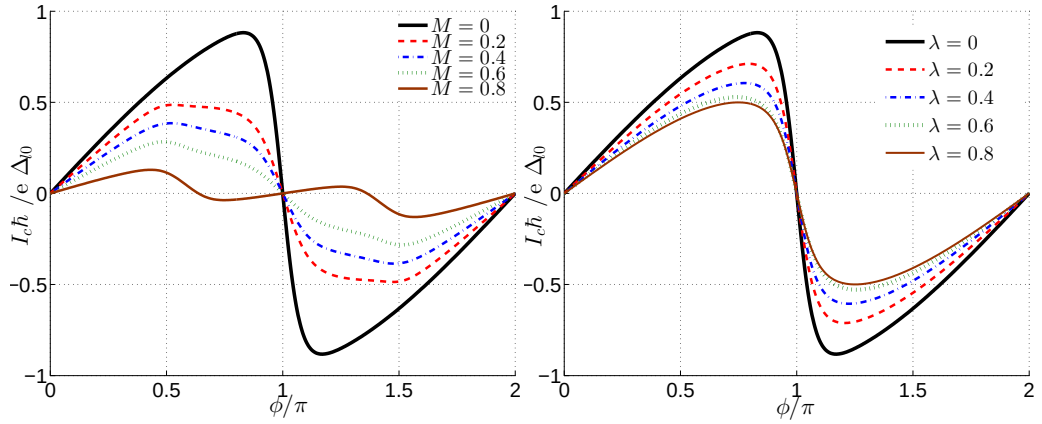

Figure 4.7: Current-phase relation (CPR) for (a) $\lambda = 0$, M varies from 0 to 0.8, and for (b) $M = 0$ and $\lambda = 0$ to 0.8. $T/T_c = 0.1$, $Z_{n,m} = 0$, $k_F d = 15$, $k_F d_{L,R} = 15$. Geometry is zx.

In figure 4.7 we calculate the current-phase relations corresponding to figures 4.6 and 4.5. In (a), we change magnetization strength, M. In $M = 0.8$ the current-phase relation transitions from 0 to π. In (b), we change spin-orbit coupling constant, λ. The character of the current-phase relations does not change as λ increases.

4.3 Two-dimensional distribution of current

In order to calculate the current-phase relation we integrate the supercurrent distribution for all possible angles of incidence (sum over all k_p values). In the supercurrent versus k_p graph, we can observe cut-offs, resonances and anti-resonances due to normal scattering.

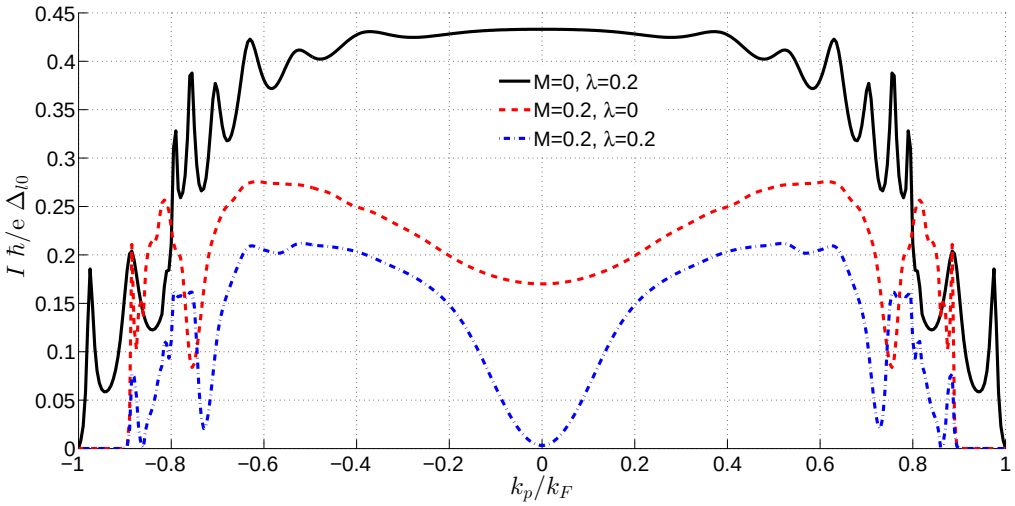

Figure 4.8: Supercurrent as a function of k_p/k_F for different values of M and λ. $T/T_c = 0.1$, $Z_{n,m} = 0$, $k_F d = 30$, $k_F d_{L,R} = 25$, Geometry is zx.

In figure 4.8, we calculate the supercurrent as a function of the parallel wavevector k_p. Supercurrent versus k_p is always calculated on the phase ϕ of the absolute maximum value of supercurrent in the respective $I(\phi)$ relation (CPR). For $M = 0.2$, the cut-off point is at $k_p = 0.894 k_F$, whereas for $\lambda = 0.2$, cut-off point is at $k_p = 0.82 k_F$. As we can observe, the cut-off points do not change. They are not affected by the presence of each other. On the other hand, the general character of current can change dramatically when both M and λ are present. For normal incidence ($k_p = 0$), in dashed-with-points line, supercurrent has vanished. Normal incidence does not produce a supercurrent for these parameters, which is not the case for both the other cases.

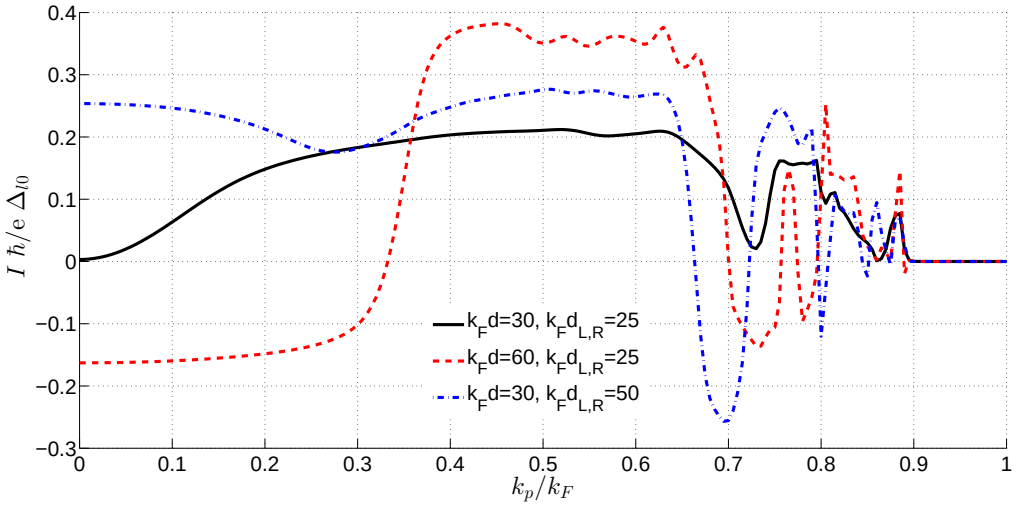

Figure 4.9: Supercurrent as a function of k_p/k_F for different values of k_Fd and $k_Fd_{L,R}$. $T/T_c = 0.1$, $Z_{n,m} = 0$, $M = 0.2$, $\lambda = 0.2$, Geometry is zx.

For $M = 0.2$ and $\lambda = 0.2$, in figure 4.9, we change the width of the layers, k_Fd and $k_Fd_{L,R}$. Supercurrent versus k_p is calculated on the maximum value of $I(\phi)$. We focus on $0 \leq k_p \leq 1$, as $k_p < 0$ is symmetrical. We observe that the cut-off points do not change as a function of width, and depend only on M and λ. Peaks and dips increase in number, as the increased width introduces more normal resonances and anti-resonances. Also, for vertical incidence ($k_p = 0$), supercurrent increases for the two dashed-line curves. We argue that the occurrence of zero supercurrent at $k_p = 0$ was less of a coincidental and more of a periodicity phenomenon.

As M increases, the cut-off point shifts towards smaller k_p. In figure 4.10, we set $k_Fd = 30$ and $k_Fd_{L,R} = 25$ while increasing M substantially. Supercurrent versus k_p is calculated on the maximum value of $I(\phi)$. Note that x axis is limited to $k_p = 0.4$, focusing on the non-zero supercurrent values. Supercurrent distribution for $M = 1$ vanishes as the cut-off point is $k_p = 0$. The cut-off points for $M = 0.9,\ 0.95$ are at $k_p = 0.316,\ 0.223$, after which, the supercurrent distribution tends to zero values. As we approach the half-metallic limit ($M = 1$), the total supercurrent distribution is reduced rapidly for all geometries consisting of only ferromagnetic layers (2-component ferromagnet geometries).

In figure 4.11, we do not change widths compared to figure 4.10. We decrease M by a small amount, so that $M = 0.8$, and we change the spin-orbit coupling constant λ. Supercurrent versus k_p is calculated on the maximum value of $I(\phi)$. At zero incidence ($k_p = 0$), supercurrent decreases non-

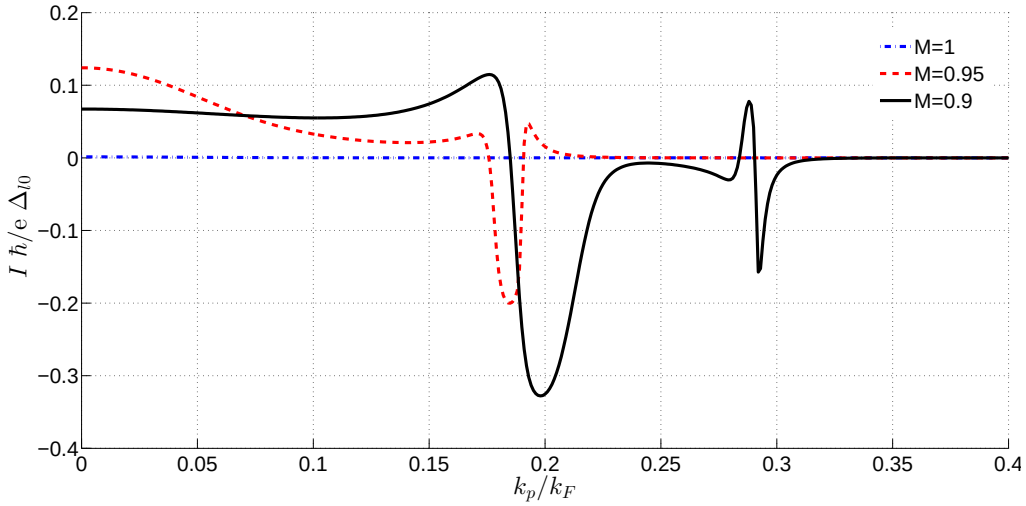

Figure 4.10: Supercurrent as a function of k_p/k_F for different values of M. $T/T_c = 0.1$, $Z_{n,m} = 0$, $\lambda = 0.2$, $k_F d = 30$, $k_F d_{L,R} = 25$. Geometry is zx.

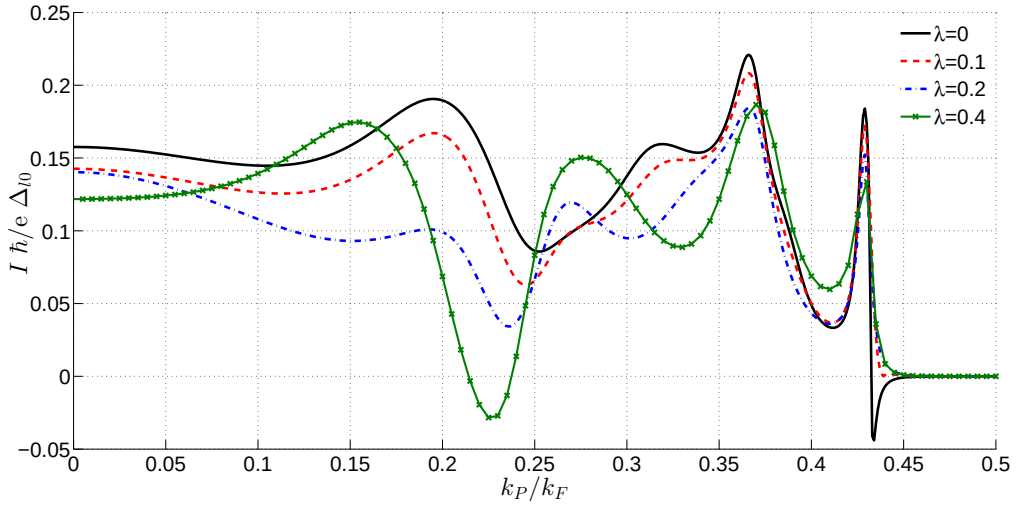

Figure 4.11: Supercurrent as a function of k_p/k_F for different values of λ. $T/T_c = 0.1$, $Z_{n,m} = 0$, $M = 0.8$, $k_F d = 30$, $k_F d_{L,R} = 25$. Geometry is zx.

monotonically as λ increases. The cut-off point for $M = 0.8$ is $k_p = 0.447$. For $\lambda = 0.4$, supercurrent has a negative value. The supercurrent value as a function of k_p, tends to oscillate more intense as λ increases. In addition, all curves have a common cut-off due to the magnetization, at $k_p = 0.447$.

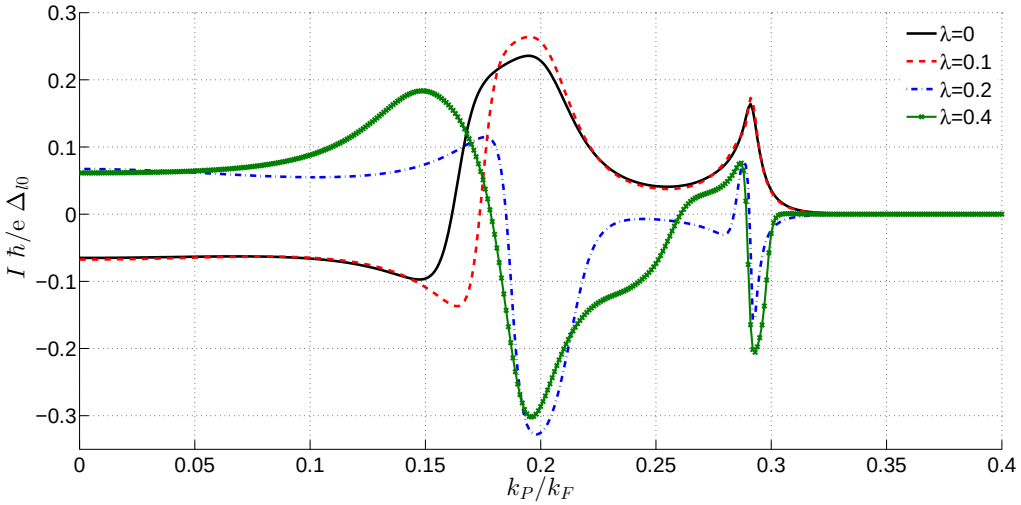

Figure 4.12: Supercurrent as a function of k_p/k_F for different values of λ. $T/T_c = 0.1$, $Z_{n,m} = 0$, $M = 0.9$, $k_F d = 30$, $k_F d_{L,R} = 25$. Geometry is zx.

In figure 4.12, we change $M = 0.9$ when compared to figure 4.11. Supercurrent versus k_p is calculated on the maximum value of $I(\phi)$. Supercurrent distribution for $\lambda = 0$ and 0.1 are almost identical for $0.14 \geq k_p/k_F \geq 0.22$, while also assuming a negative value for $k_p/k_F \leq 0.16,\ 0.17$. The reason is that while λ assumes low values, magnetization M is very strong and dominates these two values of λ. That seems to change when λ is increased. From 0.2 and above, supercurrent starts at positive values and its dependence from k_p stays roughly the same.

In figure 4.13 we calculate the respective CPR for the same values of λ, corresponding to figures 4.11 and 4.12. For $M = 0.8$ in (a), the supercurrent as a function of the phase difference ϕ does not seem to change significantly for low values of λ, despite the obvious reduction in value. For $\lambda = 0.4$, the maximum value of the supercurrent is higher than that of $\lambda = 0.2$, leading to an oscillation in supercurrent as a function of λ. In (b), M is increased to 0.9. For $\lambda = 0$, the junction is of 0-type. As λ increases, it changes from a 0-junction to a π-junction, for $\lambda = 0.2$. With increased $\lambda = 0.4$, the junction returns to a 0-type. Again, the maximum value of supercurrent oscillates as a function of λ.

In figure 4.14 we set $M = 1$, while we change the interface magnetization

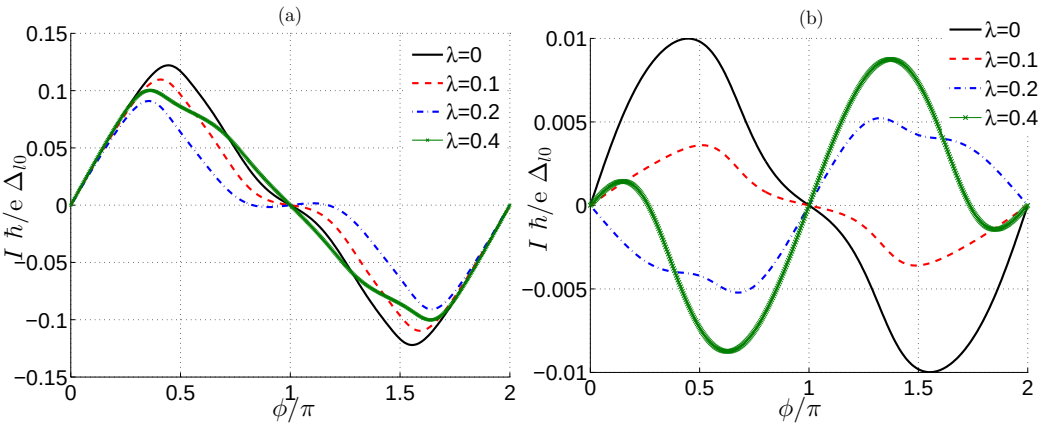

Figure 4.13: Current-Phase Relation (CPR) for different values of λ. For (a) $M = 0.8$ and (b) $M = 0.9$. $T/T_c = 0.1$, $Z_{n,m} = 0$, $k_F d = 30$, $k_F d_{L,R} = 25$. Geometry is zx.

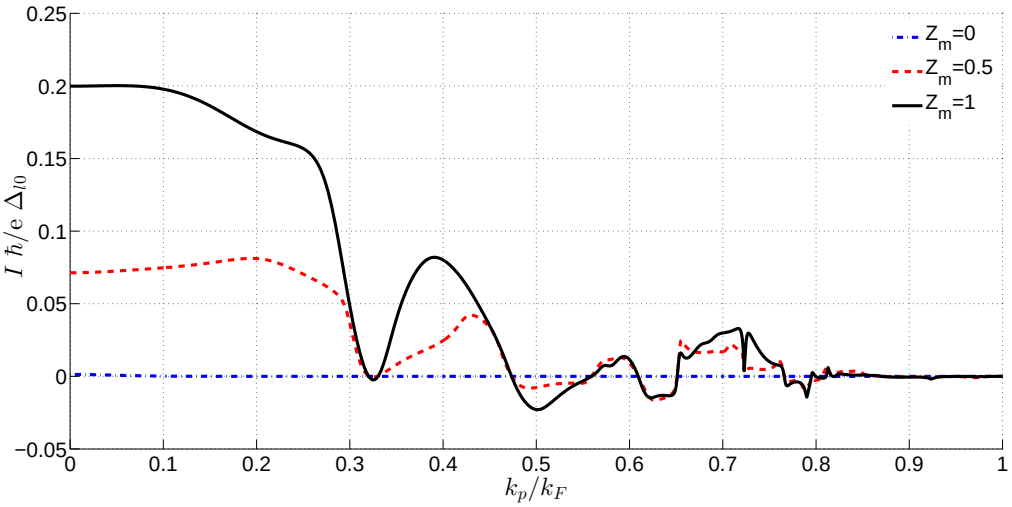

Figure 4.14: Current as a function of k_p/k_F for different values of Z_m. $T/T_c = 0.1$, $Z_n = 0$, $M = 1$, $\lambda = 0.2$, $k_F d = 30$, $k_F d_{L,R} = 25$. Geometry is $yzxy$.

strength. When $Z_m = 0$, the geometry is zx. In figure 4.10 we concluded that the supercurrent distribution of 2-component geometries, consisting of only ferromagnets, is reduced to zero at the half-metallic limit ($M = 1$). As Z_m increases, the supercurrent distribution assumes non-zero values. Geometry changes to $yzxy$.

The reason, outlined in our discussion about figure 4.5, is that while spin $\uparrow$ can propagate through the ferromagnetic layers, spin $\downarrow$ decays exponentially and can not propagate. We consider an FS (or SF) interface. The process that enables Cooper pairs to pass through the ferromagnet F, is the Andreev reflection. The Andreev reflection, in a non spin-active FS interface, occurs normally for $k_p \leq$ cut-off k_p, until the magnetization assumes $M = 1$ value. In the half-metallic limit, spin $\downarrow$ can not propagate through the F layer for all k_p. We assume a carrier, with spin $\uparrow$, that hits the interface while moving through the ferromagnet. As it is Andreev reflected, an opposite carrier is retroreflected, with the opposite spin (spin $\downarrow$). Following the above statement, this opposite carrier decays inside the F layer and therefore the supercurrent decreases to zero. An exception to the above argument would be that when the ferromagnet's layer is small enough, the reflected opposite carrier with spin $\downarrow$ effectively is not stopped by a thin potential barrier. Quantum mechanically, it can tunnel through the barrier with a probability that decreases as the energy of the carrier is decreased, as well as the potential and the width of the barrier are increased. We will show, in figure 4.21, that tunneling of these carriers, with spin $\downarrow$, is relevant for widths $k_F d_{L,R} \leq 7$ and potential strength $M = 1$. After that value, effectively the supercurrent vanishes, as the probability for a tunneling to occur decreases exponentially with width.

In the previous paragraph we analyzed what happens to the Andreev reflection on an SF interface when it is not spin-active. When the interface is spin-active, the supercurrent does not vanish even for increased widths of the ferromagnetic layers. We consider an SFS junction, with spin-active interfaces, where $M = 1$ and $Z_m = 1$. Inside the ferromagnetic layer, spin $\downarrow$ does not propagate. An incident carrier, with spin $\uparrow$, hits the FS interface. We distinguish two different cases. In the first case, ferromagnetic magnetization vector $\vec{M}$ is parallel to the interface magnetization vector $\vec{Z}_{mR}$. As a result, spin $\uparrow$ is an eigenstate of both the ferromagnet and interface magnetization. So, the carrier can propagate normally, and the spin-active interface does not affect the carrier's spin. The carrier is reflected into an opposite carrier with spin $\downarrow$, and the process produces no supercurrent. In the second case, $\vec{M}$ is not parallel to $\vec{Z}_{mR}$. As the eigenstates of the ferromagnetic magnetization and the interface are now different, the carrier hits the interface and its spin is affected. Depending on the angle between the two magnetization

vectors, spin $\uparrow_F$ has a chance of either becoming spin $\uparrow_I$ or $\downarrow_I$, where $_F$ and $_I$ denote the layer, ferromagnet and interface. We consider both situations. The carrier is reflected into the opposite carrier with spin either $\downarrow_I$ or $\uparrow_I$. The opposite carrier is retroreflected and enters the ferromagnet. Spin $\downarrow_I$ becomes either spin $\uparrow_F$ or $\downarrow_F$, and spin $\uparrow_I$ also becomes either spin $\uparrow_F$ or $\downarrow_F$. If the opposite carrier ends with spin $\downarrow_F$ it decays. However, there is always a probability that the carrier can end with spin $\uparrow_F$ regardless of the spin state it possessed inside the interface. We extend our claim to the left interface, where the same process occurs, if $\vec{M}$ is not parallel to $\vec{Z}_{mL}$. Two Andreev reflections after the first incidence, there is a clear probability of a carrier with spin $\uparrow_F$ retracing the steps of the first carrier. This process outlined above, induces *triplet correlations*, and differs from the normal double Andreev reflection on the spin of the opposite carrier (before the second Andreev reflection). In normal double Andreev reflection, the opposite carrier has exclusively only spin $\downarrow$ when it hits the interface, as only *singlet correlations* are induced, whereas for *triplet correlations* the opposite carrier has both spin $\uparrow$ and $\downarrow$.

To resolve any complications, we should note that only one spin carrier is considered for the process, despite the fact that Andreev reflection changes any spin into its opposite. Also, we note that *triplet correlations* can exist outside the half-metallic limit, and coexist with *singlet correlations* in two-ferromagnet junctions ($SFFS$), and also double spin-active interface junctions (S_IF_IS), while the magnetization strength is $M < 1$. When $M = 1$, in the half-metallic limit, *singlet correlations* do not exist. Thus, the only way to produce supercurrent is by induced *triplet correlations*.

In figure 4.15, magnetization strength is $M = 1$, and $Z_m = 1$, enabling triplet correlations. For (a), $\lambda = 0$, we calculate supercurrent as a function of k_p for different geometries. Supercurrent distribution for $xyzx$ and $zxzy$ has the same value, for all k_p values. For $k_p > 0.2$, the distribution is the same for $xyzx$, $zxzy$ and $zyzy$ geometries, which is the full line. Without the spin-orbit coupling we expect that as long as the $\vec{Z}_m$ vectors are vertical to the neighbouring $\vec{M}$, their direction will not affect the supercurrent distribution. On the other hand, when $\vec{M}$ are vertical to each other ($xyzx$, $zxzy$ and $zyzy$), the supercurrent distribution assumes the same value. Despite the fact that for the three geometries with vertical ferromagnetic layers, we obtain almost the same distribution for k_p values greater than 0.2, nevertheless there is a deviation in supercurrent for $k_p \leq 0.2$. Parallel $\vec{M}$ geometry $xyyx$, has a completely different supercurrent distribution when compared to the other three geometries. The argument that supercurrent is primarily modulated by the angle between the two ferromagnetic vectors $\vec{M}$ is reinforced by the

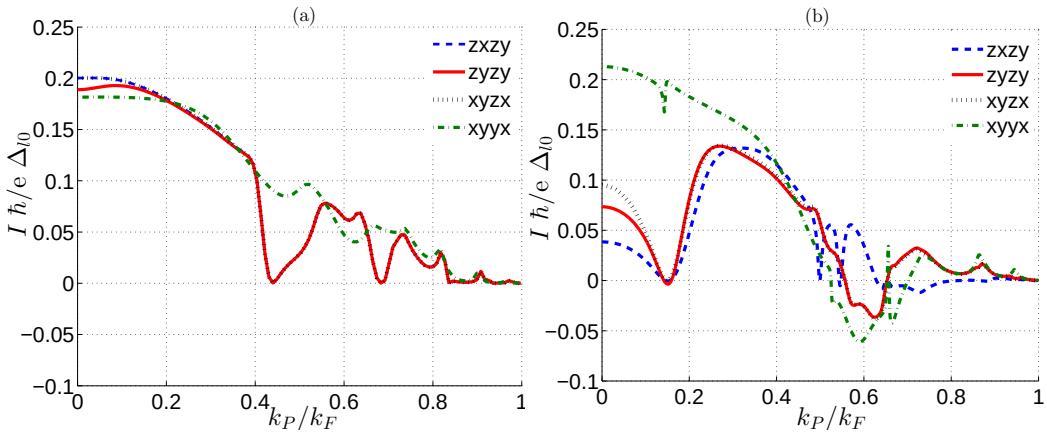

Figure 4.15: Supercurrent as a function of k_p/k_F for different geometries, for (a) $\lambda = 0$ and (b) $\lambda = 0.4$. $T/T_c = 0.1$, $M = 1$, $Z_n = 0$, $Z_m = 1$, $k_F d = 15$, $k_F d_{L,R} = 15$.

results of $xyyx$ geometry, when no spin-orbit interaction is present.

Continuing the discussion on figure 4.15, in (b), we enable spin-orbit coupling, setting $\lambda = 0.4$. Before, we argued that when ferromagnetic layer directions, $\vec{M}$, are vertical to each other, the modulation on the supercurrent distribution is the same. With spin-orbit coupling, supercurrent distribution values for vertical $\vec{M}$ geometries are quite different, especially for normal incidence. While for $\lambda = 0$ and vertical $\vec{M}$ layers, the supercurrent distribution was the same (when $k_p > 0.2$), for $\lambda = 0.4$ only $zxzy$ and $xyzx$ remain the same. Supercurrent distribution for geometry $zxzy$ is different for all k_p values. For the geometry $xyyx$, the distribution is different regardless of $\lambda = 0$. Lastly, comparing the current distributions of the geometries, we see that the maximum value of supercurrent, which is the sum of all k_p values, is about the same in case (a). Whereas in (b) the current for geometry $xyyx$ is quite different (higher than the other three). The corresponding current-phase relation graphs, in figure 4.16, validate the above argument, when we observe the maximum value of the critical current.

Considering the cases outlined in figure 4.15, we calculate the current-phase relation of each, for both $\lambda = 0$ and 0.4. In figure 4.16 (a), we set $\lambda = 0$. Geometry $zyzy$ is a 0-junction, whereas $xyzx$ and $xyyx$ are π-junctions. Finally $zxzy$ is a $-cos$-junction. Geometries $xyzx$ and $zxzy$ have a zero-phase current. That is expected, as they form a non-coplanar set of magnetization vectors. Moreover, the geometries $zyzy$ and $xyyx$ that do not form a non-coplanar set, do not introduce zero-phase current. The maximum value of the supercurrent seems to be constant for the geometries with vertical $\vec{M}$

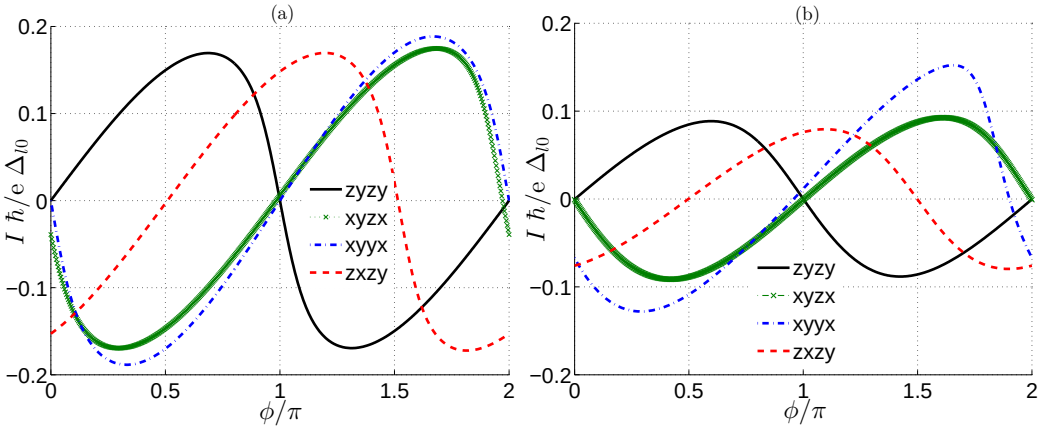

Figure 4.16: Current-Phase Relation (CPR) for different geometries. (a) $\lambda = 0$ and (b) $\lambda = 0.4$. $T/T_c = 0.1$, $M = 1$, $Z_m = 1$, $Z_n = 0$, $k_F d = 15$, $k_F d_{L,R} = 15$.

layers, whereas $xyyx$ displays the highest value of supercurrent, as expected from the supercurrent distribution in figure 4.15. In (b), we increase spin-orbit coupling to $\lambda = 0.4$. Supercurrent values decrease for all geometries. In addition, geometry $zyzy$ has the same character as before, a 0-junction with no zero-phase current. In (a), geometry $xyyx$ was a π-junction with no zero-phase current. With active spin-orbit interaction, it produces a significant zero-phase current. We argue that due to the plane structure of the $2DEG$ layer, on xy plane, it produces an electric field parallel to z axis. This electric field is translated to a magnetic field when electrons traverse the region. The magnetic field is induced across the xy plane. So, while geometry $xyyx$ forms a coplanar set of magnetization vectors, so that no zero-phase current is expected, when we introduce spin-orbit coupling, a significant zero-phase current is observed. Geometry $zyzy$ does not produce a zero-phase current despite the fact that it can form a non-coplanar set, if the magnetic field is induced on x axis. On the other hand, geometry $zxzy$ is not affected by the introduction of spin-orbit interaction. Geometry $xyzx$, which forms a non-coplanar set of magnetization vectors, as expected, shows zero-phase current even without the spin-orbit interaction. However, when we enable spin-orbit coupling (for the specific value of λ), its zero-phase current disappears.

In figure 4.17, in the geometry $xyzy$, we plot for four values of λ, we plot the supercurrent versus k_p at a phase where $I(\phi)$ has its maximum value, which can be different for each λ. The supercurrent distribution for $\lambda = 0$ is positive for all k_p, while for $\lambda \neq 0$, the supercurrent distributions also take negative values. There are no distinct features on the k_p cut-off points, for

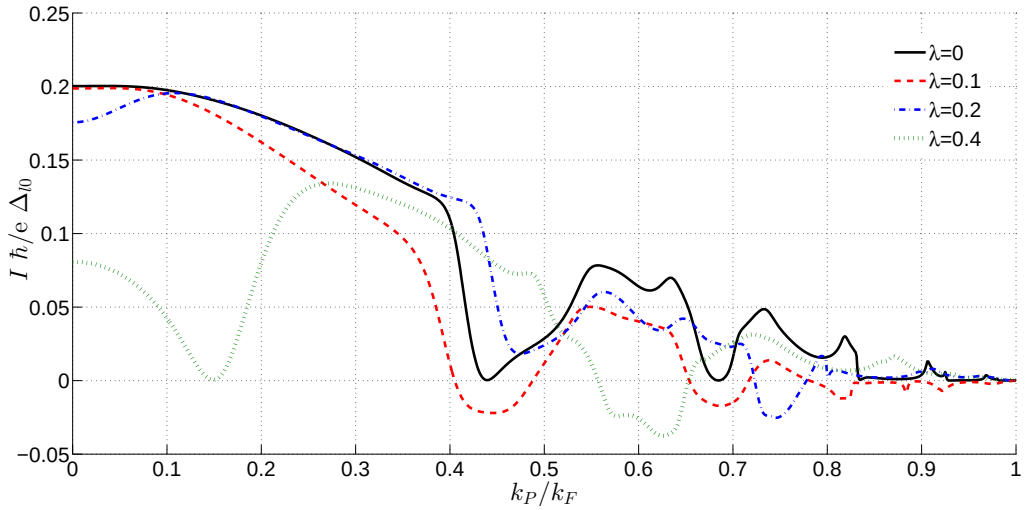

Figure 4.17: Current as a function of k_p, for different values of spin-orbit coupling constant λ, $T/T_c = 0.1$, $k_F d = 15$, $k_F d_{L,R} = 15$, $M = 1$, $Z_m = 1$, $Z_n = 0$. Geometry is $xyzy$.

each λ. It is possible that k_p cut-off points, for weak spin-orbit coupling, are dominated by the strength of the magnetization $M = 1$.

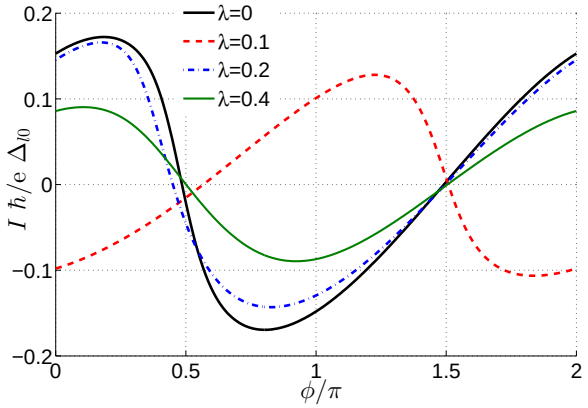

Figure 4.18: Current-phase relation (CPR) for different values of spin-orbit coupling constant λ, $T/T_c = 0.1$, $k_F d = 15$, $k_F d_{L,R} = 15$, $M = 1$, $Z_m = 1$, $Z_n = 0$. Geometry is $xyzy$.

Continuing the analysis from figure 4.17, we calculate current-phase relation for the four values of spin-orbit interaction, for $xyzy$ geometry. For $\lambda = 0$, the junction starts as a cos-like one. For values $\lambda = 0.1,\ 0.2$ it is clear that it transitions from a cos-like junction to a $-cos$-like one, as λ changes.

It is certain that, between $0.2 \leq \lambda \leq 0.4$, the junction has changed from cos-like to $-cos$-like and back.

4.4 Critical current

In section 3 we discussed some results for SNS, SFS and $S2DEGS$ junctions. The critical supercurrent can vary widely as the parameters change. We use results in section 3 as a guide, while we proceed to study the $S/F/2DEG/F/S$ junction. A direct comparison between the critical supercurrent values of the basic junctions and the $S/F/2DEG/F/S$ junction should be avoided or be taken into context, as the effects produced by each layer are different.

In the first two figures, 4.19 and 4.20, RSOC constant λ is the only parameter that is changed. In figure 4.19 the spin-orbit constant is $\lambda = 0$, making the 2DEG layer effectively a normal metal, whereas in figure 4.20 spin-orbit constant is changed into $\lambda = 0.1$. Both types of interface scattering are $Z_{n,m} = 0$. As we already discussed in section 4.1, magnetization strength in ferromagnetic layers is kept the same, and here it is set $M = 0.2$. We plot the critical current as a function of the right ferromagnet's magnetization direction $\vec{M}_R$. $\vec{M}_R$ starts aligned with z axis, changes to x (along the zx plane), then y axis (along the xy plane), and back to z (along the yz plane). $\vec{M}_L$ is kept constant for each branch, z, x and y for blue (full), green (dashed with dots) and red (dashed) respectively. The geometry is two-component, which means it only has two ferromagnetic layers and no spin-active interfaces.

For $\lambda = 0$, the $2DEG$ layer is a normal metal. We observe a strong correlation between the critical current and the angle between $\vec{M}_L$ and $\vec{M}_R$. The critical current is periodic for each two-layer geometry. As magnetization directions $\vec{M}_L$ and $\vec{M}_R$ remain vertical to each other, the critical current remains constant. There are several apparent symmetries. xz is equal to zx, xy is equal to yx and zy is equal to yz. Also, as long as the plane of $\vec{M}_R$ shares one component with the $\vec{M}_L$, the critical current assumes the same value, when $\vec{M}_R$ is on 45' of that plane.

In figure 4.20 we introduce a non-zero spin-orbit interaction, setting $\lambda = 0.1$, and as a result the symmetries, observed in figure 4.19, break. While still remaining periodic, critical current is a complex function of $\vec{M}_R$. In general, it is sensitive on the exact geometry, but on the same time it has retained two symmetries. The numerical calculations show the same result for the xy and the symmetric yx geometry, while the same is true for zy and yz geometries. Moreover, whereas in figure 4.19, the critical current was constant and maximum to a value of around $I_c(\lambda = 0)|_{max} = 0.4$, in 4.20

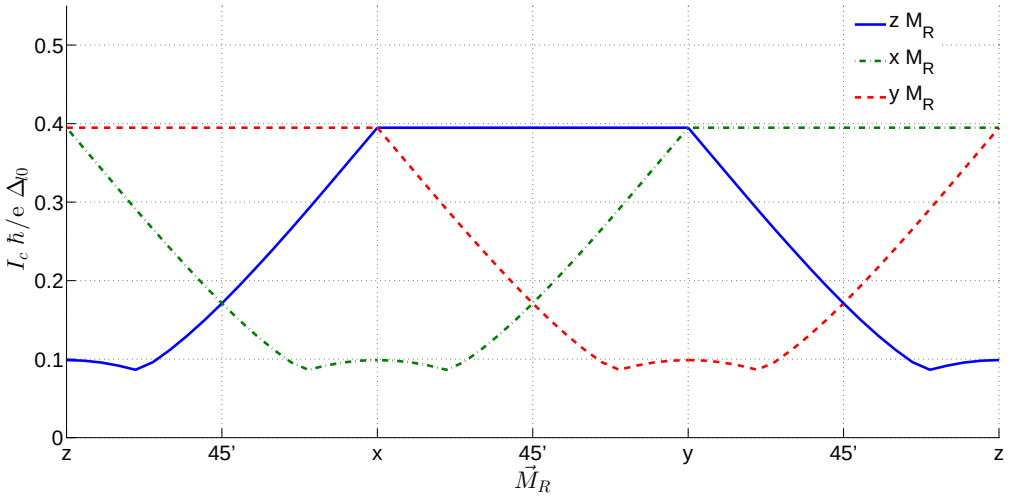

Figure 4.19: Critical current I_c as a function of the direction of right ferromagnet's magnetization vector, for different magnetization directions of the left ferromagnet, $T/T_c = 0.1$, $k_F d = 25$, $k_F d_{L,R} = 25$, $M = 0.2$, $\lambda = 0$, $Z_{n,m} = 0$.

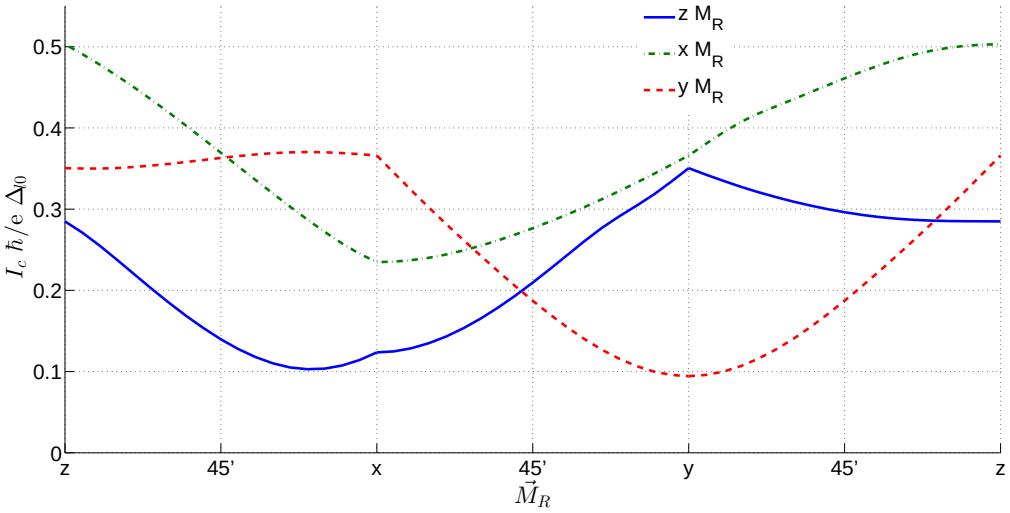

Figure 4.20: Critical current I_c as a function of the direction of right ferromagnet's magnetization vector, for different magnetization directions of the left ferromagnet, $T/T_c = 0.1$, $k_F d = 25$, $k_F d_{L,R} = 25$, $M = 0.2$, $\lambda = 0.1$, $Z_{n,m} = 0$.

geometry xz, it reaches a maximum critical current of $I_c = 0.5$, while zx geometry reaches only an $I_c = 0.125$.

In figure 4.20 we observed that geometry xz has an increased supercurrent for $I_c = 0.5$, when compared to all other potential geometries. xy geometry has an $I_c = 0.35$. Critical supercurrent values are sensitive to the geometry of the junction, when $\lambda \neq 0$. During the next figures, 4.21 and 4.22, we change the ferromagnets' width and the magnetization M strength, in order to test if xz geometry has the strongest supercurrent regardless of magnetization.

In figure 4.21 we change both ferromagnets' width $k_F d_{L,R}$ in a uniform manner, while testing for four magnetization strength values. The geometry is xy, while the $2DEG$ width is kept constant at $k_F d = 25$.

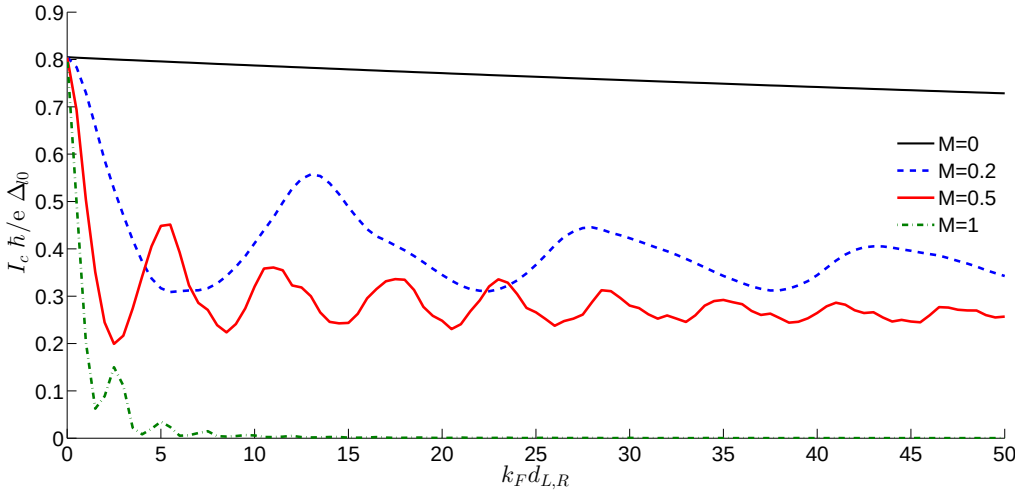

Figure 4.21: Critical current I_c as a function of the ferromagnets width $k_F d_{L,R}$, for different magnetization strength values M, $T/T_c = 0.1$, $k_F d = 25$, $\lambda = 0$, $Z_{n,m} = 0$. Magnetization directions are xy.

For $M = 0$, we emulate the $S/N/2DEG/N/S$ junction. Increasing magnetization strength M introduces oscillations while also decreasing the mean value of the supercurrent. As magnetization strength M increases, both the oscillations' period and the amount of resonances due to normal reflections are increased.

It is important to mention that for $M = 1$ (half-metallic limit) the supercurrent gets diminished in an exponential manner, with the oscillations being damped. The reason is that for $M = 1$, the wavevectors from $q_{e,s} = \sqrt{1 + sM - k_p^2}$, become

$$q_{e,\uparrow} = \sqrt{2 - k_p^2} \tag{93}$$

$$q_{e,\downarrow} = \sqrt{-k_p^2} \tag{94}$$

so that for any k_p, $q_{e,\downarrow}$ becomes imaginary. A planar wave with imaginary exponential decays and effectively vanishes after a small length. The result is that $q_{e,\downarrow}$ can not propagate through the ferromagnets of the junction. Moreover, $q_{h,\downarrow}$ also becomes imaginary and can not propagate. Imagine an electron with spin $\uparrow$ hitting the FS interface. The hole with spin $\downarrow$ that is reflected gets immediately damped and can not propagate. The sequence is broken, and after a while no Andreev reflections occur, thus the supercurrent vanishes. This consideration does not take into account the tunneling effect which allows carriers with imaginary wavenumbers to pass through a thin layer (probability reduced when width increased). We see the tunneling effect in figure 4.21, as critical current $I_c \neq 0$ for widths $k_F d_{L,R} < 7$, when $M = 1$.

In figure 4.22 we change the geometry to xz, compared to figure 4.21, where it was xy. All other variables are kept the same.

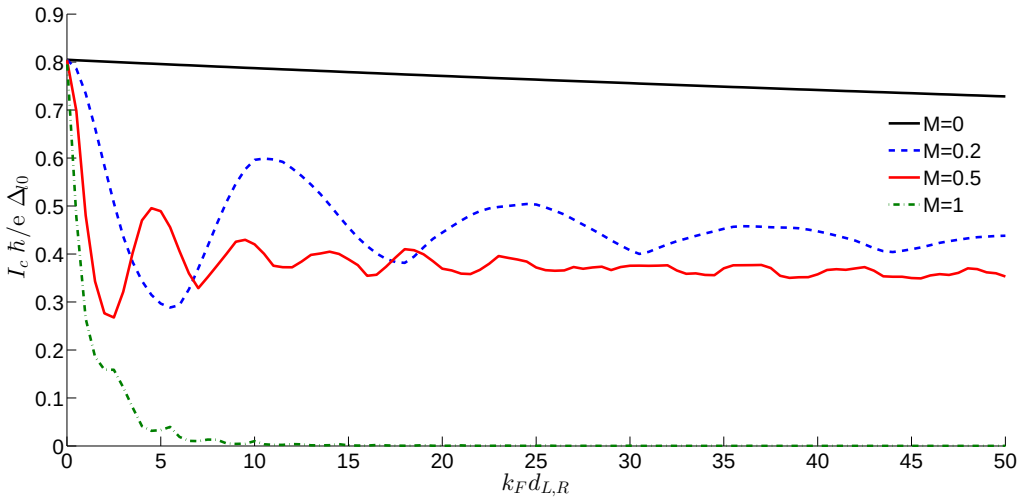

Figure 4.22: Critical current I_c as a function of the ferromagnets width $k_F d_{L,R}$, for different magnetization strength values M, $T/T_c = 0.1$, $k_F d = 25$, $\lambda = 0.1$, $Z_{n,m} = 0$. Geometry is xz.

The supercurrent for xz has retained the same general characteristics as xy. Increasing M creates more oscillations, and for $M = 1$ the supercurrent is damped very quickly. On the other hand, the mean values of supercurrent are increased for $M \neq 0$, which is what we observed in figure 4.20, where the supercurrent, for the xz geometry, was the most increased. The supercurrent for $M = 0$ for geometries xy and xz, is exactly the same.

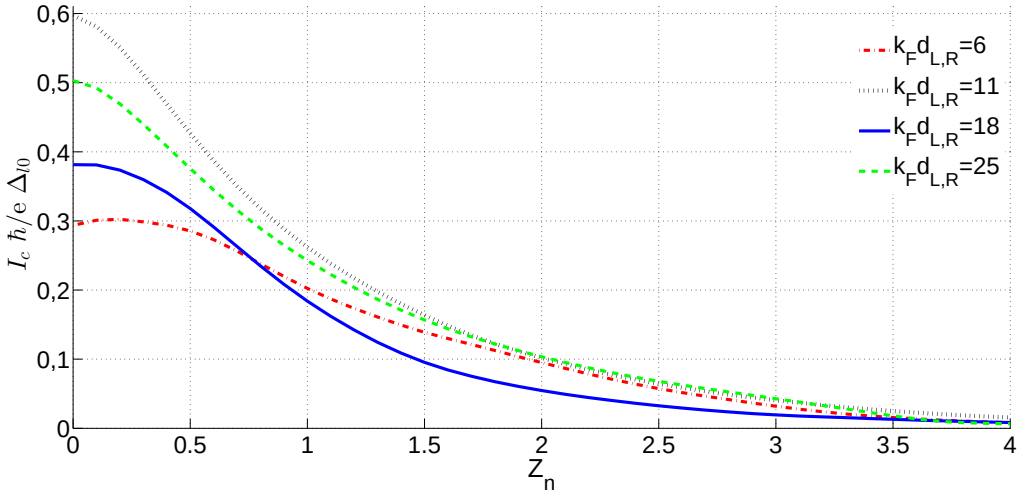

Figure 4.23: Critical current I_c as a function of normal scattering strength, for different ferromagnet widths. $T/T_c = 0.1$, $k_F d = 25$, $M = 0.2$, $Z_m = 0$.

Using the information available in figure 4.22, for $M = 0.2$, the critical supercurrent's first two dips and peaks occur for ferromagnets' width $k_F d_{L,R} = 6,\ 11,\ 18,\ 25$. We then introduce normal scattering to the interfaces of SF/FS, and observe how the critical supercurrent changes for the four $k_F d_{L,R}$ values. As Z_n increases, the value of critical supercurrent decreases and tends to zero for large values of Z_n. The current reduction is similar for all values of $k_F d_{L,R}$.

Previously, in figure 4.23, we kept λ and d constant, while we changed M and $d_{L,R}$. Now, in figure 4.24, we set $M = 0.2$ and $d_{L,R} = 25$. The $2DEG$ width is changed for four values of λ. For $\lambda = 0$, supercurrent oscillates in an irregular way. These oscillations are due to normal scattering resonances occurring inside the ferromagnets. As the $k_F d$ increases they are smoothed out. As λ increases we observe supercurrent oscillations with a much wider period. This period, while irregular, seems to scale with λ^{-1}. For $\lambda = 0.05$, we can argue that one period is $\Delta k_F d = 97 - 25 = 72$, whereas, for $\lambda = 0.1$, two periods are $\Delta k_F d = 76 - 12 = 64/2 = 32$, and finally, for $\lambda = 0.2$, four periods are $\Delta k_F d = 85 - 23 = 62/4 = 15.5$. Some deviation from λ^{-1} is expected considering the irregular periods, but the values are quite close.

In order to explain the λ^{-1} change of period for the supercurrent, we consider that a carrier with spin 2 hits the 2DEG/F interface and is reflected into the opposite carrier with spin 1. The vertical wavenumbers for spin 1 and 2 are

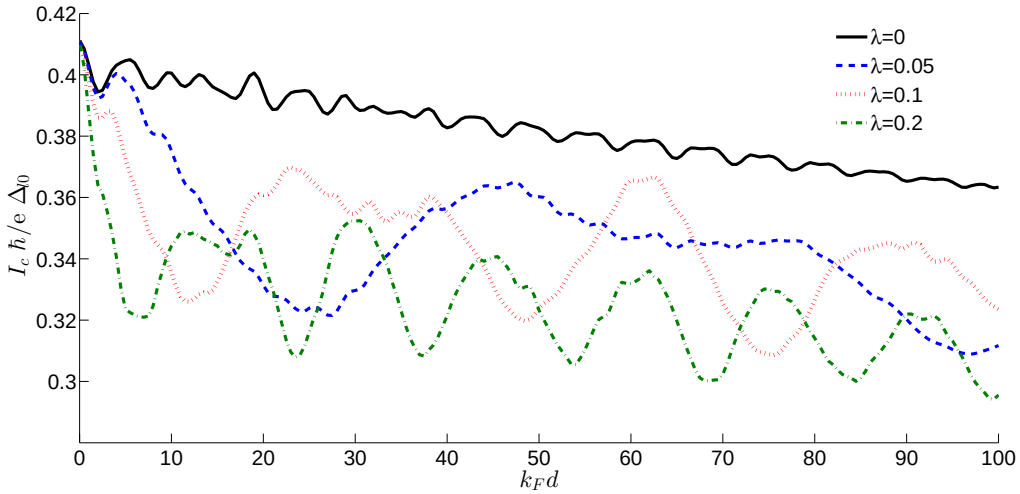

Figure 4.24: Critical current I_c as a function of the 2DEG's width k_Fd, for different RSOC constants λ, $T/T_c = 0.1$, $k_Fd_{L,R} = 25$, $M = 0.2$, $Z_{n,m} = 0$. Geometry is xy.

$$q_{(e,h)20} = \sqrt{1+\lambda^2} + \lambda \tag{95}$$

$$q_{(e,h)10} = \sqrt{1+\lambda^2} - \lambda \tag{96}$$

So, the total phase shift from the above reflection will be

$$q_{(e)20}d - q_{(h)10}d = 2n\pi + \phi + \phi_{sc} \tag{97}$$

solving Eq. (97), we get $q_{(e)20} - q_{(h)10} = (2n\pi + \phi + \phi_{sc})/d \Rightarrow \sqrt{1+\lambda^2} + \lambda - (\sqrt{1+\lambda^2} - \lambda) = (2n\pi + \phi + \phi_{sc})/d \Rightarrow 2\lambda = (2n\pi + \phi + \phi_{sc})/d \Rightarrow d = (n\pi + \phi/2 + \phi_{sc}/2)/\lambda \Rightarrow d \sim \lambda^{-1}$.

In figure 4.25 we keep the same parameters as in figure 4.24. The critical supercurrent has been replaced by zero-phase supercurrent. As we observed already, for the SFS junction, when the magnetization directions form a non-coplanar set, a zero-phase current develops across the junction. While we only have two magnetization vectors on the ferromagnets (xy), a zero-phase current develops as λ increases in value. The spin-orbit coupling introduces a magnetization vector, parallel to the xy plane. For the geometry xy, we expect a coplanar set of magnetization vectors regardless of width or spin-orbit coupling constant. Thus we would not expect a zero-phase current to be generated, with a non-zero value. We observe that the zero-phase current jumps from negative to positive values constantly, as k_Fd increases,

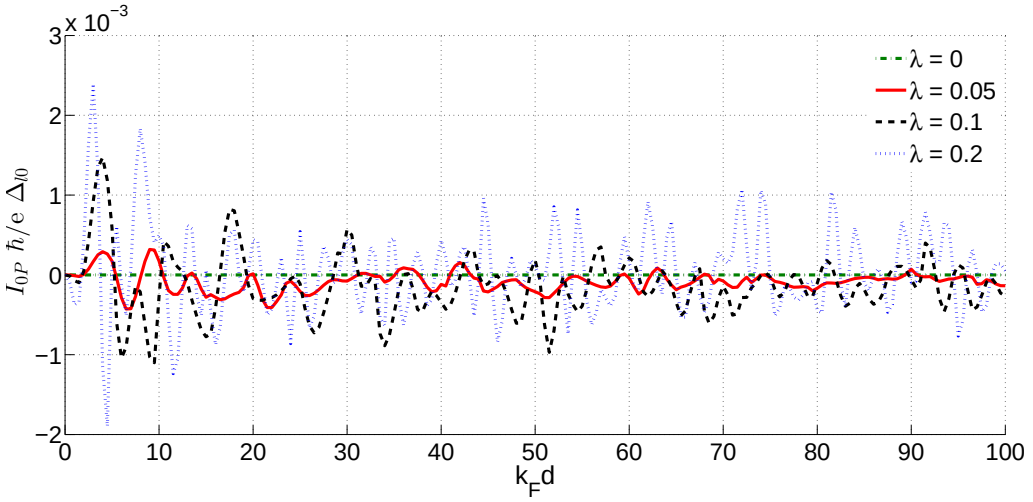

Figure 4.25: Zero-phase current I_{0P} as a function of 2DEG width, for different RSOC constants. $T/T_c = 0.1$, $k_F d_{L,R} = 25$,$M = 0.2$, $Z_{n,m} = 0$. Geometry is xy.

for any non-zero λ. For $\lambda = 0$, it is zero as expected. It is possible we have encountered an "accidental degeneracy" quantum phenomenon, as observed by Margaris et. al. [28].

In figure 4.26 we test how temperature affects critical supercurrent on four different setups. An $SN/N/NS$ junction (top full line - black), an $SN/2DEG/NS$ junction (jagged line - blue), an $SF/N/FS$ junction (bottom full line - red), and an $SF/2DEG/FS$ junction (jagged with dots - green). When $T \to T_c$, superconductivity collapses, and as a result, all four critical supercurrent values diminish until they vanish for $T = T_c$, as expected. Moreover, the Rashba spin-orbit value of $\lambda = 0.1$ has a much lesser impact on supercurrent when compared to magnetization strength of $M = 0.2$, as temperature increases.

4.5 The half-metallic limit

Previously, we mentioned that when $M = 1$, the junction functions in the half-metallic limit. In section 4.4 we analyzed the impact $M = 1$ has on wavenumbers of ferromagnets, and we observed that for $k_F d_{L,R} > 7$ the critical supercurrent decays. In this section, we set $M = 1$ and set the spin-active interfaces at $Z_m = 1$. In order to completely avoid tunneling phenomena, we set the ferromagnets' width at $k_F d_{L,R} = 150$, where specific geometries exist that allow significant critical supercurrent.

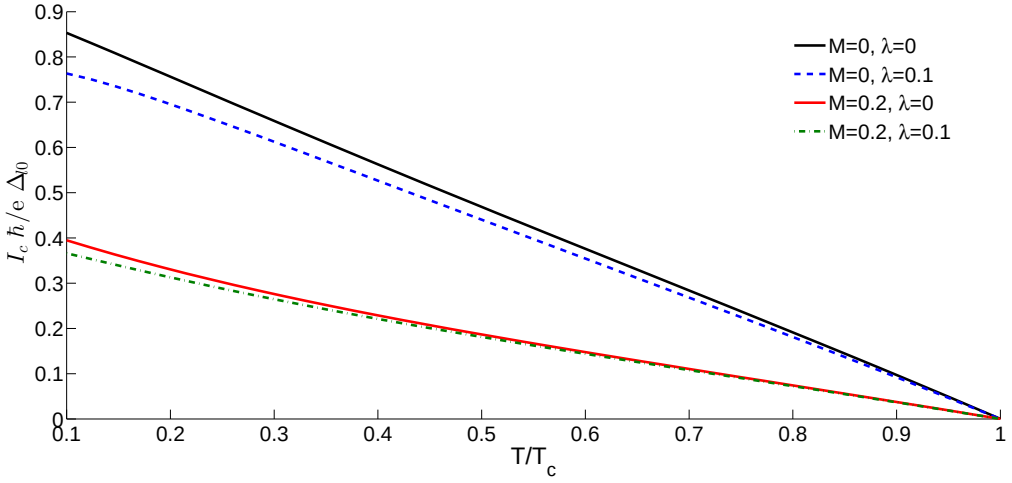

Figure 4.26: Critical current I_c as a function of normalized temperature, for four different junction setups. $k_F d = k_F d_{L,R} = 25$, $Z_{n,m} = 0$.

Geometries, in this section, are four-component as we have two interfaces in addition to the ferromagnets. So, we present geometries, as we discussed in section 4.1, by stating first the left interface, then the left ferromagnet, the right ferromagnet, and lastly the right interface. We argue that when geometries have one ferromagnet's $\vec{M}_{L,R}$, parallel to the neighbouring interface's $\vec{Z}_{mL,R}$, the critical current is rapidly reduced to zero when $k_F d_{L,R} = 10$.

For zero spin-orbit coupling we change the width of the 2DEG, $k_F d$, for different geometries. The two cases, in figure 4.27, correspond to several geometries, which fall in two general categories, PP and VV. PP denotes that the two ferromagnet magnetization vectors are parallel to each other, while VV denotes that they are vertical to each other. Following up on previous results, when a ferromagnetic magnetization vector $\vec{M}_{L,R}$ and the neighbouring interface magnetization vector, $\vec{Z}_{mL,R}$, are parallel, the critical supercurrent is reduced to zero. Thus, in figure 4.27, $\hat{r}$ can not be parallel to the neighbouring $\vec{M}$.

Any geometry that has parallel $\vec{M}_{L,R}$ and non parallel $\vec{Z}_{mL,R}$ (to the neighbouring $\vec{M}$) has the same critical supercurrent, denoted by $rPPr$. The same applies for vertical $\vec{M}_{L,R}$ and non parallel (to the neighbouring $\vec{M}$) $\vec{Z}_{mL,R}$. Also, we observe that the oscillations in critical supercurrent value are more intense for the $rVVr$ geometries. The existence of a metal between the two ferromagnets (and the change of its width) affects differently the junction, depending on the angle between the $\vec{M}_{L,R}$ directions. The supercurrent oscillates as the width increases, but the actual period of the oscillations is

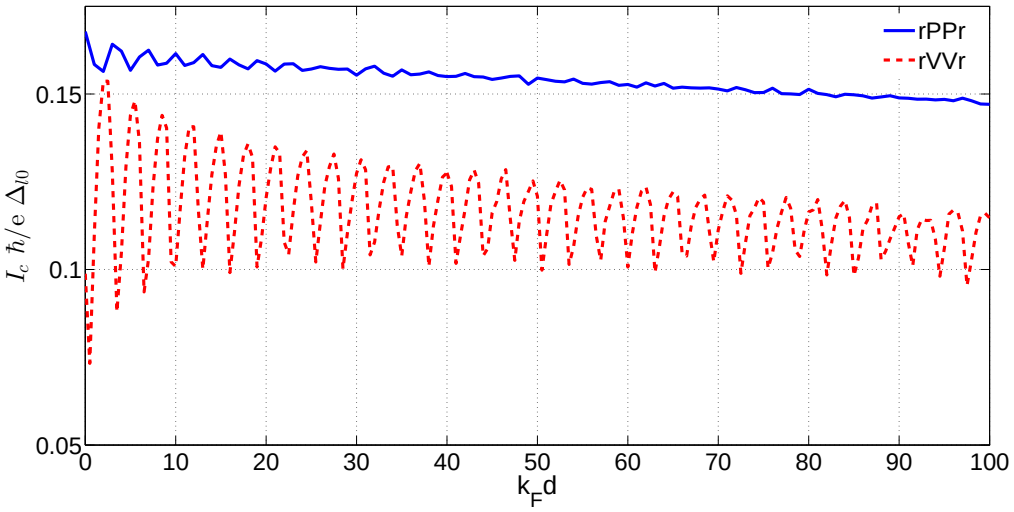

Figure 4.27: Critical current I_c as a function of 2DEG's width d, $Z_m = 1$, $M = 1$, $\lambda = 0$, $T/T_c = 0.1$, $k_F d_{L,R} = 150$, $Z_n = 0$. Geometry: $r = x, y, z$, P = parallel layers, V = vertical layers.

constant regardless of width and is close to 3. Below, we provide supercurrent versus k_p graphs calculated for $k_F d$ values of 8 to 10, which is consistent with the period observed.

In figure 4.28, we calculate the normal incidence current as a function of width. We observe that it oscillates with the same period as the critical current does. This period, is exactly equal to π. In each period, current begins in negative values and changes to positive values. This change in sign means that the maximum current in the current-phase relation is negative at first, but the positive peak takes over after half a period. We remind that critical current takes absolute values. When normal incidence does not contribute to the current, the critical current takes its minimum value, while also the zero-phase current vanishes.

In figure 4.29, we can observe that the supercurrent distribution, as we move from a peak ($k_F d = 8$) to a dip ($k_F d = 10$) (see figure 4.27, vertical magnetization vectors), changes only slightly for $k_p \geq 0.5$ values. The most significant change in distribution is seen close to zero incidence, where the supercurrent drops to zero, for $k_F d = 9.25$. The point of vanishing supercurrent moves towards higher k_p values as width increases, also affecting the rest of the distribution, distorting the high k_p values.

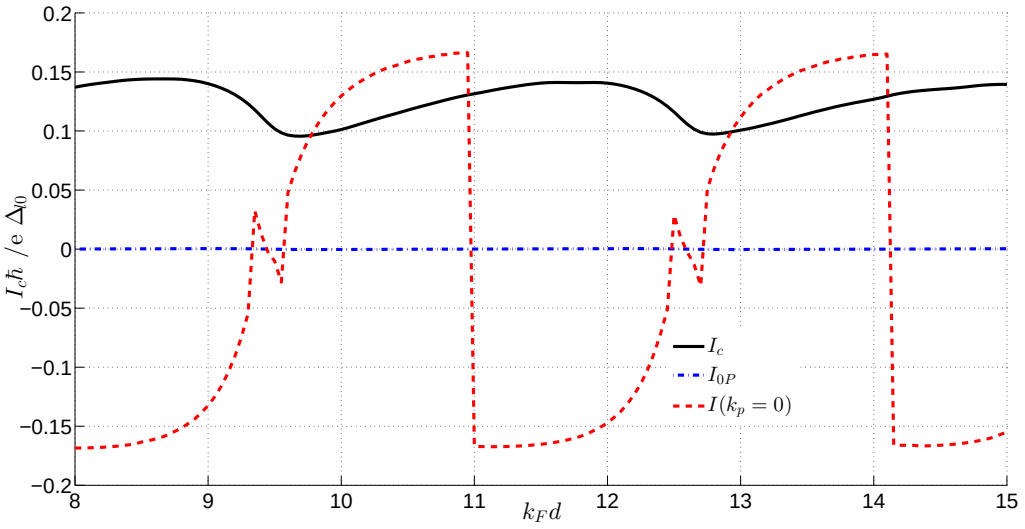

Figure 4.28: Critical current (full line), zero-phase current (jagged with dots line) and normal incidence current ($k_p = 0$) as a function of $2DEG$ width k_Fd, $Z_m = 1$, $M = 1$, $\lambda = 0$, $T/T_c = 0.1$, $k_Fd_{L,R} = 150$, $Z_n = 0$. Geometry: $zxyz$.

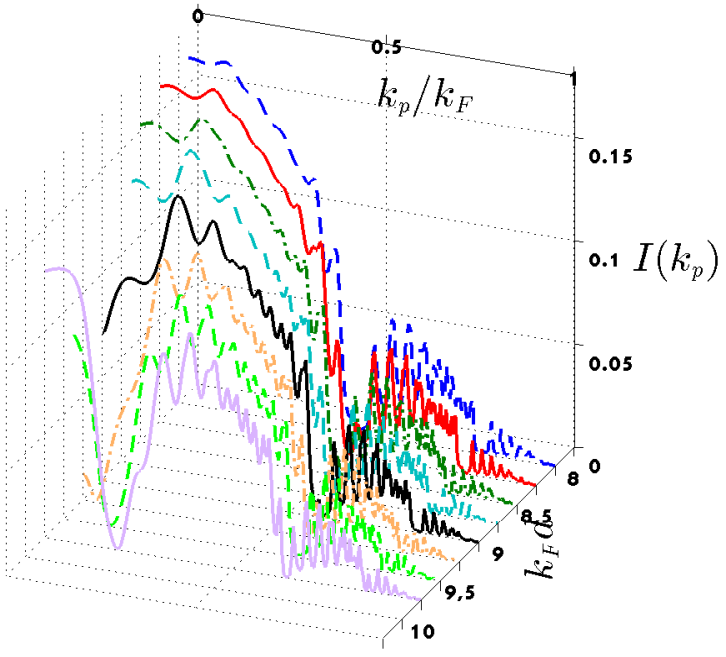

Figure 4.29: Supercurrent distribution as a function of 2DEG's width k_Fd, $Z_m = 1$, $M = 1$, $\lambda = 0$, $T/T_c = 0.1$, $k_Fd_{L,R} = 150$, $Z_n = 0$. Geometry: $zxyz$.

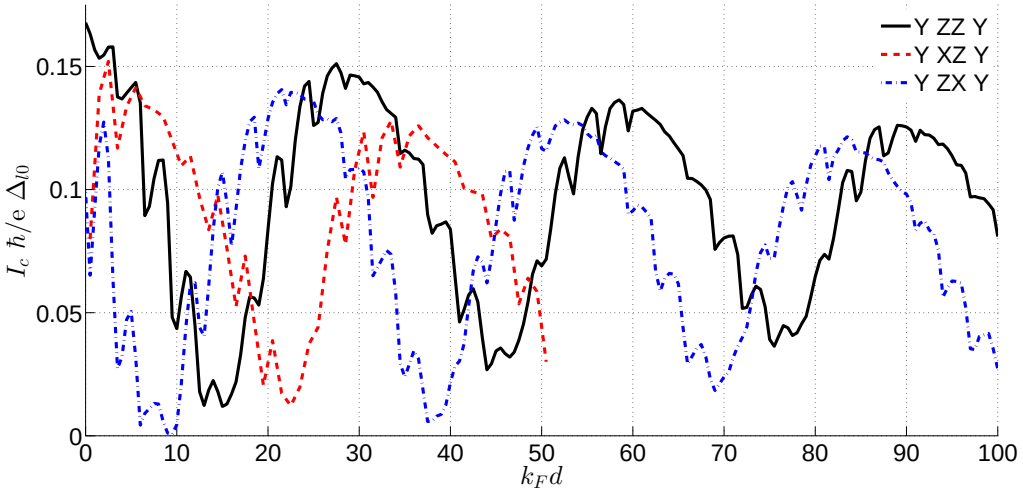

Figure 4.30: Critical current I_c as a function of 2DEG's width d, $Z_m = 1$, $M = 1$, $\lambda = 0.1$, $T/T_c = 0.1$, $k_F d_{L,R} = 150$, $Z_n = 0$. Geometries are $yzzy$, $yxzy$ and $yzxy$.

From $\lambda = 0$ in figure 4.27, we change the spin-orbit coupling to $\lambda = 0.1$, in figure 4.30. We observed the critical supercurrent symmetries to break in figure 4.20, and as a result, we expect the critical supercurrent to be affected by the geometries of the junctions. The same small oscillations that occurred for $\lambda = 0$, still exist and oscillate with the same period. The position of peaks and dips seems to remain unchanged regardless of geometry. However, another oscillation with much larger period exists. This period is close to $\Delta k_F d = 30$, which is 10 times the period of the small oscillations. This large oscillation only occurs for non-zero spin-orbit coupling values of λ. As a result, it must be due to particle scattering inside the $2DEG$. The geometries $yzxy$ and $yxzy$ do not exhibit the same critical supercurrent, as a result of the spin-orbit coupling, despite the fact that they are symmetrical to ferromagnetic layer switch. Comparing these two geometries we can observe that they have the same critical supercurrent value for $k_F d = 0$, which we expected due to being symmetric. As $k_F d$ increases, they split and have a largely different character. We can mention that as they oscillate, where $yzxy$ has a peak in supercurrent, $yxzy$ has a dip, in $k_F d = 23$, and the other way around, in $k_F d = 37$. In figure 4.24, we discussed the reason behind the large oscillations occurrence, and why they change as a function of λ^{-1}. The same principle applies here.

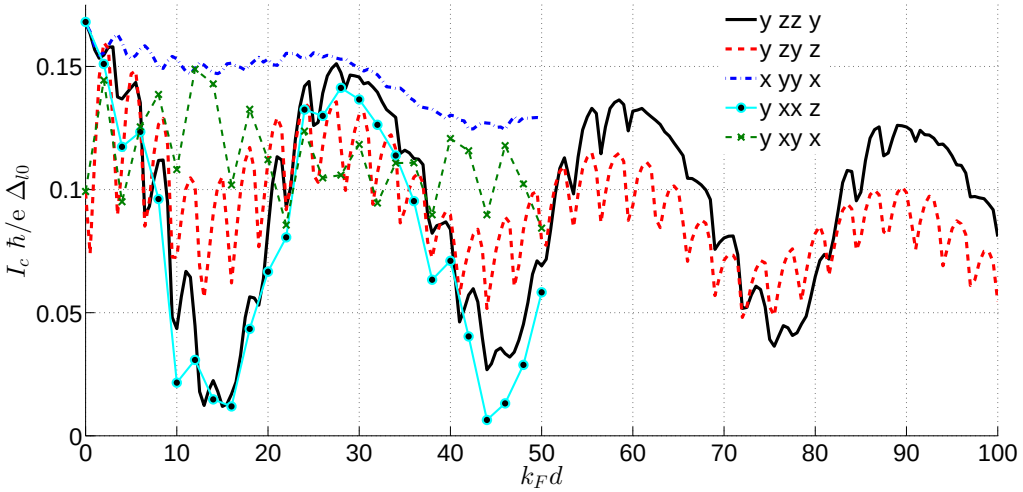

Figure 4.31: Critical current I_c as a function of 2DEG's width d, $Z_m = 1$, $M = 1$, $\lambda = 0.1$, $T/T_c = 0.1$, $k_F d_{L,R} = 150$, $Z_n = 0$. Geometries are $yzzy$, $yzyz$ and $xyyx$.

Continuing the same comparison, in figure 4.31 we compare the geometry $yzzy$ introduced in figure 4.30, with geometries $yzyz$ and $xyyx$, while also providing low-grid calculations for $yxxz$ and $yxyx$. These low-grid calculations serve the purpose of determining if the calculated points of the two geometries coincide with any of the full-grid graphs. For the full-grid geometries, the small oscillations are unchanged, but the large oscillations are less intense, for both $yzyz$ and $xyyx$, compared to figure 4.30. We observe that while the period is constant, the difference between the highest and lowest critical supercurrent values has decreased. As we compare the two figures, we understand that the information given is not enough to make a statement, accounting for every geometry. On the other hand, we can argue that when the ferromagnetic layers align with the y axis, the critical supercurrent, as a function of width, varies slightly. That happens for the geometry $xyyx$. The magnetic field produced is not fixed on any axis of the xy plane. It can vary with the incidence of the particles. So, for $xyyx$, $yxxz$ and $yxyx$ geometries, the ferromagnetic layers are coplanar to the magnetic field of the $2DEG$. The resulting critical supercurrent is not the same in any of the three geometries. We also notice that $yzzy$ and $yxxz$ geometries have the same character, but some of the critical supercurrent values do not coincide.

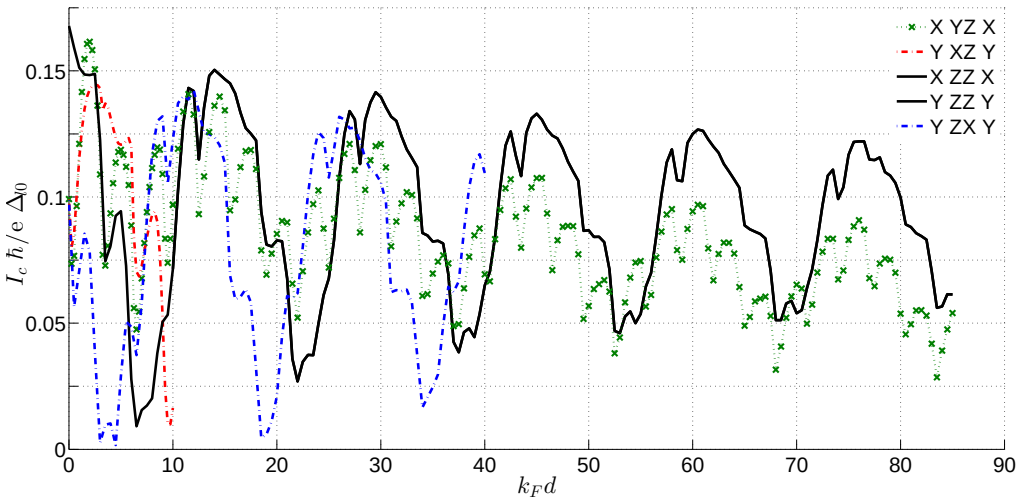

Figure 4.32: Critical current I_c as a function of 2DEG's width d, $Z_m = 1$, $M = 1$, $\lambda = 0.2$, $T/T_c = 0.1$, $k_F d_{L,R} = 150$, $Z_n = 0$.

In figures, 4.30 and 4.31, we compared several geometries for $\lambda = 0.1$. In figure 4.32, we set $\lambda = 0.2$. As expected, the period of large oscillation is constant for all geometries calculated. Compared to $\lambda = 0.1$ figures, the large oscillation period has increased by a value of 2. We again mention that the period of the large oscillation scales with λ^{-1}. The small oscillations are dominated by the larger period of the large oscillation. Only $xyzx$ geometry has fully visible small oscillations. Notice also, in full line, that two geometries completely coincide, $xzzx$ and $yzzy$. The ferromagnetic layers have the same direction, and we expected that interface spin-flips will not affect the critical supercurrent, only enable it through triplet correlations.

In figure 4.33 we calculate the critical supercurrent (clean lines) and the absolute zero-phase current (X-lines), for geometry $xyyx$, for three values of spin-orbit coupling constant. We notice that for $\lambda = 0$, zero-phase current is 0, as expected for a coplanar set of magnetization vectors. Moreover, zero-phase current values close to zero tend to change abruptly, thus, at these points the zero-phase current takes negative values. This means that the junction transitions from cos-like to $-cos$-like (n peak to $n+1$ peak, $n = 1, 3, 5, ...$). That occurs because on the n peaks, the zero-phase current has the same value as the critical supercurrent. In addition, the n+1 peaks, which have negative values, always coincide with peaks of the critical supercurrent. While we do have a coplanar set of magnetization vectors, the effect of the spin-orbit coupling enables strong zero-phase current.

Previously, we claimed that the direction of the interfaces' magnetization does not affect critical supercurrent as long as it enables triplet correlations.

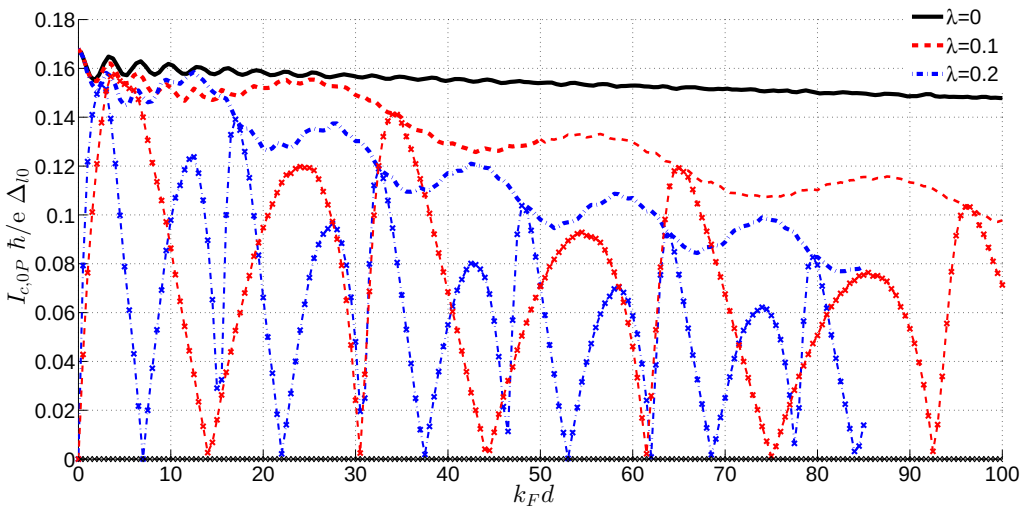

Figure 4.33: Critical supercurrent I_c (non-X-lines) and absolute zero-phase current I_{0P} (X-lines), as a function of $k_F d$ for different values of λ, $T/T_c = 0.1$, $Z_m = 1$, $M = 1$, $k_F d_{L,R} = 150$, $Z_n = 0$. Geometry is $xyyx$.

That means it must be vertical to its neighbouring ferromagnetic magnetization vector. In order to test this claim, we calculate the critical current and zero-phase current for five geometries, as we change the direction of the right interface's magnetization $\vec{Z}_{mR}$. The calculations are made for $\lambda = 0.1$, but also included, are the results for $\lambda = 0$. The direction of $\vec{Z}_{mR}$ is changed from $\hat{z}$ axis to $\hat{x}$, from $\hat{x}$ to $\hat{y}$ and from $\hat{y}$ back to $\hat{z}$.

In figure 4.34, geometry is $xzy\vec{Z}_{mR}$. Full lines denote that $\lambda = 0$, whereas jagged lines denote $\lambda = 0.1$. Also, clean lines denote critical current I_c and marked-by-x lines denote zero-phase current I_{0P}. When $\vec{Z}_{mR}$ is parallel to $\vec{M}_R$ the supercurrent vanishes. As the direction of $\vec{Z}_{mR}$ moves on the zx and yz planes the supercurrent increases. When $\vec{Z}_{mR}$ is on the xy plane, where it's vertical to $\vec{M}_R$, critical current has a constant value. This result is true regardless of λ, despite the fact that absolute value of supercurrent has decreased for $\lambda = 0.1$. Geometry $xyz\vec{Z}_{mR}$ always forms a non-coplanar set of magnetization vectors, thus we expect that is always produces zero-phase supercurrent. However, as long as $\vec{Z}_{mR}$ is on the zx plane, the zero-phase current vanishes. After it is aligned with $\hat{x}$ axis, it slowly changes to a *cos*-like junction. On the other hand, zero-phase current with spin-orbit interaction, takes only negative values (except when $\vec{Z}_{mR}$ is parallel to the $\vec{M}_R$) and is much smoother as $\vec{Z}_{mR}$ changes.

For $zyz\vec{Z}_{mR}$ geometry, in figure 4.35, we observe that as long as $\vec{Z}_{mR}$ is vertical to $\vec{M}_R$, the current is constant, regardless of λ. Also, the supercurrent

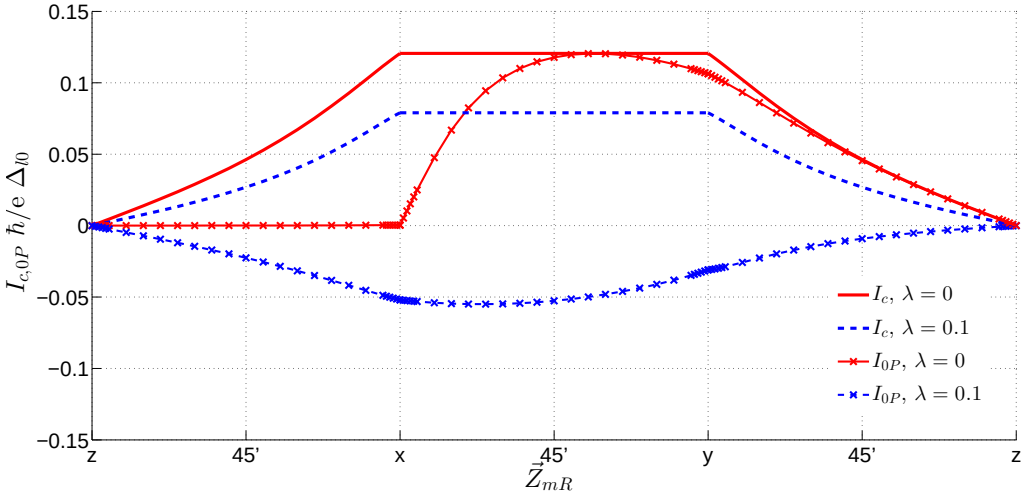

Figure 4.34: Critical current I_c and zero-phase current I_{0P} as a function of left interface's magnetization direction $\vec{Z}_{mR}$, for $\lambda = 0, 0.1$. $Z_m = 1$, $M = 1$, $T/T_c = 0.1$, $k_F d = 50$, $k_F d_{L,R} = 150$, $Z_n = 0$. Geometry is $xyz\vec{Z}_{mR}$.

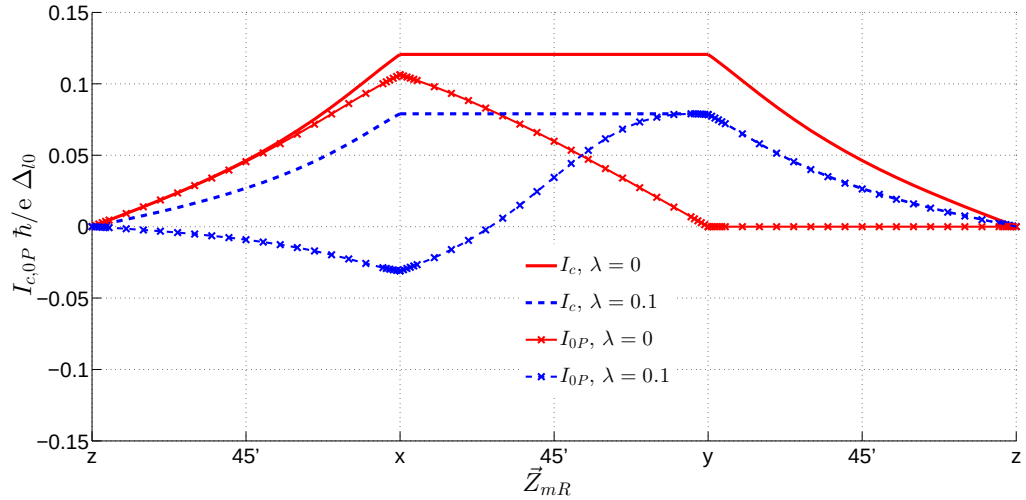

Figure 4.35: Critical current I_c and zero-phase current I_0 as a function of left interface's magnetization direction $\vec{Z}_{mR}$, for $\lambda = 0, 0.1$. $Z_m = 1$, $M = 1$, $T/T_c = 0.1$, $k_F d = 50$, $k_F d_{L,R} = 150$, $Z_n = 0$. Geometry is $zyz\vec{Z}_{mR}$.

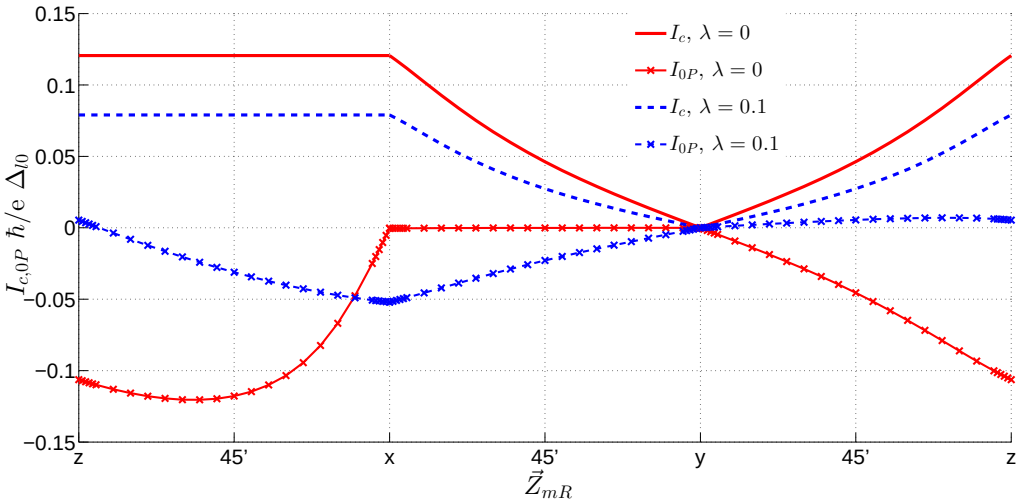

Figure 4.36: Critical current I_c and zero-phase current I_0 as a function of left interface's magnetization direction $\vec{Z}_{mR}$, for $\lambda = 0, 0.1$. $Z_m = 1$, $M = 1$, $T/T_c = 0.1$, $k_F d = 50$, $k_F d_{L,R} = 150$, $Z_n = 0$. Geometry is $xzy\vec{Z}_{mR}$.

vanishes when $\vec{Z}_{mR}$ is parallel to $\vec{M}_R$. The zero-phase current for $\lambda = 0$ vanishes when $\vec{Z}_{mR}$ is on the yz plane, while takes non-zero values for all other directions. Zero-phase current for $\lambda = 0.1$ takes non-zero values for all directions of $\vec{Z}_{mR}$, except when it transitions to a *cos*-like junction for $\vec{Z}_{mR} = (xy30)$. Also, comparing the two figures, we can see that critical supercurrent values are exactly the same. We argue that values are the same due to ferromagnetic layers having the same geometry.

In figure 4.36, we flip the ferromagnetic layer directions, from figure's 4.34 $xyz\vec{Z}_{mR}$ to $xzy\vec{Z}_{mR}$. We mention that the supercurrent now vanishes when $\vec{Z}_{mR} = \hat{y}$. The critical supercurrent values, regardless of spin-orbit interaction, are the same. Zero-phase current for $\lambda = 0$, again vanishes when $\vec{Z}_{mR}$ is on the xy plane. In addition, it assumes exactly the opposite values, when compared to $xyz\vec{Z}_{mR}$, for every other direction of $\vec{Z}_{mR}$.

For the $xzx\vec{Z}_{mR}$ geometry, in figure 4.37, enabling spin-orbit interaction does not affect the supercurrent or zero-phase current. To be accurate, values of I_c and I_{0P} differ for $\lambda = 0,\ 0.1$, but the difference is negligible when compared to the previous geometries. The zero-phase current vanishes when $\vec{Z}_{mR}$ is on the zx plane.

Changing the $\vec{Z}_{mL}$ into y, compared to figure 4.37, changes only the character of the zero-phase current for non-zero values. In figure 4.38, zero-phase current vanishes when $\vec{Z}_{mR}$ is on the xy plane.

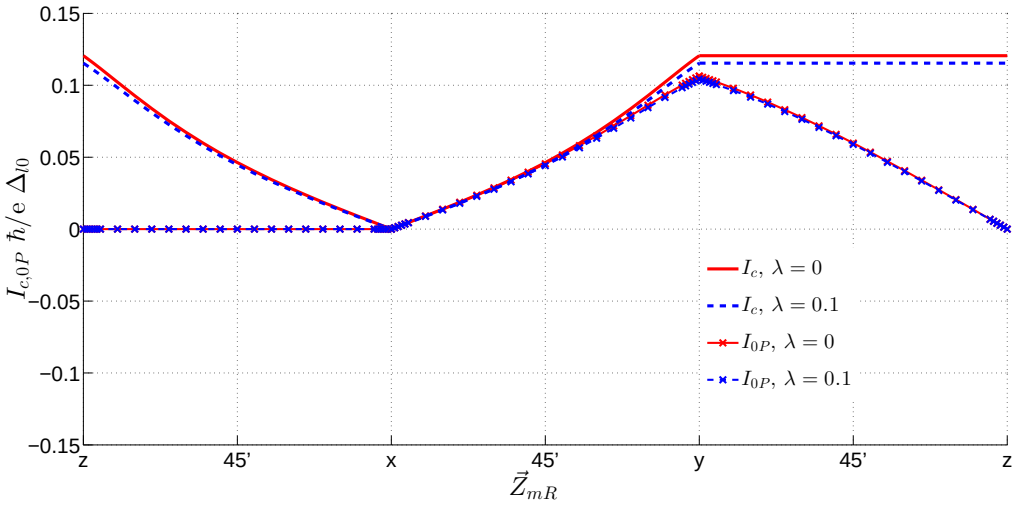

Figure 4.37: Critical current I_c and zero-phase current I_0 as a function of left interface's magnetization direction $\vec{Z}_{mR}$, for $\lambda = 0, 0.1$. $Z_m = 1$, $M = 1$, $T/T_c = 0.1$, $k_F d = 50$, $k_F d_{L,R} = 150$, $Z_n = 0$. Geometry is $xzx\vec{Z}_{mR}$.

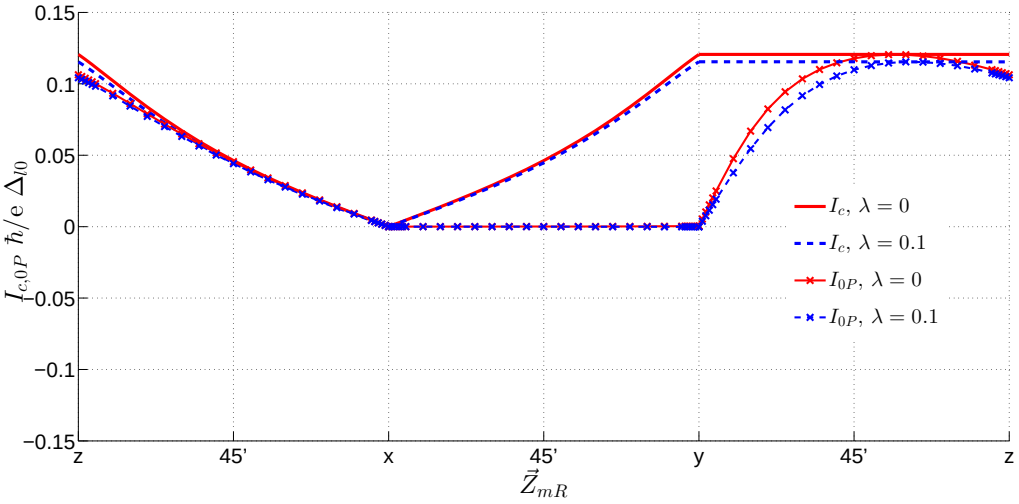

Figure 4.38: Critical current I_c and zero-phase current I_0 as a function of left interface's magnetization direction $\vec{Z}_{mR}$, for $\lambda = 0, 0.1$. $Z_m = 1$, $M = 1$, $T/T_c = 0.1$, $k_F d = 50$, $k_F d_{L,R} = 150$, $Z_n = 0$. Geometry is $yzx\vec{Z}_{mR}$.

5 Conclusion

We considered an $S/F/2DEG/F/S$ short, ballistic junction in the clean limit. We studied the effects of the spin-orbit interaction on the critical supercurrent, zero-phase current and current-phase relation, when they are already modulated by two ferromagnetic layers.

More specifically, we observed the changes in current-phase relation types with junction parameters. We noticed the different effect of cut-off points, due to magnetization and spin-orbit interaction. The cut-off in k_p, due to magnetization, vanishes the contribution to the supercurrent above the cut-off k_p. When we have no magnetization, but only spin-orbit coupling, the cut-off k_p point does not give vanishing supercurrent. When both $M \neq 0,\ \lambda \neq 0$, it is the cut-off point due to magnetization that dominates the contribution to supercurrent for high k_p, while the cut-off in the $2DEG$ layer just causes an abrupt change in the supercurrent, without vanishing it. We also observed the difference between current-phase relations of magnetization-only layers and spin-orbit-only layers. Spin-orbit-only layers produce only 0-junctions, whereas magnetization-only were observed to transition from 0 to π junctions.

Moreover, we observed the effect that the normal resonances and anti-resonances have on the supercurrent. Normal resonances are affected by the width of the layers, by the magnetization strength, by spin-orbit coupling and by interface normal scattering. As these parameters change, the change in normal resonances influences the supercurrent, inducing oscillations. In addition, for inhomogeneous ferromagnets, the spin-orbit interaction has a strong influence on the supercurrent. Calculating and comparing the current-phase relation for $\lambda = 0$ and $\lambda \neq 0$, the supercurrent of two of the four geometries did not change, while for the other two it changed significantly. Spin-orbit coupling breaks supercurrent degeneracies.

For a two-ferromagnet geometry, we found that the critical supercurrent depends on the relative angle between the magnetization vectors, in absence of spin-orbit coupling. On the other hand, with spin-orbit coupling, the critical supercurrent differed for most geometries and was increased in value for specific geometries. As we mentioned, magnetization and spin-orbit interaction affect normal scattering, so as we increased the width of the junction, more resonances and anti-resonances were produced, greatly modulating the supercurrent, whose separation depends on the width. However, normal scattering strength acts destructively on current as it increases. The spin-orbit coupling induces oscillations with a larger period, which scales with λ^{-1}, and is due to normal reflections in the $2DEG$ layer. Increasing temperature lowers the supercurrent, until superconductivity collapses (on $T = T_c$), and supercurrent vanishes.

For values of magnetization $M \to 1$, we observed the supercurrent to decrease in value, dropping to zero value after magnetization reached $M = 1$. This limit is called the half-metallic limit, because in the ferromagnet, one spin can propagate while the other decays. We argued that supercurrent dropped to zero due to the nature of the Andreev reflection process, which reflects a particle with a spin, to the anti-particle with the opposite spin, which induces *singlet correlations*. In the half-metallic limit, increasing the interface spin-flip scattering strength, we observed significant supercurrent and quite strong for k_p above the cut-off point for a spin $\downarrow$, in the ferromagnet. Thus spin-active interfaces induce *triplet correlations* and in this, the homogeneity of the magnetization is crucial.

Continuing on the half-metallic limit with spin-active interfaces, we observed for $\lambda = 0$ the supercurrent assumes two different behaviours. The supercurrent is modulated according to the angle between the ferromagnetic magnetization vectors. When they are parallel, there is an almost linear decay with width, with the supercurrent being modulated when they are vertical. The period of the critical supercurrent oscillation is about π and we see a clear correlation between normal incidence contribution to the current, and the value of the critical supercurrent. They have the same period, and diminishing of normal incidence is translated to minimum critical supercurrent values. When we increased λ, each geometry produced its own characteristic current versus width relation. The period of oscillations was affected by the value of λ^{-1}, as mentioned before. Also, we observed that spin-orbit interaction can induce zero-phase current when a geometry does not support zero-phase current on its own (when λ was zero). The periodicity of the zero-phase current indicates transitions of the junction, as a function of width. Lastly we argued and observed that as long as an interface magnetization vector was vertical to the neighbouring ferromagnetic vector, the supercurrent assumed its maximum potential value. When it is parallel, the supercurrent vanishes.

6 Acknowledgements

First and foremost, i would like to express my sincere gratitude to my advisor Prof. Nikos Flytzanis, for the continuous support of my Master's study and research, for his patience, motivation, enthusiasm, and immense knowledge. His guidance helped me during the research and writing of this thesis.

I would also like to thank the two committee members, Prof. Xenophon Zotos and Prof. Nikos Efremidis for their patience, encouragement and insightful comments.

I sincerely thank Dr. Ioannis Margaris for providing the computer code with which this research was made possible, while also assisting with bugs and fixes. Also, i would like to thank Dr. Vasillis Paltoglou for his help in all stages of my research, from the very first theoretical questions to the proof-reading of the whole thesis.

This project would not be possible without the help of my parents, Elias Alexandrakis and Maria Stratidaki, and my friend, Demmie Intzepogazoglou. Their psychological support proved invaluable since day one.

Last but not least, i would like to thank my teacher/professor Mr. Stefanos Traxanas for he inspired me when it was most needed.

7 Bibliography

References

[1] A. Schilling et al. (1993). *Superconductivity above* $130K$ *in the Hg-Ba-Ca-Cu-O system*. Nature 363 (6424): 56.

[2] P. G. D. Gennes, *Superconductiviy of Metals and Alloys* (W. A. Benjamin, New York, 1966)

[3] J. Bardeen, L. N. Cooper, and J. R. Schrieffer, Phys. Rev. **108**, 1175 (1957).

[4] A. F. Andreev, Zh. Eksp, Teor. Fiz. **46**, 1823 (1964), [Sov. Phys. JETP **19**, 1228 (1964)].

[5] G. E. Blonder, M. Tinkham, and T. M. Klapwijk, Phys. Rev. B **25**, 4515 (1982).

[6] Ishii, C., 1970, Prog. Theor. Phys. **44**, 1525.

[7] Josephson, B. D., 1962, Phys. Lett. **1**, 251.

[8] Furusaki A and Tsukada M 1991 *Solid State Commun.* **78** 299-302.

[9] A. Furusaki, M. Tsukada, Solid State. Comm. 78, 4 (1991)

[10] L.W. Molenkamp, G. Schmidt and G.E.W. Bauer, Phys. Rev. B **64**, 121202 (2001)

[11] Z. Yang, J. Wang and K.S. Chan, J. Appl. Phys. **103**, 103905 (2008)

[12] Z. Yang, J. Wang and K.S. Chan, J. Phys.: Condens. Matter **22**, 045302 (2010)

[13] P.F. Bagwell, Phys. Rev. B **46**, 12573 (1992)

[14] K. Halterman and O. T. Valls, Phys. Rev. B **69**, 104517 (2004)

K. Halterman and O. T. Valls, Phys. Rev. B **70**, 014517 (2004)

[15] K. Halterman and O. T. Valls, Phys. Rev. B **66**, 224516 (2002)

[16] Z. Radovic, N. Lazarides, N. Flytzanis, Phys. Rev. B **68**, 014501 (2003)

[17] F. S. Bergeret, A. F. Volkov and K. B. Evetov, Phys. Rev. B **64**, 134506 (2001)

[18] Yu. S. Baresh and I. Bobkova, Phys. Rev. B **65**, 144502 (2002)

[19] T. M. Klapwijk, G. E. Blonder and M. Tinkham, Physica B&C **109** & **110 B**, 1657 (1982)

[20] I. O. Kulik, Zh Eksp. Teor. Fiz. **57**, 1745 (1969), [Sov. Phys. JETP **30**, 944 (1970)]

[21] C. W. J. Beenakker in *Transport Phenomena in Mesoscopic Systems*, p.235, editors:H. Fukujama and T. Ando, Springer Verlag, Berlin 1992.

[22] A. Chrestin, T. Matsuyama, and U. Merkt, Phys. Rev. B **49**, 498 (1994).

[23] Y. A. Bychkov and E I Rashba, J. Phys. C: Solid State Phys. **17**, 6039 (1984).

[24] Dimitrova, O. V., Feigel'man, M. V., 2006, J. Phys.: Experim. Theor. Phys. **4**, 102

[25] I. V. Krive, A. M. Kadigrobov, R. I. Shakhter and M. Johnson, Phys. Rev. B **71**, 214516 (2005)

[26] A. Buzdin, PRL **101**, 107005 (2008)

[27] E.V. Bezuglyi, A.S. Rozhavsky, I.D. Vagner and P. Wyder, Phys. Rev. B **66**, 052508 (2002)

[28] Margaris I, Paltoglou V, Flytzanis N, *Zero phase difference supercurrent in ferromagnetic Josephson junctions*, J. Phys.: Condens. Matter **22** (2010) 445701.